박 사 학 위 논 문
Ph.D. Dissertation

리드버그 원자를 통한 양자 프로그래밍

Quantum Programming with Rydberg atoms

2025

정 석 호 (鄭 錫 浩 Jeong, Seok-Ho)

한 국 과 학 기 술 원

Korea Advanced Institute of Science and Technology

박 사 학 위 논 문

리드버그 원자를 통한 양자 프로그래밍

2025

정 석 호

한 국 과 학 기 술 원

물리학과

리드버그 원자를 통한 양자 프로그래밍

정 석 호

위 논문은 한국과학기술원 박사학위논문으로
학위논문 심사위원회의 심사를 통과하였음

2025년 5월 27일

심사위원장 안 재 욱 (인)

심 사 위 원 최 재 윤 (인)

심 사 위 원 강 명 수 (인)

심 사 위 원 김 동 규 (인)

심 사 위 원 배 준 우 (인)

Quantum Programming with Rydberg atoms

Seok-Ho Jeong

Advisor: Jaewook Ahn

A dissertation submitted to the faculty of
Korea Advanced Institute of Science and Technology in
partial fulfillment of the requirements for the degree of
Doctor of Philosophy in Physics

Daejeon, Korea
May 27, 2025

Approved by

_____

Jaewook Ahn
Professor of Physics

The study was conducted in accordance with Code of Research Ethics[1].

---

[1] Declaration of Ethical Conduct in Research: I, as a graduate student of Korea Advanced Institute of Science and Technology, hereby declare that I have not committed any act that may damage the credibility of my research. This includes, but is not limited to, falsification, thesis written by someone else, distortion of research findings, and plagiarism. I confirm that my thesis contains honest conclusions based on my own careful research under the guidance of my advisor.

초 록

강한 상호작용을 가진 중성 원자의 유연한 기하학적 구조를 제공하는 리드버그 원자 배열은 양자컴퓨팅에 많은 기회를 제공한다. 이 학위논문에서는, 우선 보조원자 (와이어원자)를 사용하여 큐비트 원자 (데이터원자)간의 결합을 중재하는 방식으로 리드버그 광학게이트를 설계하는 양자 회로 모델 프로그래밍을 제시한다. 그리고 두가지 새로운 종류의 리드버그 원자 양자 프로그래밍 방식을 제시한다. 하나는 대표적인 NP(비결정론적 다항시간)-완전 문제 인스턴스인 3-충족성(3-SAT) 문제 인스턴스를 리드버그 원자 양자 실험에 내재적인 최대독립집합(MIS) 문제 인스턴스의 큐비트 배열 구조로 변환하는 프로그래밍이다. 이러한 양자 알고리즘을 리드버그 봉쇄 현상과 단열 양자 프로세스를 통하여 3-SAT 문제 인스턴스를 실험적으로 평가한다. 그리고 다른 하나로 퀜치 에볼루션(QE)과 단열 양자 컴퓨팅(AQC) 실험 데이터에 소프트웨어 결합을 하여 기존 고전적 방식 대비 처리 시간을 크게 줄이고 정확도를 올리는 리드버그 양자 강화 시뮬레이션 어닐링(QESA)이다. QESA는 시뮬레이션 어닐링(SA)에 비해 목표 근사화 비율에 도달하는 효율적인 성능 이점을 보여준다.

핵 심 낱 말 양자 계산 문제, 리드버그 원자, 양자 와이어, 양자 게이트, 충족성 문제, 최대독립집합 문제, 단열 양자 컴퓨팅, 양자-고전 하이브리드 알고리즘

Abstract

The Rydberg arrangement of atoms, which provides a flexible geometry of neutral atoms with strong interactions, offers many chances for quantum computing. In this thesis, we first present a quantum circuit model programming that designs Rydberg optical gates by using auxiliary atoms (wire atoms) to mediate the coupling between qubit atoms (data atoms). Then, we present two new kinds of Rydberg atom quantum programming schemes. First, we program to transform a representative nondeterministic polynomial-time (NP)-complete problem instance, the 3-satisfiability (3-SAT) problem instance, into a qubit array structure for the maximum independent set (MIS) problem instance intrinsic to Rydberg atom quantum experiments. These quantum algorithms are experimentally evaluated on 3-SAT problem instances using Rydberg blockade and adiabatic quantum processes. We then introduce Rydberg Quantum-enhanced simulated annealing (QESA), a software combination with quench evolution (QE) and adiabatic quantum computing (AQC) experimental data that significantly reduces processing time and improves accuracy over classical methods. QESA demonstrates an efficient performance advantage over simulated annealing (SA) to reach a target approximation ratio.

Keywords Quantum computational problem, Rydberg atom, Quantum wire, Quantum gates, Satisfiability problem, Maximum independent set problem, Adiabatic quantum computing, Hybrid Quantum-classical algorithm

Contents

List of Tables

List of Figures

Chapter 1.   Introduction

Quantum physics is the overarching theory that describes the microscopic nature of physical systems. Quantum computing, in particular, has attracted attention as a means to innovate computational power beyond the limits of classical digital computers [1, 2]. As a type of quantum computing, gate-based quantum computation has been demonstrated in many physical systems, including hardware systems, linear optics [3, 4], quantum mechanics of superconducting circuits [5, 6, 7], trapped ions [8, 9, 10], defects in solid materials [11, 12], and neutral atoms [13, 14]. Neutral atoms have been considered for gate-based quantum computation using interactions between Rydberg atoms [15, 16]. The advantages of using Rydberg atoms include strong dipole-dipole interactions and laser excitations that can be turned on and off at high speeds, large arrays of atoms that can be prepared in almost any desired geometry and topology [17, 18, 19], and stable ground hyperfine states that can be used for long-term quantum information. Quantum gates using Rydberg atoms can take advantage of distance-dependent interactions [20] or the Rydberg blockade effect [21, 22], which prohibits adjacent atoms from being excited to the Rydberg state. There are many Rydberg atomic schemes for quantum gates and entanglement [23, 24, 25, 26], which have been experimentally demonstrated [27, 28, 29, 30, 31, 32, 33]. This thesis investigates the potential of Rydberg atom system as a quantum computer. Rydberg atom system controls individual atoms with optical tweezers and can accurately manipulate the distance between pairs of atoms. It also offers graphs with Rydberg blockade property, which causes strong correlations between atoms. This thesis proposes three types of quantum programming that utilize these properties of Rydberg quantum systems. Chapter 2 introduces the physical meaning of the Rydberg atom array, the definition of the maximum independent set (MIS) problem, and the Rydberg experimental setup. In Chapter 3, we show that various Rydberg quantum gate schemes can be designed with auxiliary atoms (wire atoms) and optical local atom addressing. By using auxiliary atoms, we have solved the quantum gate problem due to the Rydberg blockade. In addition to solving the quantum gate, the auxiliary atom helps to overcome the geometrical limitations by introducing an additional atom, the wire, between two unconnected atoms, which will be discussed later in constructing the quantum graph. Then, in Chapter 4, we present quantum algorithms and programming for the transformation of mathematical problems intractable to classical computers into Rydberg quantum graphs. To solve NP problem instances, we formulate a quantum programming algorithm for Rydberg atom array that evaluates the satisfiability (i.e., existence of a solution) of a 3-satisfiability (3-SAT) instance. We present an algorithm that reduces the 3-SAT problem to a maximum independent set (MIS) problem with Rydberg atom blockade interactions, and then experimentally obtain satisfiability results for SAT graph instances obtained by adiabatic quantum computing (AQC). Chapter 5 is on the hybrid quantum-classical programming, which we refer to as quantum enhanced simulated annealing (QESA). It is essential to decrease the number of iterations of the quantum adiabatic process to achieve quantum supremacy in current Rydberg quantum systems. This requires simultaneously improving the quality (noise) and scalability (number of atoms) issues. To solve this problem, we propose an approach that combines experimental results with software to obtain high precision with low processing time. We show the results of QESA based on experimental results of AQC or quench evolution (QE) of Rydberg atom arrays of approximately one hundred atoms. We show the computational time advantage over classical stand-alone simulated annealing (SA), and in particular, we present a new correlation between the computational time and Hamming distance of QESA. From

these results, we also estimate the scalability of QESA in terms of the number of atoms and Hamming distance. Chapter 6 is the conclusion of the previous chapters on three types of quantum programming. We present a quantum gate using Rydberg wires, programming that converts NP-complete instances into a qubit array structure for Rydberg atom quantum experiments, and describe the effectiveness of warm-start software coupling of preliminary Rydberg quantum experiment results using Hamming distance to improve performance and accuracy.

Chapter 2.   Review of Rydberg atom Quantum Programming

Quantum programming is the process of designing and executing algorithms that operate on quantum computers [34, 35]. Whereas classical programming is digital, using binary (0 and 1) bits, quantum programming uses qubits, which represent superpositions and entanglement [34, 35].

The scope of quantum programming can be quite broad, and, particularly in this thesis, we will discuss three different kinds of quantum programming:

1. Quantum circuit model programming: Design of the universal quantum gates intrinsic to the 2D ground-Rydberg qubit system consisting of the data and auxiliary qubits.

2. Adiabatic quantum programming: Converting an NP-complete instance into a qubit array structure to suit the problem so that the Rydberg atomic quantum experiment can be performed.

3. Hybrid quantum-classical programming: Software combination of Rydberg quantum experimental results using Hamming distance to improve accuracy, which will be discussed later.

In this chapter, we will briefly introduce the basic principles and properties of Rydberg atoms used in quantum programming, the maximum independent set (MIS) problem, and Rydberg atom experimental setup.

2.1   Theoretical basic of Rydberg atom arrays

A Rydberg atom is a neutral atom (e.g. Rubidium or Cesium) in which one or more electrons are excited to a high principal quantum number n (typically, $n \gtrsim 30$ [15, 36]), and has the following properties:

1. Strong, long-range interactions [15],

2. Large electric dipole moments [15],

3. High sensitivity to external fields [36, 37].

Strong dipole-dipole interactions lead to Rydberg blockade, a phenomenon in which the excitation of one atom prevents the excitation of neighboring atoms [15]. And the high sensitivity to external fields leads to strong coupling between the ground and excited states by the laser, which facilitates the transition between states. In quantum computing, where qubits are encoded into the ground and excited states of an atom, this Rydberg blockade and strong interstate coupling provide high controllability and entanglement.

In addition, the high sensitivity of a single atom to external fields enables optical tweezer [37], which traps a single atom in a far-off-resonance optical trap (FORT) created by a far-off-resonant beam at a targeted location. These optical tweezers provide an environment for creating scalable and reconfigurable quantum computing [38].

In this section, we describe in detail the following physical properties of the Rydberg atom. First, we introduce how the high sensitivity to external fields of the Rydberg atom and the strong dipole-dipole

interaction are reflected in the Hamiltonian of the Rydberg atom system. Then, we describe the Rydberg blockade, which allows the Rydberg atom system to provide high controllability and entanglement for quantum computing. Finally, we introduce the Lindblad master equation, a model that describes the decoherence that occurs in the Rydberg atom system.

2.1.1 Hamiltonian of Rydberg atom system

The quantum Hamiltonian of the Rydberg atom system is represented as follows:

$$\hat{H}_{\text{Ryd}} = \hat{H}_{\text{g}-\text{R}} + \hat{H}_{\text{R}-\text{R}}. \tag{2.1}$$

where $\hat{H}_{g-R}$ is the term that represents the two-photon transition between the ground and Rydberg states of each atom, and $\hat{H}_{R-R}$ is the Rydberg-Rydberg interaction term acting between the Rydberg states of two spatially distant atoms.

In this subsection, $\hat{H}_{\text{Ryd}}$ is described in two parts: "Two-photon transition between ground and Rydberg states" and "Rydberg-Rydberg interaction" related to the Rydberg blockade phenomenon.

Two-photon transition between the ground and Rydberg states

The transition between the ground and Rydberg states of a single atom occurs as a two-photon transition due to the atom-light interaction between the atom and the laser, which is an external field. This two-photon transition can be explained by a three-level system consisting of a ground state $|g\rangle$, an intermediate state $|i\rangle$, and a Rydberg state $|R\rangle$, as shown in Fig. 2.1.

And this two-photon transition occurs through the coupling between the $|g\rangle$-$|i\rangle$ state by the laser beam L1 and the coupling between the $|i\rangle$-$|R\rangle$ state by the laser beam L2. And, for $|R\rangle = \left|nS_{1/2}, m_J = 1/2\right\rangle$ where each coupling by laser beams L1 and L2 can be viewed as a strict one-photon transition in the two-level system $\{|g\rangle, |i\rangle\}$ [15, 39, 40] and an approximate one-photon transition in the two-level system $\{|i\rangle, |R\rangle\}$ (where $|R\rangle$ has a negligible hyperfine splitting) [15, 36, 41], respectively.

This two-level system is represented by the Hamiltonian $\hat{H}_{\text{Two}-\text{level}}$ (Eq. (2.3)) with two parameters one-photon Rabi frequency Ω_{ab} and detuning Δ by the *Electric dipole approximation* and the *Rotating wave approximation* (RWA), since it is a two-level system is a two-level system $\{|a\rangle, |b\rangle\}$ with energy $\{\hbar\omega_a, \hbar\omega_b\}$ ($\omega_{b-a} = \omega_b - \omega_a$) and transition dipole $\vec{\mu}$, where each level is acted upon by a laser in an electric field $\vec{E}$ oscillating with an angular frequency $\omega_L(\equiv 2\pi c/\lambda_L)$ with a wavelength $\lambda_L(\gg a_0)$ much larger than the typical atom size ($\sim a_0$, $a_0 = 5.2918 \times 10^{-11}$ m is Bohr radius):

$$\Omega_{ab} \equiv -\vec{\mu} \cdot \vec{E}/\hbar \tag{2.2a}$$

$$\Delta \equiv \omega_L - \omega_{b-a} \tag{2.2b}$$

$$\hat{H}_{\text{Two}-\text{level}} = \frac{\hbar}{2} \begin{bmatrix} 0 & \Omega_{ab}^* \\ \Omega_{ab} & -2\Delta \end{bmatrix}. \tag{2.3}$$

Based on this, the Hamiltonian of the three-level system $\{|g\rangle, |i\rangle, |R\rangle\}$ is expressed as Eq. (2.4):

$$\hat{H}_{\text{Three}-\text{level}} = \frac{\hbar}{2} \begin{bmatrix} 0 & \Omega_{gi}^* & 0 \\ \Omega_{gi} & -2\Delta_{m1} & \Omega_{iR}^* \\ 0 & \Omega_{iR} & -2(\Delta_{m1} + \Delta_{m2}) \end{bmatrix}, \tag{2.4}$$

4
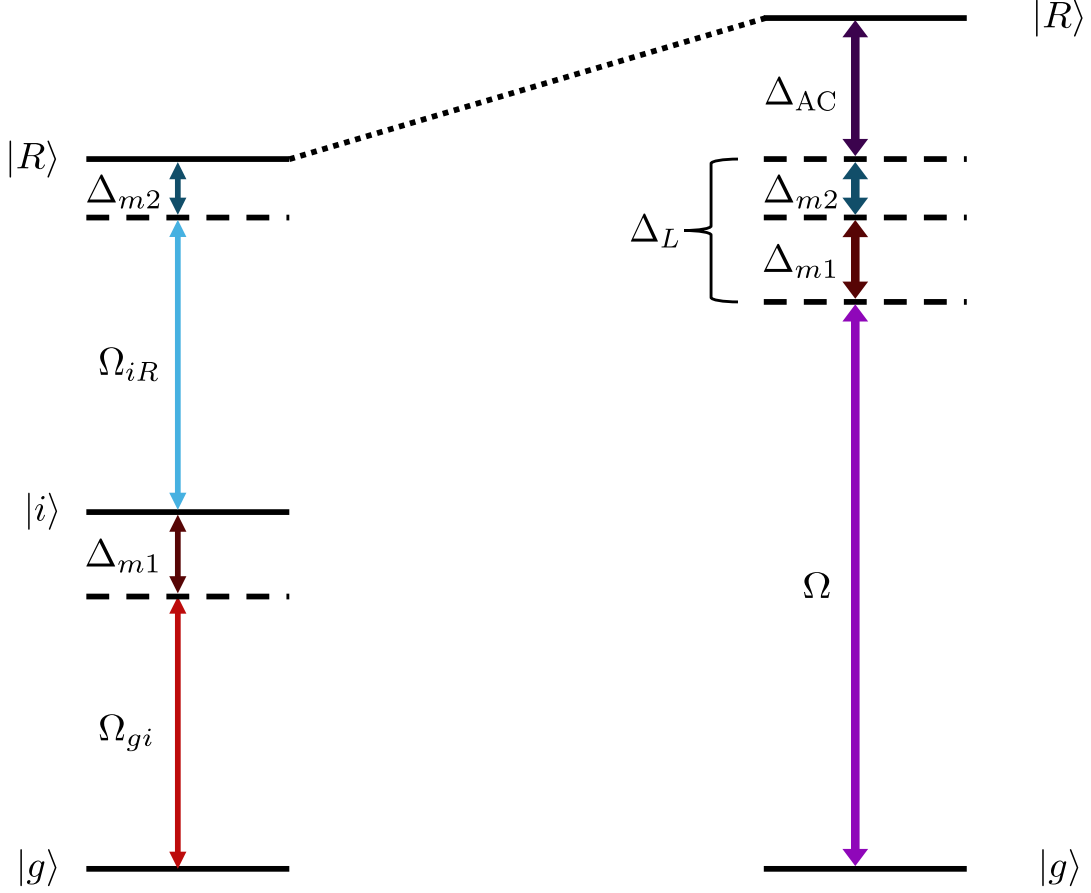
Figure 2.1: Two-photon transition in the three-level System $\{|g\rangle, |i\rangle, |R\rangle\}$ (which are ground-, intermediate- and Rydberg states), From the *Electric dipole approximation* and *Rotating wave approximation* (RWA), there are a strict- and an approximate one-photon transition in each two-level system $\{|g\rangle, |i\rangle\}$ (red-colored in the left diagram) and $\{|i\rangle, |R\rangle\}$ (blue-colored in the left diagram). And, by the *Adiabatic elimination*, These two one-photon transitions in the three-level System $\{|g\rangle, |i\rangle, |R\rangle\}$ leads to the two-photon transition (purple-colored in the right diagram) between $|g\rangle$ and $|R\rangle$ states.

where $(\Omega_{gi}, \Delta_{m1}) \equiv (-\vec{\mu}_{gi} \cdot \vec{E}_{L1}/\hbar, \omega_{L1} - \omega_{i-g})$, $(\Omega_{iR}, \Delta_{m2}) \equiv (-\vec{\mu}_{iR} \cdot \vec{E}_{L2}/\hbar, \omega_{L2} - \omega_{R-i})$ are the (One-photon Rabi frequency, Detuning) pair of each laser beam acting on the $|g\rangle$-$|i\rangle$ state transition and the $|i\rangle$-$|R\rangle$ state transition, respectively.

So, the Schrödinger equation for the three-level system is given as follows:

$$i\hbar \begin{bmatrix} \dot{c}_g(t) \\ \dot{c}_i(t) \\ \dot{c}_R(t) \end{bmatrix} = \frac{\hbar}{2} \begin{bmatrix} 0 & \Omega_{gi}^* & 0 \\ \Omega_{gi} & -2\Delta_{m1} & \Omega_{iR}^* \\ 0 & \Omega_{iR} & -2(\Delta_{m1} + \Delta_{m2}) \end{bmatrix} \cdot \begin{bmatrix} c_g(t) \\ c_i(t) \\ c_R(t) \end{bmatrix} \quad (2.5)$$

In Eq. (2.5), if the intermediate detuning Δ_{m1} is much larger than the other parameters $\Omega_{gi}, \Omega_{iR}, (\Delta_{m1} + \Delta_{m2})$ (i.e. $|\Delta_{m1}| \gg |\Omega_{gi}|, |\Omega_{iR}|, |\Delta_{m1} + \Delta_{m2}|$), it can be approximated as $\dot{c}_i(t) \approx 0$ by the *adiabatic elimination* [42].

By the Eq. (2.5) and *Adiabatic elimination*, the following relation is obtained:

$$2i\dot{c}_i(t) = \Omega_{gi}c_g(t) - 2\Delta_{m1}c_i(t) + \Omega_{iR}^*c_R(t) \approx 0 \tag{2.6a}$$

$$c_i(t) \approx \frac{\Omega_{gi}c_g(t) + \Omega_{iR}^*c_R(t)}{2\Delta_{m1}} \tag{2.6b}$$

Substituting Eq. (2.6b) to Eq. (2.5), it is clear that Eq. (2.5) can be approximated by the following two-level Schrödinger equation:

$$i\hbar \begin{bmatrix} \dot{c}_g(t) \\ \dot{c}_R(t) \end{bmatrix} = \frac{\hbar}{2} \begin{bmatrix} \frac{|\Omega_{gi}|^2}{2\Delta_{m1}} & \frac{\Omega_{gi}^*\Omega_{iR}^*}{2\Delta_{m1}} \\ \frac{\Omega_{gi}\Omega_{iR}}{2\Delta_{m1}} & \frac{|\Omega_{iR}|^2}{2\Delta_{m1}} - 2(\Delta_{m1} + \Delta_{m2}) \end{bmatrix} \cdot \begin{bmatrix} c_g(t) \\ c_R(t) \end{bmatrix}. \tag{2.7}$$

The new parameters are the two-photon Rabi frequency Ω, the AC Stark shift Δ_{AC}, and the total detuning Δ_L, defined as follows:

$$\Omega \equiv \frac{\Omega_{gi}\Omega_{iR}}{2\Delta_{m1}} \tag{2.8a}$$

$$\Delta_{\mathrm{AC}} \equiv \frac{|\Omega_{gi}|^2 - |\Omega_{iR}|^2}{4\Delta_{m1}} \tag{2.8b}$$

$$\Delta_L \equiv \Delta_{m1} + \Delta_{m2} \tag{2.8c}$$

Consequently, the two-photon transition in Eq. (2.7) is approximated as the two-level system $\{|g\rangle, |R\rangle\}$, and the Hamiltonian $\hat{H}_{g-R}$, which represents the two-photon transition between the ground and Rydberg states of each atom, is obtained as follows:

$$\hat{H}_{\mathrm{g-R}} = \hbar \sum_j \left(\frac{\Omega}{2}\hat{\sigma}_j^x - \Delta\hat{n}_j \right), \tag{2.9}$$

where $\Delta \equiv \Delta_{\mathrm{AC}} + \Delta_L$ is the detuning, Ω is the (Two-photon) Rabi frequency, $\hat{\sigma}_j^x \equiv |g\rangle_j \langle R|_j + |R\rangle_j \langle g|_j$ is the Pauli x operator acting on the j-th atom, and $\hat{n}_j \equiv |R\rangle_j \langle R|_j$ is the Rydberg occupation number operator of the j-th atom.

Rydberg-Rydberg interaction

In this subsection, we will discuss the Rydberg-Rydberg interaction between the Rydberg states of two atoms spatially distant from each other. Rydberg state is a state in which one or more electrons of a neutral atom are excited to a high principal quantum number, $n \,(\gtrsim 30)$, and have large electric dipole moments [36]. Hence, there is a dipole-dipole interaction between the Rydberg states of atoms A and B, located at positions $\vec{R}_A$ and $\vec{R}_B$ and distant from each other, which is given as follows:

$$\hat{U}_{D-D} = \frac{1}{4\pi\epsilon_0} \frac{\vec{\mu}_A \cdot \vec{\mu}_B - 3(\vec{\mu}_A \cdot \hat{R})(\vec{\mu}_B \cdot \hat{R})}{d^3}, \tag{2.10}$$

where d is the distance between two atoms A and B, $\vec{\mu}_{A(B)}$ is the electric dipole moment of each atom, and $\hat{R} = \vec{R}/d$ $(\vec{R} \equiv \vec{R}_A - \vec{R}_B)$.

This dipole-dipole interaction $\hat{U}_{d-d}$ induces a $|r_A, r_B\rangle$-$|r_A', r_B'\rangle$ transition of the Rydberg state pair $|r_A, r_B\rangle$ of atoms A, B. The following perturbative energy shift $\Delta E_{r_A, r_B}$ of $\hat{U}_{d-d}$ is applied between the two distant atoms:

$$\begin{aligned} \Delta E_{r_A, r_B} &\approx \Delta E_{r_A, r_B}^{(1)} + \Delta E_{r_A, r_B}^{(2)} \\ &= \langle r_A, r_B| \hat{U}_{D-D} |r_A, r_B\rangle + \sum_{r_A' \neq r_A, r_B' \neq r_B} \frac{|\langle r_A, r_B| \hat{U}_{D-D} |r_A', r_B'\rangle|^2}{E_{r_A, r_B} - E_{r_A', r_B'}} \end{aligned} \tag{2.11}$$
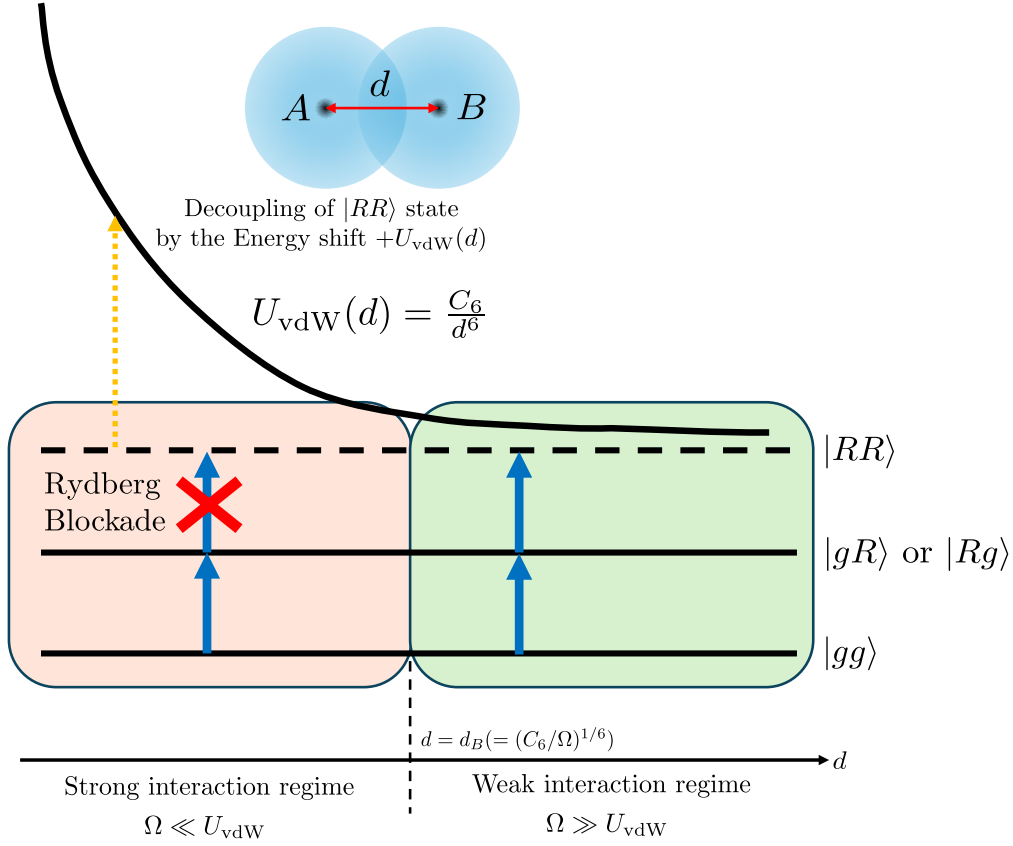
Figure 2.2: Rydberg-Rydberg Interaction $U_{\mathrm{vdW}}(d)$ of two atoms A and B at a distance d and the Rydberg Blockade due to the decoupling of $|RR\rangle$ state by the energy shift $+U_{\mathrm{vdW}}(d)$ at the strong interaction regime ($d \ll d_B = (C_6/\Omega)^{1/6}$)

Here, since the orbital function is point symmetric with respect to the origin, the first order perturbation energy is $\Delta E^{(1)}_{r_A, r_B} = \langle r_A, r_B | \hat{U}_{d-d} | r_A, r_B \rangle = 0$. Thus, the perturbative energy shift $\Delta E_{r_A, r_B}$ can be approximated by the second order perturbation energy $\Delta E^{(2)}_{r_A, r_B}$, which is called the **van der Waals interaction**:

$$\Delta E_{r_A, r_B} \approx \Delta E^{(2)}_{r_A, r_B} = \sum_{r'_A \neq r_A, r'_B \neq r_B} \frac{|\langle r_A, r_B | \hat{U}_{D-D} | r'_A, r'_B \rangle|^2}{E_{r_A, r_B} - E_{r'_A, r'_B}} = \hbar \frac{C_6}{d^6}, \tag{2.12}$$

where C_6 is the van der Waals interaction coefficient and R is the distance between two atoms A and B.

Consequently, the Hamiltonian $\hat{H}_{\mathrm{vdW}}(d)$ of the Rydberg-Rydberg interaction of two atoms A, B at a distance d is expressed as Eq. (2.13a), and the Hamiltonian $\hat{H}_{\mathrm{R-R}}$ representing the Rydberg-Rydberg interactions between these different atoms is given by Eq. (2.13b):

$$\hat{H}_{\mathrm{vdW}}(d) = \hbar \frac{C_6}{d^6} \hat{n}_A \hat{n}_B, \tag{2.13a}$$

$$\hat{H}_{\mathrm{R-R}} = \sum_{j<k} \hat{H}_{\mathrm{vdW}}(r_{jk}) = \hbar \sum_{j<k} \frac{C_6}{r_{jk}^6} \hat{n}_j \hat{n}_k, \tag{2.13b}$$

where r_{jk} is the distance between the j-th and k-th atoms, and $\hat{n}_j \equiv |R\rangle_j \langle R|_j$ is the Rydberg occupation number operator of the j-th atom.

2.1.2 Rydberg blockade

Using the Eq. (2.1), Eq. (2.9) and Eq. (2.13b) in the Subsec. 2.1.1, the quantum Hamiltonian of the Rydberg atom system is finally obtained as follows:

$$\hat{H}_{\mathrm{Ryd}} = \hbar \left[\sum_j \left(\frac{\Omega}{2} \hat{\sigma}_j^x - \Delta \hat{n}_j \right) + \sum_{j<k} \frac{C_6}{r_{jk}^6} \hat{n}_j \hat{n}_k \right].$$

(2.14)

As shown in Figure 2.2, the energy level of the double-excitation state $|RR\rangle$ is shifted by $+U_{\mathrm{vdW}}$ compared to $\hat{H}_{g-R}$ by the van der Waals interaction, a Rydberg-Rydberg interaction between atoms A and B at a distance R from each other.

Also, in the strong interaction regime ($\Omega \ll U_{\mathrm{vdW}}$), where the energy shift of the $|RR\rangle$ state is much larger than the Rabi frequency, the $|RR\rangle$ state is decoupled from the dynamics of the Hamiltonian $\hat{H}_{\mathrm{Ryd}}$ by the energy shift U_{vdW}, which is called **Rydberg blockade**. The strong interaction regime, where this Rydberg blockade occurs, and the weak interaction regime, outside of the strong interaction regime, is based on whether the distance d between two atoms is within the Rydberg blockade distance $d_B = (C_6/\Omega)^{1/6}$ (Fig. 2.2).

2.1.3 Lindblad master equation

The quantum Hamiltonian $\hat{H}_{\mathrm{Ryd}}$ (Eq. (2.14)) of the Rydberg atom system, described in 2.1.1 and utilized in Subsection 2.1.2, shows how the "external electric field of the laser" and the "van der Waals interaction derived from the dipole-dipole interaction between atoms" act on the Rydberg atom system, and can be used to control the Rydberg atom system.

However, unwanted noise from the *Environment*, which is external to the *System* we are focusing on, causes decoherence in the dynamics of $\hat{H}_{\mathrm{Ryd}}$. Therefore, we use the Lindblad master equation (Eq. (2.15b)), which is formed by adding the Lindblad superoperator $\hat{\mathcal{L}}(\rho)$ representing the decoherence of the *System* by the *Environment* to the Schrödinger equation (Eq. (2.15a)), which is a representation of the dynamics of $\hat{H}_{\mathrm{Ryd}}$ with respect to the density matrix ρ of the *System*:

$$\text{Schrödiger equation:} \quad \frac{\partial \rho}{\partial t} = \frac{i}{\hbar} \left[\rho(t), \hat{H}_{\mathrm{Ryd}}(t) \right]$$

(2.15a)

$$\text{Lindblad master equation:} \quad \frac{\partial \rho}{\partial t} = \frac{i}{\hbar} \left[\rho(t), \hat{H}_{\mathrm{Ryd}}(t) \right] + \hat{\mathcal{L}}(\rho(t)).$$

(2.15b)

And the Lindblad superoperator $\hat{\mathcal{L}}(\rho)$ is expressed as a function of the Lindblad jump operator $\hat{L}_m$ ($1 \le m \le M \le 2^N - 1$) [43]:

$$\hat{\mathcal{L}}(\rho) = \sum_{m=1}^M \left(\hat{L}_m \rho \hat{L}_m^\dagger - \frac{1}{2} \left\{ \hat{L}_m^\dagger \hat{L}_m, \rho \right\} \right).$$

(2.16)

In the case of a Rydberg atom system, the *System* is the two-level system $\{|g\rangle, |R\rangle\}$ and the *Environment* is the remaining states including the intermediate state $|i\rangle$ in the two-photon transition, typical examples of the noise that this *Environment* contributes to the *System* are the spontaneous decay of the intermediate state $|i\rangle$ to the ground state $|g\rangle$ (Fig. 2.3) and the spontaneous decay of the Rydberg state $|R\rangle$. Since the Rydberg state lifetime of an ^{87}Rb atom ($\tau_R \gtrsim 150 \ \mu$s) [44] is about 10^4 times longer than the lifetime of the intermediate state $\tau_i = 1/\Gamma \approx 30$ ns (Decay rate of the $5P_{3/2}$ state of ^{87}Rb: $\Gamma = 2\pi \times 6$ MHz), decoherence is primarily related to the spontaneous decay of the intermediate
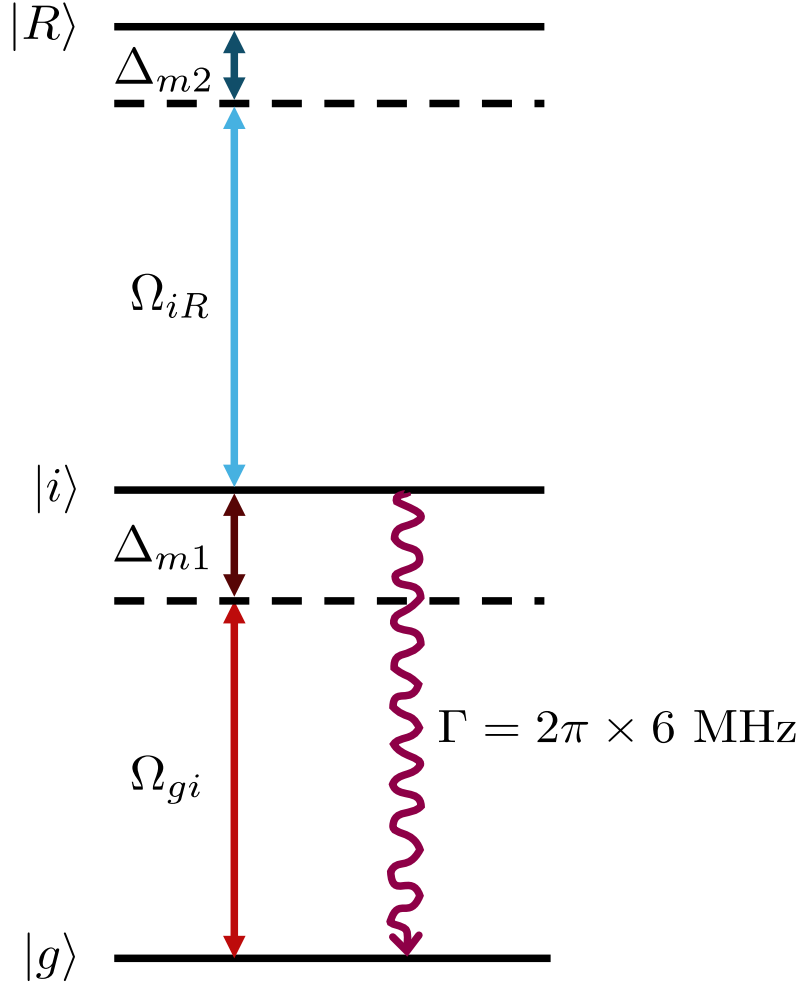
Figure 2.3: Three level system with the spontaneous decay of the intermediate state $|i\rangle$.

state $|i\rangle \left(= \left|5P_{3/2}\right\rangle\right)$. The Lindblad jump operator $\hat{L}_{\text{Three-level}}$ for the three-level system $\{|g\rangle, |i\rangle, |R\rangle\}$ represents this as follows:

$$\hat{L}_{\text{Three-level}} = \begin{bmatrix} 0 & \sqrt{\Gamma} & 0 \\ 0 & 0 & 0 \\ 0 & 0 & 0 \end{bmatrix} = \sqrt{\Gamma} |g\rangle \langle i| \tag{2.17}$$

The Lindblad superoperator $\mathcal{L}_{\text{Three-level}}(\rho(t))$ resulting from this is given by the Eq. (2.18a), and the Lindblad master equation for the three-level system is given by the Eq. (2.18b):

$$\mathcal{L}_{\text{Three-level}}(\rho(t)) = \hat{L}_{\text{Three-level}}\rho(t)\hat{L}_{\text{Three-level}}^{\dagger} - \frac{1}{2}\left\{\hat{L}_{\text{Three-level}}^{\dagger}\hat{L}_{\text{Three-level}}, \rho(t)\right\}, \quad (2.18a)$$

$$\frac{\partial \rho}{\partial t} = \frac{i}{\hbar}\left[\rho(t), \hat{H}_{\text{Three-level}}(t)\right] + \mathcal{L}_{\text{Three-level}}(\rho(t)). \tag{2.18b}$$

From Eq. (2.18b), the following relations are obtained:

$$
\begin{aligned}
\dot{\rho}_{gg} &= \frac{i}{2}\left[\Omega_{gi}\rho_{ig}^* - \Omega_{gi}^*\rho_{ig}\right] + \Gamma\rho_{ii} \\
&= \mathrm{Im}(\Omega_{gi}^*\rho_{ig}) + \Gamma\rho_{ii},
\end{aligned} \tag{2.19a}
$$

$$
\begin{aligned}
\dot{\rho}_{ii} &= \frac{i}{2}\left[\left(\Omega_{gi}^*\rho_{ig} + \Omega_{iR}\rho_{Ri}^*\right) - \left(\Omega_{gi}\rho_{ig}^* + \Omega_{iR}^*\rho_{Ri}\right)\right] - \Gamma\rho_{ii} \\
&= \mathrm{Im}(\Omega_{iR}^*\rho_{Ri} - \Omega_{gi}^*\rho_{ig}) - \Gamma\rho_{ii},
\end{aligned} \tag{2.19b}
$$

$$
\begin{aligned}
\dot{\rho}_{RR} &= \frac{i}{2}\left[\Omega_{iR}^*\rho_{Ri} - \Omega_{iR}\rho_{Ri}^*\right] \\
&= -\mathrm{Im}(\Omega_{iR}^*\rho_{Ri}),
\end{aligned} \tag{2.19c}
$$

$$
\begin{aligned}
\dot{\rho}_{ig} &= \frac{i}{2}\left[\Omega_{gi}\left(\rho_{ii} - \rho_{gg}\right) + 2\Delta_{m1}\rho_{ig} - \Omega_{iR}^*\rho_{Rg}\right] - \frac{\Gamma}{2}\rho_{ig} \\
&= \frac{i}{2}\left[\Omega_{gi}\left(\rho_{ii} - \rho_{gg}\right) - \Omega_{iR}^*\rho_{Rg}\right] + i\Delta_{m1}\rho_{ig} - \frac{\Gamma}{2}\rho_{ig},
\end{aligned} \tag{2.19d}
$$

$$
\begin{aligned}
\dot{\rho}_{Rg} &= \frac{i}{2}\left[\Omega_{gi}\rho_{Ri} - \Omega_{iR}\rho_{ig} + 2\left(\Delta_{m1} + \Delta_{m2}\right)\rho_{Rg}\right] \\
&= \frac{i}{2}\left[\Omega_{gi}\rho_{Ri} - \Omega_{iR}\rho_{ig}\right] + i\Delta_L\rho_{Rg},
\end{aligned} \tag{2.19e}
$$

$$
\begin{aligned}
\dot{\rho}_{Ri} &= \frac{i}{2}\left[\Omega_{gi}^*\rho_{Rg} + \Omega_{iR}\left(\rho_{RR} - \rho_{ii}\right) - 2\Delta_{m1}\rho_{Ri} + 2\left(\Delta_{m1} + \Delta_{m2}\right)\rho_{Ri}\right] - \frac{\Gamma}{2}\rho_{Ri} \\
&= \frac{i}{2}\left[\Omega_{gi}^*\rho_{Rg} + \Omega_{iR}\left(\rho_{RR} - \rho_{ii}\right)\right] + i\Delta_{m2}\rho_{Ri} - \frac{\Gamma}{2}\rho_{Ri}.
\end{aligned} \tag{2.19f}
$$

From the conditions of $|\Delta_{m1}| \gg |\Omega_{gi}|, |\Omega_{iR}|, |\Delta_{m1} + \Delta_{m2}|$ (i.e., $|\Delta_{m1}| \gg |\Omega_{gi}|, |\Omega_{iR}|$ and $\Delta_{m1} \sim -\Delta_{m2}$), we can let $\dot{\rho}_{ii} \approx 0$, $\dot{\rho}_{ig} \approx 0$, $\dot{\rho}_{Ri} \approx 0$ via *adiabatic elimination* as in Eqs. (2.6), and we get the relation as in Eqs. (2.20):

$$
\rho_{ii} \sim \frac{|\Omega_{iR}|^2\rho_{RR} + |\Omega_{gi}|^2\rho_{gg}}{4\Delta_{m1}^2} \approx 0 \tag{2.20a}
$$

$$
\rho_{ig} \sim -\frac{\Omega_{gi}\left(\rho_{ii} - \rho_{gg}\right) - \Omega_{iR}^*\rho_{Rg}}{2\Delta_{m1}} + i\Gamma\frac{\Omega_{gi}\left(\rho_{ii} - \rho_{gg}\right) - \Omega_{iR}^*\rho_{Rg}}{4\Delta_{m1}^2} \tag{2.20b}
$$

$$
\rho_{Ri} \sim \frac{\Omega_{gi}^*\rho_{Rg} + \Omega_{iR}\left(\rho_{RR} - \rho_{ii}\right)}{2\Delta_{m1}} + i\Gamma\frac{\Omega_{gi}^*\rho_{Rg} + \Omega_{iR}\left(\rho_{RR} - \rho_{ii}\right)}{4\Delta_{m1}^2} \tag{2.20c}
$$

Accordingly, Eq. (2.18b) can be approximated as Eqs. (2.21) for the two-level system $\{|g\rangle, |R\rangle\}$:

$$
\dot{\rho}_{gg} \sim -\frac{i}{2}\left[\frac{\Omega_{gi}^*\Omega_{iR}^*}{2\Delta_{m1}}\rho_{Rg} - \frac{\Omega_{gi}\Omega_{iR}}{2\Delta_{m1}}\rho_{Rg}^*\right] \tag{2.21a}
$$

$$
= -\frac{i}{2}\left(\Omega^*\rho_{Rg} - \Omega\rho_{Rg}^*\right) \tag{2.21b}
$$

$$
\dot{\rho}_{RR} \sim \frac{i}{2}\left[\frac{\Omega_{gi}^*\Omega_{iR}^*}{2\Delta_{m1}}\rho_{Rg} - \frac{\Omega_{gi}\Omega_{iR}}{2\Delta_{m1}}\rho_{Rg}^*\right] \tag{2.21c}
$$

$$
= \frac{i}{2}\left(\Omega^*\rho_{Rg} - \Omega\rho_{Rg}^*\right) \tag{2.21d}
$$

$$
\dot{\rho}_{Rg} \sim i\frac{\Omega}{2}\left(\rho_{RR} - \rho_{gg}\right) + \left[i\Delta - \frac{\Gamma\left(|\Omega_{gi}|^2 + |\Omega_{iR}|^2\right)}{8\Delta_{m1}^2}\rho_{Rg}\right]\rho_{Rg} \tag{2.21e}
$$

$$
= i\frac{\Omega}{2}\left(\rho_{RR} - \rho_{gg}\right) + \left(i\Delta - \gamma_i\right)\rho_{Rg}, \tag{2.21f}
$$

where γ_i is the individual dephasing rate, defined as following:

$$
\gamma_i \equiv \frac{\Gamma\left(|\Omega_{gi}|^2 + |\Omega_{iR}|^2\right)}{8\Delta_{m1}^2}. \tag{2.22}
$$

Then, the N-atom Rydberg atom system with Eqs. (2.21) is represented by the two-level Lindblad equation (Eq. (2.23b)), which accounts for the decoherence of the Lindblad superoperator defined by the

Eq. (2.23a):

$$\hat{\mathcal{L}}_{\text{ind}}(\rho) \ = \ \sum_{j=1}^{N} \left(L_j \rho L_j^\dagger - \frac{1}{2} \left\{ L_j^\dagger L_j, \rho \right\} \right), \tag{2.23a}$$

$$\frac{\partial \rho}{\partial t} \ = \ \frac{i}{\hbar} \left[\rho(t), \hat{H}_{\text{Ryd}}(t) \right] + \hat{\mathcal{L}}_{\text{ind}}(\rho), \tag{2.23b}$$

where $L_j = \sqrt{\gamma_i/2} \sigma_z^{(j)}$ is the Lindblad jump operator representing the individual dephasing of Eqs. (2.21) for the j-th atom.

2.2 Maximum Independent Set (MIS) Problem

The amount of resources required by a computational algorithm to solve a given computational problem, such as the number of steps required for computation, memory usage, etc. is known as **Computational Complexity** [45]. This computational complexity is an important measure of the possibility of efficiently solving a computational problem [45], and it plays the following roles:

1. Tractability (Inherent Difficulty) of Problem: An implication of algorithmic limit as the existence of a tractable (efficiently solvable) algorithm for a given problem [45].

2. Computational limit: Formalization of the kinds and maximum size of problems that can be solved within limited resources [46].

3. Guide for Algorithm Design and Presenting Cryptography Foundation: A guide to algorithm design, including resource allocation methods for exact or approximate algorithms [47], and a presentation of the basics of cryptographic system security that depends on the difficulty of the problem [48].

4. Formalization of Problem Reduction: Providing a formalized way to compare the difficulty of problems using Problem Reduction [49].

Computational complexity is divided into time complexity and space complexity depending on the type of resources such as time (number of steps required for computation) and space (amount of memory required). And a representative example of complexity classes that classify computational complexity is shown in Table 2.1, and the definitions of complexity classes shown in this table are as follows:

1. **P** (Polynomial Time): Problems that are solvable by a deterministic Turing machine (DTM) in polynomial time $O(poly(N))$ and are considered efficiently solvable [45]. Examples are Sorting, Finding Shortest Path, etc.

2. **NP** (Nondeterministic Polynomial Time): Problems that can be solved by a nondeterministic Turing machine (NTM) in polynomial time $O(poly(N))$ and whose solution can be verified by a Deterministic Turing machine in polynomial time [45]. Some examples include Satisfiability (SAT), Hamiltonian Path, Traveling Salesman, and Maximum Independent Set (MIS).

3. **EXPTIME** (Exponential Time): The set of problems that can be solved by DTM in exponential time $O(2^{poly(N)})$, with solving difficulty equal to or harder than that of an NP problem [45, 46, 50]. Typical examples include Generalized Chess, Checkers, and Go on unbounded boards.

Table 2.1: Classification of Computational complexity, **BPP** is the complexity class of decision problems solvable via a probabilistic Turing machine (PTM), a type of nondeterministic Turing machine (NTM)

Resource	Computational model	Complexity class	Complexity scale
Time	Deterministic Turing machine (DTM)	**P**	$O(poly(N))$
		EXPTIME	$O(2^{poly(N)})$
	Nondeterministic Turing machine (NTM)	**NP**	$O(poly(N))$
		NEXPTIME	$O(2^{poly(N)})$
		BPP	$O(poly(N))$
Space	Deterministic Turing machine (DTM)	**PSPACE**	$O(poly(N))$ space)
		EXPSPACE	$O(2^{poly(N)}$ space)
	Nondeterministic Turing machine (NTM)	**NPSPACE**	$O(2^{poly(N)}$ space)
		NEXPSPACE	$O(poly(N)$ space)

4. **NEXPTIME** (Nondeterministic Exponential Time): Problems solvable by NTM in exponential time $O(2^{poly(N)})$, including the **EXPTIME** class [46, 51].

5. **BPP** (Bounded-error Probabilistic Polynomial Time): Problems that can be solved by a Probabilistic Turing machine (PTM), a type of NTM, in polynomial time with an error probability of 1/3 or less [46, 48].

6. **PSPACE** (Polynomial Space): Problems that can be solved in DTM using the polynomial memory space $O(poly(N)$ space), e.g., Quantified Boolean Formula (QBF), some logic games, space-bounded automata, etc [51].

7. **NPSPACE** (Nondeterministic Polynomial Space): Problems solvable in NTM using polynomial memory space $O(poly(N)$ space), and **NPSPACE**=**PSPACE** by Savitch's Theorem [52].

8. **EXPSPACE** (Exponential Space): Problems that can be solved in DTM using the exponential memory space $O(2^{poly(N)}$ space), with typical examples including generalized Tiling [53] and First-Order Logic with Transitive Closure [54].

9. **NEXPSPACE** (Nondeterministic Exponential Space): Problems that can be solved by NTM using the exponential memory space $O(2^{poly(N)}$ space), and as in the case of the **NPSPACE** class, **NEXPSPACE**=**EXPSPACE** by Savitch's Theorem [52].

Additionally, there is the Bounded-error Quantum Polynomial Time (**BQP**) class, which is a Quantum Turing machine (QTM, also known as Universal Quantum Computer [55]) version of **BPP**:

10. **BQP** (Bounded-error Quantum Polynomial Time): Problems that can be solved by a Quantum Turing machine (QTM) in polynomial time with an error probability of 1/3 or less, representative examples are Shor's Algorithm (Integer Factorng) and Grover's search algorithm [2, 46].

And these Complexity Classes show the containment relation in Eqs. (2.24), which can be represented by the diagram in Fig. 2.4:

$$\mathbf{P} \subseteq \mathbf{NP} \subseteq \mathbf{PSPACE} \subseteq \mathbf{EXPTIME} \subseteq \mathbf{NEXPTIME} \subseteq \mathbf{EXPSPACE} \tag{2.24a}$$

$$\mathbf{P} \subseteq \mathbf{BPP} \subseteq \mathbf{BQP} \subseteq \mathbf{PSPACE} \subseteq \mathbf{EXPTIME} \subseteq \mathbf{NEXPTIME} \subseteq \mathbf{EXPSPACE} \tag{2.24b}$$
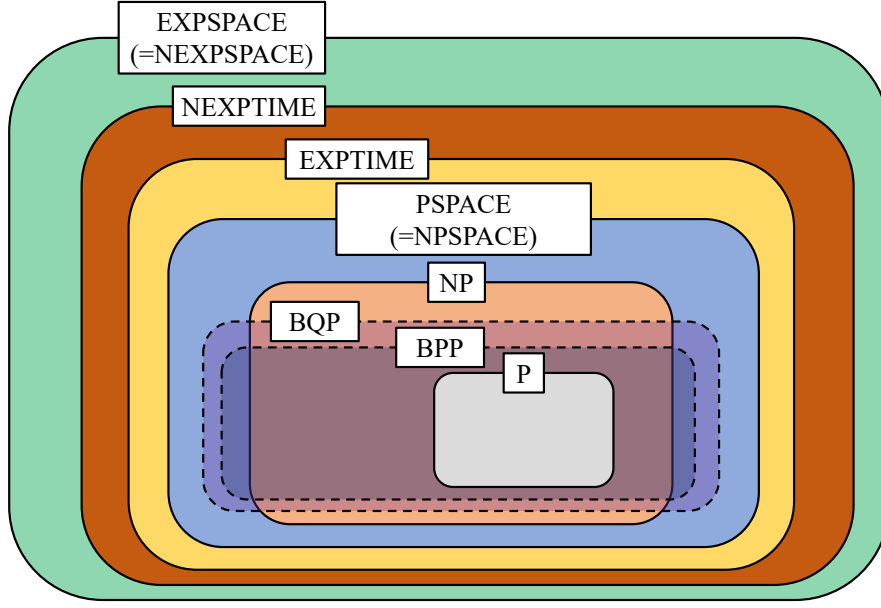
Figure 2.4: Containment relation among computational complexity classes

In addition, the class of computational problems whose difficulty is **NP**-class or higher is called the **NP-Hard** Class, and the formal definition is as follows:

NP-Hard: A problem A is **NP-Hard** if A is reducible from L to A in polynomial time for all **NP** problems L (i.e., $\forall L \in \mathbf{NP}, L \leq_P A \Rightarrow A \in \mathbf{NP\text{-}Hard}$)

Notable examples of NP-hard problems are the SAT and the Halting Problem (which is **NP-hard** but **not** in the **NP** class). The class of **NP** problems that are **NP-hard** is called as **NP-complete** problems, which are the hardest problems in NP. We will deal with one of these NP-complete problems, in particular the maximum independent set (MIS) problem, which is a classic graph theory problem in the field of combinatorial optimization.

2.2.1 Definition and Computational Complexity of the MIS Problem

Given an undirected graph $G = (V, E)$ defined by a set of nodes V and a set of edges $E(\subseteq V \times V)$ that are the connections between these nodes, an independent set is a subset $S(\subseteq V)$ of nodes such that no two nodes are neighboring by an edge (i.e. $\forall u, v \in S, (u, v) \notin E$, namely "independence condition") [56]. The maximum independent set (MIS) problem, as shown in Fig. 2.5, is the problem of finding the largest possible size of such an independent set in a given graph, and is formally defined as follows:

MIS Problem: Finding $S^* \subseteq V$ such that S^* is an independent set and $|S^*|$ is maximized.

Exact Maximum Independent Set (size = 5): [1, 3, 7, 8, 10]
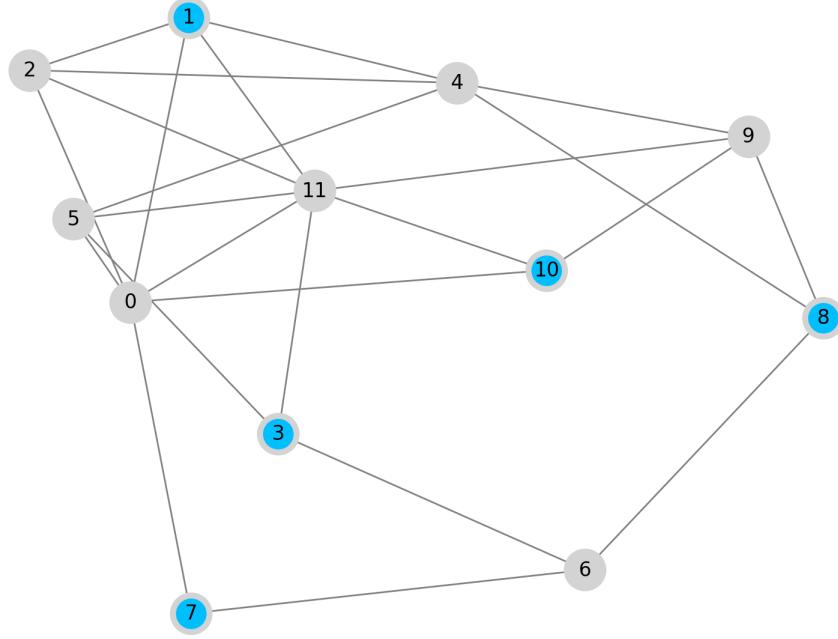
Figure 2.5: Maximum independent set (MIS) of a connected graph with 12 nodes, The blue-highlightened nodes are elements of an exact MIS $\{1, 3, 7, 8, 10\}$.

Computational Complexity

The MIS problem is **NP-hard** and also belongs to the **NP-complete** class, i.e., there is no known polynomial-time solving algorithm for an arbitrary graph $G(V, E)$ unless $\mathbf{P} = \mathbf{NP}$ [49]. The time complexity of the best exact algorithm [57], which uses a modified recursive algorithm, is $O(2^{0.276|V|})$, and on the approximability aspect, for any given graph $G(V, E)$ (whose exact MIS size is $|\mathrm{MIS}|$), there exists a polynomial-time approximation algorithm such that for all $\varepsilon > 0$, the solution S' is approximated by $|S'|/|\mathrm{MIS}| \leq |V|^{\varepsilon-1}$ (i.e., which is in the Poly-APX class) [58, 59, 60]. In other words, the MIS problem for arbitrary graphs is extremely hard to even approximate in polynomial time [58].

2.2.2 Applications and Advances in Classical Computing of MIS Problem

As mentioned in the definition of the MIS problem in Subsection 2.2.1, the MIS problem is the problem of finding the largest independent set, which is a set of non-adjacent points. Despite its NP-completeness, it has many practical applications in real-world systems where non-interference or conflict avoidance is critical, across computer science, engineering, and natural sciences. Due to this importance of MIS problem, there is a lot of research on advanced algorithms and methods to solve MIS problem. Therefore, in this subsection, we will introduce the applications of MIS problem in practical fields and the advances in classical computing.

Practical applications of MIS problem

Based on the non-adjacency of independent sets and the feature that MIS is the maximization version of independent set size, several applications have been proposed in practical fields such as network theory, circuit design, computer science, data analysis, etc. Examples include:

1. **Non-interfering Wireless Networking**: In wireless ad hoc or sensor networks, the points that can communicate simultaneously without interference are an independent set, of which MIS corresponds to optimal communication channel reuse [61].

2. **Task Scheduling in Parallel Computing**: In task scheduling, the optimization of parallelism in which tasks do not conflict due to shared resources or data dependence between tasks is a MIS problem [62].

3. **Optimal Design of VLSI and Circuit Layout**: An optimal integrated circuit with no shorts between adjacent elements is an MIS [63].

4. **Social Netwrok Analysis**: The complement of MIS is minimum vertex cover, which is the set of the smallest number of nodes that are crucial for understanding the structure of the network and for monitoring and controlling information propagation [64].

Classical Algorithms

There are multiple classical algorithms - Exact or Approximation and Heuristic Algorithms - to solve the **MIS** problem:

1. **Exact Algorithms**

   (a) **Brute Force (Exhaustive Search)** [49]: Algorithm which checks thes independence of all $2^{|V|}$ subsets. Its time complexity is $O(2^{|V|})$.

   (b) **Backtracking with Pruning** [65]: Algorithm which explores solution space via recursive method and prunes branches where independent set conditions fail or cannot improve current best.

   (c) **Robson's Algorithm** [57]: Fastest known exact algorithm which use an advanced recursive backtracking with clever branching and memoization. Its time complexity is $O(2^{0.276|V|})$.

2. **Approximation and Heuristic Algorithms**

   (a) **Greedy Algorithms** [66]: An algorithm which repeats choosing a vertex of the lowest degree, adding it to set, and removing it and its neighbors.

   (b) **Local Search** [67]: It starts with a candidate independent set and tries to swap in better vertices. But it may get stuck in local optima.

   (c) **Simulated Annealing** [67, 68]: Stochastic local search technique that avoids local minima by occasionally accepting worse solutions.

2.2.3 Rydberg atom system: An Intrinsic Quantum Machine for MIS problem

In Sec. 2.1, we mentioned the high quantum controllability provided by laser pulses through strong ground-Rydberg coupling of two-photon transitions and strong long-range Rydberg-Rydberg interaction as features of the Rydberg atom system. Then, in Subsecs. 2.2.1 and 2.2.2, we introduced the maximum independent set (MIS) Problem, which is a representative example of the most difficult NP-complete problem in terms of computational complexity. In this subsection, it will be explained why the Rydberg atom system is an intrinsic quantum machine for solving the MIS problem.

Rydberg Hamiltonian: Natural Encoder of the MIS cost Hamiltonian

By the definition of the MIS Problem in Subsec. 2.2.1, the cost Hamiltonian $H_{\mathrm{MIS}}(G)$ of the MIS Problem for a given graph $G(V, E)$ is given by:

$$H_{\mathrm{MIS}}(G) = \sum_{j \in V} (-\Delta n_j) + \sum_{(j,k) \in E} U n_j n_k, \tag{2.25}$$

where $n_j = 0, 1$ is an occupation number, a binary variable indicating whether node $j \in V$ is included in the independent set S^* or not, where $n_j = 1$ means that it is included in S^*. Δ and U are positive constants with the relation $0 < \Delta < U$, which act as the promoting term $-\Delta n_j$ that maximizes the size of the independent set and the constraint term $U n_j n_k$ by the definition of the independent set, respectively [68, 69].

Comparing this to the quantum Hamiltonian $\hat{H}_{\mathrm{Ryd}}$ of a Rydberg atom system (Eq. (2.14) with $U_{j,k} \equiv C_6/r_{jk}^6$), the Rydberg-Rydberg interaction term $U_{j,k}$ between the j-th and k-th atoms corresponds to the constraint term $U n_j n_k$ in the Eq. (2.25).

$$\hat{H}_{\mathrm{Ryd}} = \hbar \left[\sum_j \left(\frac{\Omega}{2} \hat{\sigma}_j^x - \Delta \hat{n}_j \right) + \sum_{j<k} U_{j,k} \hat{n}_j \hat{n}_k \right]. \tag{2.26}$$

Furthermore, by the Rydberg blockade described in Subsection 2.1.2, nodes within the Rydberg blockade distance $d_B = (C_6/\Omega)^{1/6}$ can only be excited by one node. Then, let j and k be two nodes j and k neighboring by an edge $(j,k) \in E$, and let them be j-th atom and k-th atom whose distance is within d_B (i.e., $r_{jk} < d_B$), then the Rydberg blockaded states of this Rydberg atom system are all independent sets [69]. Moreover, the ground states among these states correspond to MIS and these ground states can be obtained by adiabatic quantum evolution by proper tuning of Ω and Δ [68, 70]. Thus, it can be seen that the Rydberg Hamiltonian $\hat{H}_{\mathrm{Ryd}}$ (Eq. (2.26)) maps efficiently to the cost Hamiltonian H_{MIS} (Eq. (5.2)) of the MIS problem.

Reprogrammable graph embedding

By using the property called Rydberg blockade introduced in Subsec. 2.1.2, any given graph $G(V, E)$ can be programmed as a Rydberg atom array for an arbitrary MIS problem by corresponding nodes and edges to two atoms that are within d_B of each other [71].
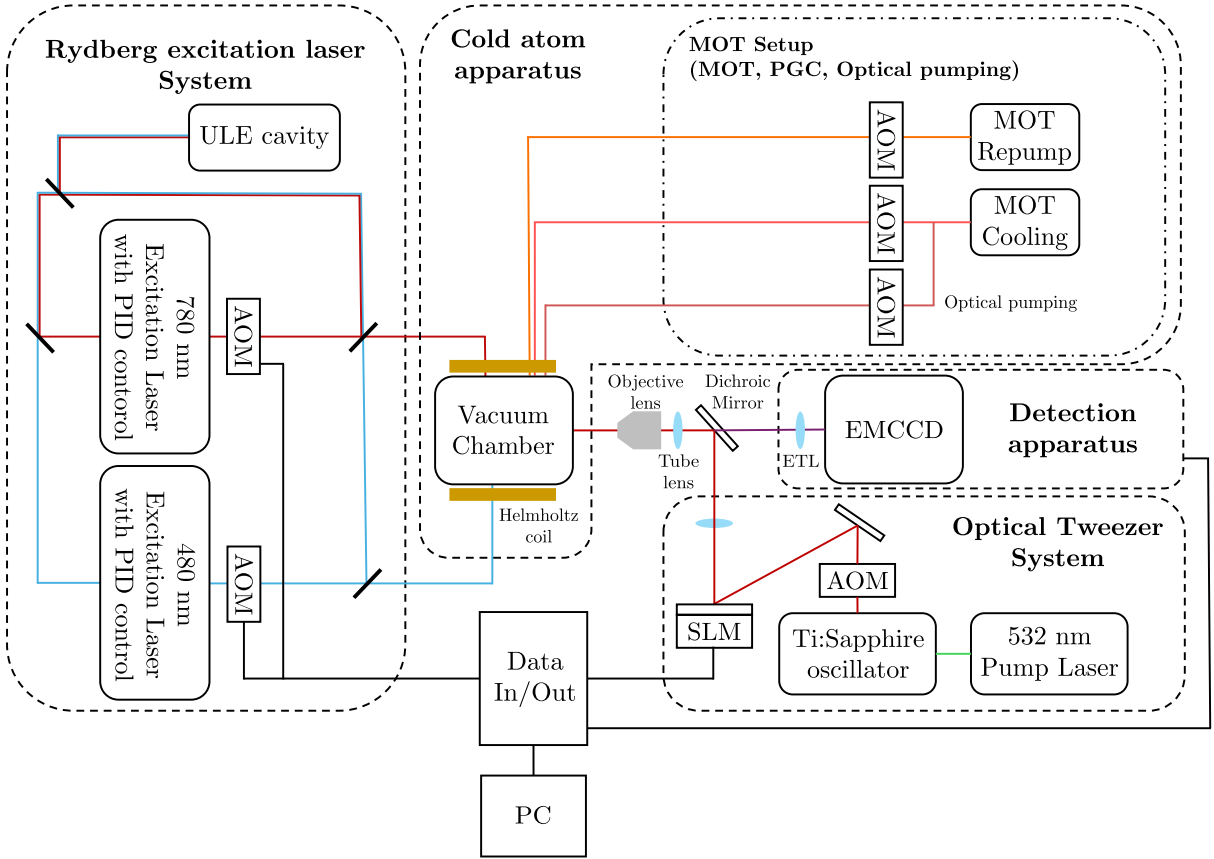
Figure 2.6: Schematic diagram of the experimental setup, The experimental setup consists of total four main parts: (1) Cold atom apparatus (MOT setup with a vacuum chamber), (2) Optical tweezer system, (3) Rydberg excitation laser system, (4) Detection apparatus.

Therefore, Rydberg atom array is an **intrinsic quantum computational tool** that can realize the edge connectivity of a given MIS problem graph with a property called **Rydberg blockade**.

2.3 Experimental setup for Rydberg atom Quantum Programming

In the previous sections 2.1 and 2.2, we introduced Rydberg atom array, one of the physical implementation systems of quantum programming, and the MIS problems that can be solved intrinsically by this Rydberg atom system. In this section, we will introduce the atomic qubit experimental setup, which is the hardware of quantum computing using Rydberg atom system. First, we will describe the preparation process of Rydberg atom array and initial state required for the physical implementation of quantum programming, and introduce the atomic transition between ground and Rydberg states used for the operation of quantum computing in Rydberg atom system. Finally, we will explain the setup and methods for measuring the results of quantum computing operations.

The experimental setup for the Rydberg atom quantum machine, as shown in Fig. 2.6, consists of

a cold atom apparatus, an optical tweezer system, a Rydberg excitation laser system, and a detection apparatus [19, 72, 73]. The cold atom apparatus and optical tweezer system are used in the preparation of the Rydberg atom array and initial state (Subsec. 2.3.1), The Rydberg excitation laser system is used in the process of atomic transition between ground and Rydberg states (Subsec. 2.3.2), and the detection apparatus is used to measure the operation results of quantum computing (Subsec. 2.3.3).

2.3.1 Preparation of the Rydberg atom array

As mentioned in Section 2.1 and Subsection 2.2.3, quantum programming using Rydberg atom system is based on an atom array with connectivity through a property called Rydberg blockade between atomic qubits at designated positions. Therefore, we would like to introduce the process of preparing atomic qubits required for quantum programming using Rydberg atom system at first. The process of preparing atomic qubit consists of the following four parts:

1. Cold atom loading via magneto optical trap (MOT) and polarization gradient cooling (PGC) [74],

2. Single atom trapping via the far-off-resonance optical trap (FORT) [75] of an optical tweezer beam,

3. Atom rearrangement [76, 77] to create a defect-free Rydberg atom array,

4. Initial state preparation via optical pumping.

Magneto optical trap and Polarization gradient cooling

To make a Rydberg atom array, cold atoms are necessary, and the setup for this, the cold atom apparatus, is a magneto-optical trap (MOT). As shown in Figure 2.6, the MOT setup consists of a vacuum chamber (2.6×10^{-10} Torr) containing atoms (rubidium, ^{87}Rb), cooling and repump lasers used for Doppler cooling and polarization gradient cooling (PGC) [74], and an anti-Helmholtz (AH) Coil (Figure 2.7 (a)), which generates an atom cloud at a specific location by Zeeman shift due to a position-dependent magnetic field $B_z (\propto z)$ with zero magnitude at the center of coil. The roles of the AH-coil, Cooling and Repump laser used in such a MOT setup are as follows:

1. *Cooling laser* : As shown in Fig. 2.8 (a), for the $\left|5P_{3/2}, F' = 3\right\rangle$ state, which is detuned (red-detuned) by -2.5Γ ($\Gamma = 2\pi \times 6$ MHz) with a σ^+-polarized laser in the 780-nm wavelength band that was detuned (red-detuned) by $\Gamma = 2\pi \times 6$ MHz, and the cyclic transition it induced $\left|5S_{1/2}, F = 2\right\rangle \leftrightarrow \left|5P_{3/2}, F' = 3\right\rangle$, which leads to Doppler cooling of the atom with a dissipative optical force $\vec{F}_{\text{MOT}}$ ($\propto -\vec{v}$) (depicted in Fig. 2.7 (b)) proportional to the velocity $\vec{v}$ of the atom [39]. After Doppler cooling, it is used to perform sub-Doppler cooling, PGC, by changing its detuning.

2. *Repump laser* : A σ^+-polarized laser with a wavelength of 780-nm to compensate the state leakage due to the spontaneous decay $\left|5P_{3/2}, F' = 2\right\rangle \rightarrow \left|5S_{1/2}, F = 1\right\rangle$ during the cyclic transition of a cooling laser, and to recover the leaked state in the transition $\left|5S_{1/2}, F = 1\right\rangle \rightarrow \left|5P_{3/2}, F' = 2\right\rangle \rightarrow \left|5S_{1/2}, F = 2\right\rangle$.

(a)
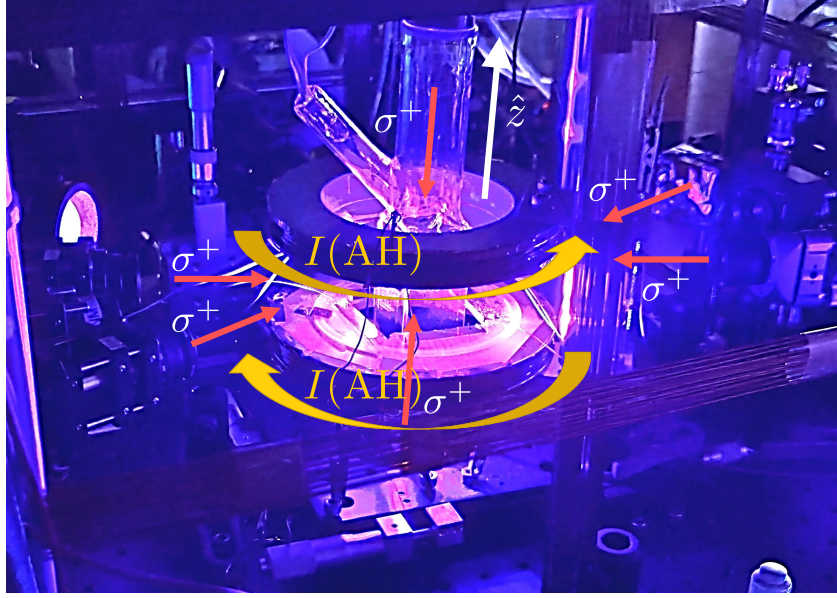
(b)
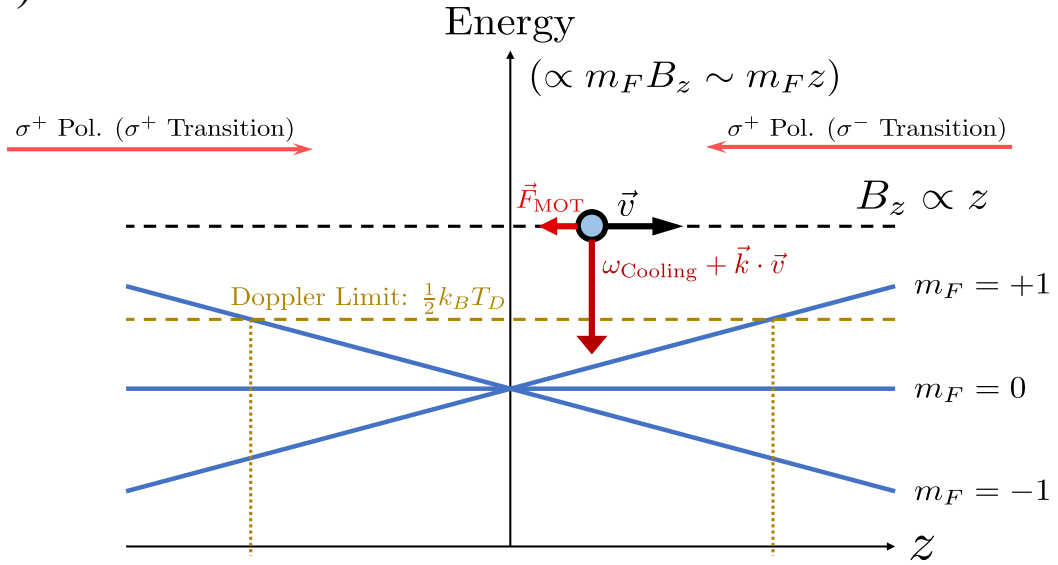
Figure 2.7: Principle of the magneto-optical trap (MOT), (a) MOT setup including anti-Helmholtz (AH) coil in KAIST ALICE-II, (b) Atom's energy-position (E-z) diagram for MOT cooling, The MOT Cooling laser (with the doppler-shifted frequency $\omega_{\text{Cooling}} + \vec{k} \cdot \vec{v}$) acts as a dissipative force $\vec{F}_{\text{MOT}}$ ($\propto -\vec{v}$) to an atom. By applying a position-dependent magnetic field $B_z (\propto z)$ by an AH-coil, the shift of energies of the Zeeman sublevels (blue solid lines) is linear to z.

3. *AH-coil* : As depicted in Fig. 2.7 (b), The Zeeman sublevel shift, which varies linearly with the component of the AH-coil center axis ($\hat{z}$ direction) at each atom position, serves to trap the atoms cooled to the Doppler limit $k_B T_D/2$ ($T_D = \hbar\Gamma/2k_B = 146$ μK for the ^{87}Rb D_2 line, gold-colored dashed line in Fig. 2.7 (b)) within a certain z range (within the gold-colored dashed lines in Fig. 2.7).

$nS_{1/2}$ ——————— $J = 1/2$

(b)

$m_J = 1/2$ — $\Delta_{m1} + \Delta_{m2}$

Rydberg excitation
(480 nm, σ^- Pol.)

$5P_{3/2}$ D_2 Line

$F' = 3$ -2.5Γ
$F' = 2$
$F' = 1$
$F' = 0$

$m_F = +3$ $\Delta_{m1} = 2\pi \times 660$ MHz

$m_F = -3$ $m_F = +2$

$m_F = -2$

Rydberg excitation
(780 nm, σ^+ Pol.)

$5P_{1/2}$ D_1 Line
Cooling

Repump

Optical tweezer

Optical pumping

$5S_{1/2}$

$F = 2$

$F = 1$

Optical
pumping
(σ^+ Pol.)

$m_F = -2$

$m_F = +2$

Maximized Spontaneous decay
(Unless optical pumping is done)

$5P_{3/2}$ $F' = 2$
or
$F' = 3$

$5S_{1/2}$ $F = 2$
$m_F =$ -2 -1 0 $+1$ $+2$
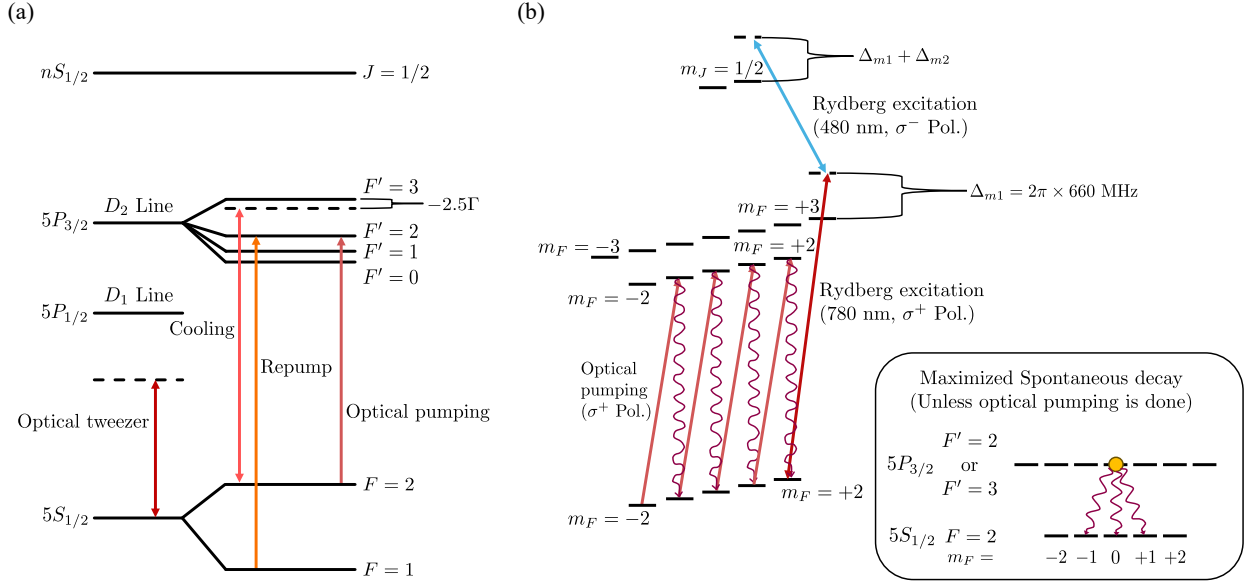
Figure 2.8: Energy level diagram of ^{87}Rb for (a) MOT and optical tweezer, and (b) Optical pumping and Rydberg Excitation, the inset in (b) represents the situation where the spontaneous decay of the intermediate state is maximized without the optical pumping.

After Doppler cooling, the AH-coil is turned off in the PGC process.

After this Doppler cooling and PGC, a cold atom source with a temperature around $T = 25$ μK is loaded.

Single atom trapping and rearrangement

Once the source of cold atoms is loaded by the MOT setup, by using an optical tweezer system, each single atom is positioned at the targetted coordinates according to Rydberg atom array construction. As shown in the Fig. 2.6, the optical tweezer system consists of a spatial light modulator (SLM, Meadowlarks ODPDM512), a π-polarized off-resonant 820 nm laser (a Ti:sapphire CW laser from Avesta), an objective lens (Mitutoyo G Plan Apo 50X with a high-numerical aperture NA = 0.5), and a 532 nm pump laser (Verdi G-18 from Coherent). And how the optical tweezer system works is as follows:

1. *Single atom trapping*: The position coordinate information of the atom array is converted into the holographic phase of the SLM via the Gerchberg-Saxton weighted (GSW) Algorithm [76, 78, 79]. A π-polarized off-resonant 820-nm laser with a phase changed by SLM is focused by an objective lens at the targeted coordinates on the MOT Cloud with a beam diameter $2w_0 \sim 2\mu$m (w_0: beam waist) [19] to create a tightly focused far-off-resonance optical trap (FORT) [75] (Fig. 2.9 (a)). Here, FORT [75] is a dipole trap using the AC Stark Shift (Eq. (2.8b)) mentioned in Subsec. 2.1.1, where only the term corresponding to the red-detuned laser beam L1 is used (i.e., the term corresponding to the laser beam L2 is zero). And derived from this, the trap depth U_0 of

(a)   (b)
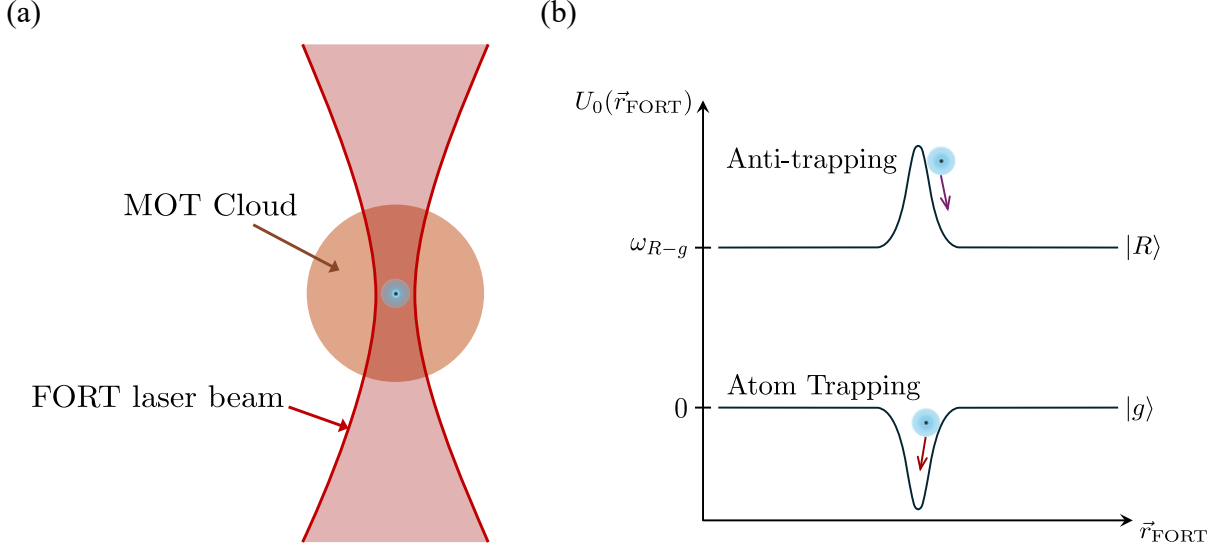
Figure 2.9: Principle of an optical tweezer, (a) Single atom trapping by the optical tweezer through a far-off-resonance optical trap (FORT) laser beam, (b) The action of the optical tweezer as the atom trapping for the ground state $|g\rangle$ and the anti-trapping for Rydberg state $|R\rangle$, respectively.

FORT is as follows:

$$U_0 = \frac{\hbar\Omega_{\mathrm{FORT}}^2}{4\Delta_{\mathrm{FORT}}} \tag{2.27a}$$

$$= \frac{3\pi c^2 \Gamma}{2\hbar\omega_0^3} \cdot \frac{I(\vec{r}_{\mathrm{FORT}})}{\Delta_{\mathrm{FORT}}}, \tag{2.27b}$$

where $\omega_{\mathrm{FORT}} = 2\pi/(\lambda_{\mathrm{FORT}})$ ($\lambda_{\mathrm{FORT}} = 820$ nm) is the angular frequency of the FORT laser beam, $I(\vec{r}_{\mathrm{FORT}})$ is the Gaussian beam intensity of the FORT laser at relative position $\vec{r}_{\mathrm{FORT}}$ from the center of the FORT (which makes the FORT as a Gaussian trap), and $1/\Delta_{\mathrm{FORT}}$ ($= 1/(3\Delta_{\mathrm{FORT,D_1}}) + 2/(3\Delta_{\mathrm{FORT,D_2}})$) is the reciprocal of the harmonic mean of detunings $\Delta_{\mathrm{FORT,D_1}}$ and $\Delta_{\mathrm{FORT,D_2}}$ for the $\mathrm{D_1}$ and $\mathrm{D_2}$ lines according to Clebsch-Gordan coefficient [40].

2. *Atom Rearrangement*: After trapping a single atom, the process to check whether a single atom is trapped in the FORT at each targeted coordinate, and move the trap of the single atom prepared previously in the nearby area via SLM to the FORT where the atom is not trapped and refill it [76, 77].

With these two processes, *Single atom trapping* and *Atom Rearrangement*, we generate the targeted atom array.

Initial state preparation

Once the atom array is prepared for the targeted configuration by the optical tweezer system, an initial state preparation is required to accumulate the distribution of ground hyperfine states of each single atom toward $|g\rangle = |5S_{1/2}, F = 2, m_F = 2\rangle$ through optical pumping in order to minimize the dephasing due to the maximization of the spontaneous decay effect from the divergent ground hyperfine

state population. The optical pumping beam used for optical pumping is from the MOT setup and is as follows:

1. Detuned Cooling laser beam: σ^+-polarized beam for the cyclic transition (Fig. 2.8 (b)) $\left|5S_{1/2}, F = 2\right\rangle \leftrightarrow \left|5P_{3/2}, F' = 2\right\rangle$

2. Repump laser beam: σ^+-polarized beam for the transition $\left|5S_{1/2}, F = 1\right\rangle \to \left|5P_{3/2}, F' = 2\right\rangle \to \left|5S_{1/2}, F = 2\right\rangle$

2.3.2 Rydberg excitation

In Subsection 2.3.1, we introduced how to prepare a Rydberg atom array consisting of atoms in the initial state for quantum operation and the experimental setup required for this preparation, which is a cold atom apparatus and an optical tweezer system. Once the atomic qubit structure is prepared in the Rydberg atom array configuration, we proceed to the quantum operation of this atomic qubit structure. The experimental setup that physically implements the quantum operation of the qubit structure consisting of such a Rydberg atom array is the Rydberg excitation laser system for the two-photon transition between the ground-state $|g\rangle = \left|5S_{1/2}, F = 2, m_F = 2\right\rangle$ and the Rydberg state $|R\rangle = \left|nS_{1/2}, F'' = 2, m''_F = 2\right\rangle$ ($\approx \left|nS_{1/2}, m_J = 1/2\right\rangle \otimes |I = 3/2, m_I = 3/2\rangle$ for $n \gtrsim 30$ [15, 36, 41]) (in Fig. 2.8 (b) and Subsec. 2.1.1).

As shown in Fig. 2.6, the Rydberg excitation laser system consists of a 780 nm (a homemade external-cavity diode laser) laser at the one-photon-transition between the ground state $|g\rangle = \left|5S_{1/2}, F = 2, m_F = 2\right\rangle$ and the near-resonant intermediate state $|i\rangle = \left|5P_{3/2}, F' = 3, m'_F = 3\right\rangle$ and a 480 nm (Toptica TA-SHG Pro) laser at the approximate one-photon transition between $|i\rangle = \left|5P_{3/2}, F' = 3, m'_F = 3\right\rangle$ and the Rydberg state $|R\rangle = \left|71S_{1/2}, m_J = 1/2\right\rangle$, whose laser frequencies are stabilized down to a narrow linewidth of < 30 (2π) kHz by a proportional-integral-derivative (PID) controller (Toptica FALC 110) and an ultra-low expansion (ULE) cavity (Stable laser systems, finesse 15,000). As described in Fig. 2.8 (b), the 780 nm laser has a circular polarization of σ^+, with intermediate detuning on the scale of $\Delta_{m1} \approx 2\pi \times 660$ MHz [72], and the 480 nm laser has a circular polarization of σ^-. And two control parameters Ω and Δ in Eq. (2.9) are modulated with a radio-frequency synthesizer (Moglabs XRF) and acousto-optic modulators (AOMs) [80, 81]

This Rydberg excitation laser system is responsible for controlling the Rydberg atom system to perform the quantum operation by tuning $\hat{H}_{g-R}$ (Eq. (2.9)) mentioned in Subsec. 2.1.1.

2.3.3 Atomic qubit state measurement

After the quantum operation via the Rydberg excitation setup introduced in Subsection 2.3.2, the detection of whether the atomic qubit state resulting from the quantum operation is ground or Rydberg state is conducted. As shown in the Fig. 2.6, the detection apparatus is the setup used here consisting of an electron-multiplying charge-coupled device (EMCCD, Andor iXon Ultra 897) and an electrically tunable lens (ETL, EL-16-40-TC of Optotune).

Atomic qubit state measurement process consists of Rydberg state repulsion measurement and imaging detection of trapped ground-state atom:

1. *Rydberg state repulsion measurement*: The trap depth U_0 (Eq. (2.27a)) of the FORT as explained in Subsec. 2.9, acts as a trap for the ground state $|g\rangle$ and an anti-trapping [82] to repel the Rydberg

state $|R\rangle$, as described in Fig. 2.9 (b). Based on this, the optical tweezer beam is turned on at each FORT position again to recapture only a single ground-state atom at each position into the trap.

2. Imaging detection of trapped ground-state atom : After Rydberg state repulsion, the fluorescence due to the $|5S_{1/2}, F = 2\rangle$-$|5P_{3/2}, F = 3\rangle$ transition of the ground-state single atoms remaining in the trap is observed with ETL and EMCCD by using a cooling laser beam with changed detuning as the imaging beam to generate fluorescence imaging data.

From the generated fluorescence imaging data, the retrapped single-atoms with high fluorescence intensity are detected as ground-state $|g\rangle$ and empty traps with no fluorescence intensity are detected as Rydberg state $|R\rangle$.

Chapter 3. Rydberg Wire Gates Design for Universal Quantum Computation

In this chapter, we present an all-optical quantum gate scheme in a Rydberg atom array where no ground sub-levels are resorted to, but instead auxiliary atoms (wire atoms) mediating the coupling between qubit atoms (data atoms) and single-atom addressing operations are used. This scheme uses a Rydberg atom array as a cluster of data and wire qubits, which uses the Rydberg and ground states as the two qubit states of a data qubit and the wire atoms between data qubits mediate the interactions between data atoms via a sequence of single-atom addressing operations. The advantage of this setup is that the implementation of all gates is fast laser excitation of the ground-Rydberg transitions, which enables the quantum circuit for a certain computational task (including digital quantum simulation) to be carried out fast.

This chapter is based on a published paper: S. Jeong, X-F. Shi, M. Kim and J. Ahn "Rydberg Wire Gates for Universal Quantum Computation," Front. Phys. **10**, 875673 (2022) [83].

3.1 Single-Atom Addressing in a Rydberg-Atom System

We aim to design a quantum gate as a sequence of individual-atom addressing in a Rydberg atom array, so we consider a two-dimensional (2D) array of atoms, as shown in Figure 3.1 (a). Since in the Rydberg blockade regime, two adjacent atoms are inhibited from being excited to an anti-blockade state, $|11\rangle$, the computational space of the two atoms is limited to $\{|00\rangle, |01\rangle, |10\rangle\}$ excluding $|11\rangle$ (the anti-blockade two-atom state) upon defining the two-level system $\{|0\rangle, |1\rangle\}$ of each atom's ground state and Rydberg state. However, general quantum computation requires $|11\rangle$, so we use auxiliary atoms (referred to hereafter as wire atoms) to mediate the coupling between data atoms. In Fig. 3.1 (a), the data atoms are represented by red spheres and the wire atoms by gray spheres.

The three-atom system AWB in Fig. 3.1 (a) consists of data atoms A and B, and a wire atom W that couples A and B. The wire atom is excited to $|1\rangle$ only for data processing of $|AB\rangle$, otherwise it is left as $|0\rangle_W$. Based on that, there are five computational ground states: $|00\rangle_{AB} |0\rangle_W$, $|01\rangle_{AB} |0\rangle_W$, $|10\rangle_{AB} |0\rangle_W$, $|11\rangle_{AB} |0\rangle_W$, and $|00\rangle_{AB} |1\rangle_W$. The first four base states are the computational basis for the two data (AB) system, and the last one, $|00\rangle_{AB} |1\rangle_W$, can be considered a temporal register, as in Fig. 3.1 (b). There are three available atom addressings by three-qubit gate operations:

$$\tilde{W}(\Theta, \phi) = e^{-\frac{i}{\hbar} \int H_W dt}, \tag{3.1a}$$

$$\tilde{A}(\Theta, \phi) = e^{-\frac{i}{\hbar} \int \left(\frac{\hbar\Omega}{2} \hat{n}_\phi \cdot \vec{\sigma}^A + V n_W n_A \right) dt}, \tag{3.1b}$$

$$\tilde{B}(\Theta, \phi) = e^{-\frac{i}{\hbar} \int \left(\frac{\hbar\Omega}{2} \hat{n}_\phi \cdot \vec{\sigma}^B + V n_W n_B \right) dt}, \tag{3.1c}$$

where Θ and ϕ are the Rabi rotation angle and axis, respectively. The Hamiltonian H_W of a single addressing of W in the Rydberg blockade regime, i.e., $d < d_B < \sqrt{2}d$ (where d and d_B are the interatomic distance and blockade distance, respectively), of adjacent atoms is as follows:

$$H_W = \frac{\hbar\Omega}{2} \hat{n}_\phi \cdot \vec{\sigma}^W + V n_W \left(n_A + n_B \right), \tag{3.2}$$
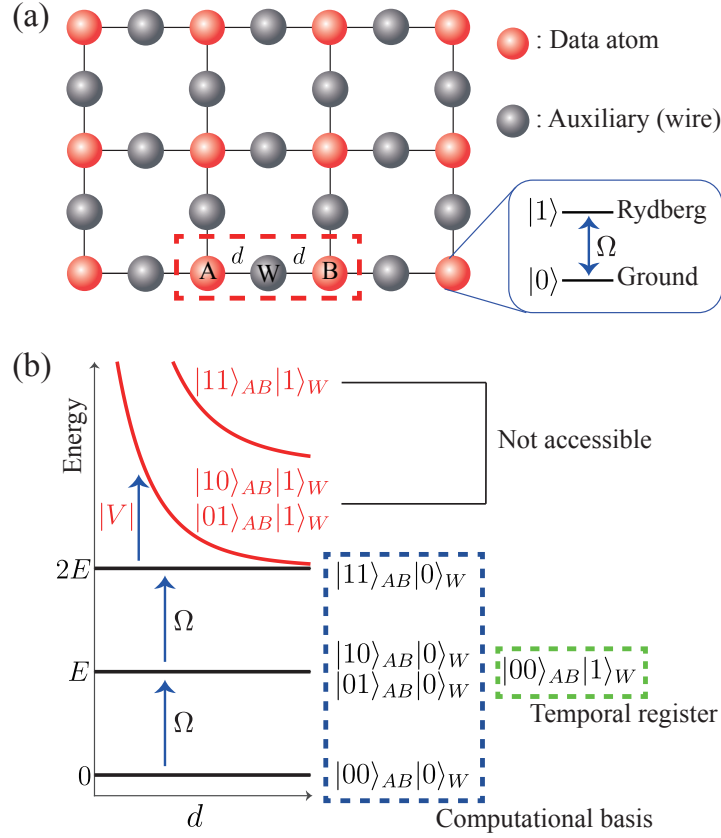
Figure 3.1: The Rydberg wire gate scheme: (a) A 2D atomic array is composed of data atoms (red spheres) and auxiliary (wire) atoms (gray spheres). A two-level system for each atom is used, with an atomic ground state $|0\rangle$ and a Rydberg state $|1\rangle$. Wire atoms, e.g., W, mediate the coupling between two neighboring data atoms, e.g., A and B, which are distant from W by a distance d. (b) The energy level diagram of the three atoms, A, W, and B. We use four computational basis states $|00\rangle_{AB}|0\rangle_W$, $|01\rangle_{AB}|0\rangle_W$, $|10\rangle_{AB}|0\rangle_W$, $|11\rangle_{AB}|0\rangle_W$ (in the blue dotted squares), and the temporal register, $|00\rangle_{AB}|1\rangle_W$ (in the light green dotted squares), in total five accessible states. The other states, $|10\rangle_{AB}|1\rangle_W$, $|01\rangle_{AB}|1\rangle_W$, and $|11\rangle_{AB}|1\rangle_W$, are inaccessible due to the Rydberg blockade. The figure is reused from the reference [83], Frontiers Media S.A..

where Ω is the Rabi frequency, $\hat{n}_\phi$ is the rotational axis defined by a laser phase ϕ, $V = C_6/d^6$ is the van der Waals interaction with coefficient C_6, and $\vec{\sigma} = (\sigma_x, \sigma_y, \sigma_z)$ is the Pauli vector and $n = (1 - \sigma_z)/2$ is the excitation number.

We use them for general quantum computations on data AB atoms: $\tilde{W}$ transforms $|00\rangle_{AB}|0\rangle_W$ into $|00\rangle_{AB}|1\rangle_W$, preserving all other states and their superpositions. Hence, the $\tilde{W}$ operation is the inverted controlled rotation gate, where AB are the control qubits and W is the target qubit. The other three operations are reduced to single-atom and two-atom rotation on the data qubit (AB), given by Eqs. (3.3):

$$\mathbf{R}_A \otimes \mathbf{I}_B = \langle 0|_W \tilde{A} |0\rangle_W , \tag{3.3a}$$

$$\mathbf{I}_A \otimes \mathbf{R}_B = \langle 0|_W \tilde{B} |0\rangle_W , \tag{3.3b}$$

$$\mathbf{R}_A \otimes \mathbf{R}_B = \langle 0|_W \tilde{A}\tilde{B} |0\rangle_W , \tag{3.3c}$$

where **R** is the single-qubit rotation and **I** is the identity.

3.2 Design of Single- and Multi-Qubit Gates

3.2.1 Standard One-Qubit Gates

In this subsection, we design standard one-qubit gates which include Pauli gates **X**, **Y**, **Z**, general rotation $\mathbf{R}(\Theta, \phi)$, Hadamard gate **H**, and phase gate **P** via the atom-addressing operations $\tilde{W}$, $\tilde{A}$, and $\tilde{B}$ (Eqs. (3.1)).

The Pauli gates rotate the quantum state of one atom with the others remaining unchanged. For data atoms A and B, Pauli **X**-, **Y**-, and **Z**-gates are as follows:

$$\mathbf{X}_A \otimes \mathbf{I}_B \ = \ e^{i\alpha} \langle 0|_W \tilde{X}_A |0\rangle_W \,, \tag{3.4a}$$

$$\mathbf{I}_A \otimes \mathbf{X}_B \ = \ e^{i\alpha} \langle 0|_W \tilde{X}_B |0\rangle_W \,, \tag{3.4b}$$

$$\mathbf{Y}_A \otimes \mathbf{I}_B \ = \ e^{i\alpha} \langle 0|_W \tilde{Y}_A |0\rangle_W \,, \tag{3.4c}$$

$$\mathbf{I}_A \otimes \mathbf{Y}_B \ = \ e^{i\alpha} \langle 0|_W \tilde{Y}_B |0\rangle_W \,, \tag{3.4d}$$

$$\mathbf{Z}_A \otimes \mathbf{I}_B \ = \ e^{i\alpha} \langle 0|_W \tilde{X}_A \tilde{Y}_A |0\rangle_W \,, \tag{3.4e}$$

$$\mathbf{I}_A \otimes \mathbf{Z}_B \ = \ e^{i\alpha} \langle 0|_W \tilde{X}_B \tilde{Y}_B |0\rangle_W \,, \tag{3.4f}$$

where $\tilde{X}_A = \tilde{A}(\pi, 0)$, $\tilde{X}_B = \tilde{B}(\pi, 0)$, $\tilde{Y}_A = \tilde{A}(\pi, \pi/2)$ and $\tilde{Y}_B = \tilde{B}(\pi, \pi/2)$ and $\alpha = \pi/2$ is the global phase. The general rotations are given as follows:

$$\mathbf{R}_A(\Theta, \phi) \otimes \mathbf{I}_B \ = \ \langle 0|_W \tilde{A}(\Theta, \phi) |0\rangle_W \,, \tag{3.5a}$$

$$\mathbf{I}_A \otimes \mathbf{R}_B(\Theta, \phi) \ = \ \langle 0|_W \tilde{B}(\Theta, \phi) |0\rangle_W \,. \tag{3.5b}$$

The Hadamard gate **H** is a gate that maps the quantum states $|0\rangle$ and $|1\rangle$ to the superposition states $|+\rangle = (|0\rangle + |1\rangle)/\sqrt{2}$ or $|-\rangle = (|0\rangle - |1\rangle)/\sqrt{2}$, respectively, and it identical to $e^{i\pi/4}\mathbf{X}\sqrt{\mathbf{Y}}$, thereby resulting in

$$\mathbf{H}_A \otimes \mathbf{I}_B \ = \ e^{i\alpha} \langle 0|_W \tilde{X}_A \sqrt{\tilde{Y}_A} |0\rangle_W \,, \tag{3.6a}$$

$$\mathbf{I}_A \otimes \mathbf{H}_B \ = \ e^{i\alpha} \langle 0|_W \tilde{X}_B \sqrt{\tilde{Y}_B} |0\rangle_W \,, \tag{3.6b}$$

where $\sqrt{\tilde{Y}_A} = \tilde{A}(\pi/2, \pi/2)$ and $\sqrt{\tilde{Y}_B} = \tilde{B}(\pi/2, \pi/2)$ are the pseudo-Hadamard gates ($\alpha = \pi/2$).

The phase gates $\mathbf{P}_A(\phi)$ and $\mathbf{P}_B(\phi)$, are given by

$$\mathbf{P}_A(\phi) \otimes \mathbf{I}_B \ = \ e^{i\phi/2} \langle 0|_W \tilde{X}_A^\dagger \tilde{A}(\pi, \phi/2) |0\rangle_W \,, \tag{3.7a}$$

$$\mathbf{I}_A \otimes \mathbf{P}_B(\phi) \ = \ e^{i\phi/2} \langle 0|_W \tilde{X}_B^\dagger \tilde{B}(\pi, \phi/2) |0\rangle_W \,. \tag{3.7b}$$

S and **T** gates are obtained as $\mathbf{S}_A = \mathbf{P}_A(\pi/2)$, $\mathbf{S}_B = \mathbf{P}_B(\pi/2)$, $\mathbf{T}_A = \mathbf{P}_A(\pi/4)$, and $\mathbf{T}_B = \mathbf{P}_B(\pi/4)$. The global phase α of the aforementioned gates can be removed by using the global phase gate $\mathbf{Ph}(\alpha)$, defined as in Eq. (3.8):

$$\mathbf{Ph}(\alpha) = \langle 0|_W \tilde{Y}_B \tilde{X}_W^\dagger \tilde{W}(\pi, \alpha) \tilde{Y}_{AB}^\dagger \tilde{X}_W^\dagger \tilde{W}(\pi, \alpha) \tilde{Y}_B^\dagger \tilde{X}_W^\dagger \tilde{W}(\pi, \alpha) \tilde{Y}_{AB} \tilde{X}_W^\dagger \tilde{W}(\pi, \alpha) |0\rangle_W \,, \tag{3.8}$$

which is a combination of four two-qubit phase rotations, $|00\rangle \rightarrow e^{i\alpha} |00\rangle$ which is carried out by $\tilde{X}_W^\dagger \tilde{W}(\pi, \alpha)$, $|01\rangle \rightarrow e^{i\alpha} |01\rangle$ by $\tilde{Y}_B \tilde{X}_W^\dagger \tilde{W}(\pi, \alpha) \tilde{Y}_B^\dagger$, $|10\rangle \rightarrow e^{i\alpha} |10\rangle$ by $\tilde{Y}_A^\dagger \tilde{X}_W^\dagger \tilde{W}(\pi, \alpha) \tilde{Y}_A$, and $|11\rangle \rightarrow e^{i\alpha} |11\rangle$ by $\tilde{Y}_{AB}^\dagger \tilde{X}_W^\dagger \tilde{W}(\pi, \alpha) \tilde{Y}_{AB}$, where $\tilde{Y}_{AB} \equiv \tilde{Y}_A \tilde{Y}_B$.

(a) Controlled-NOT gate $\mathbf{CX}_{AB}$

(b) Controlled-Phase gate $\mathbf{CP}_{00}(\alpha)$
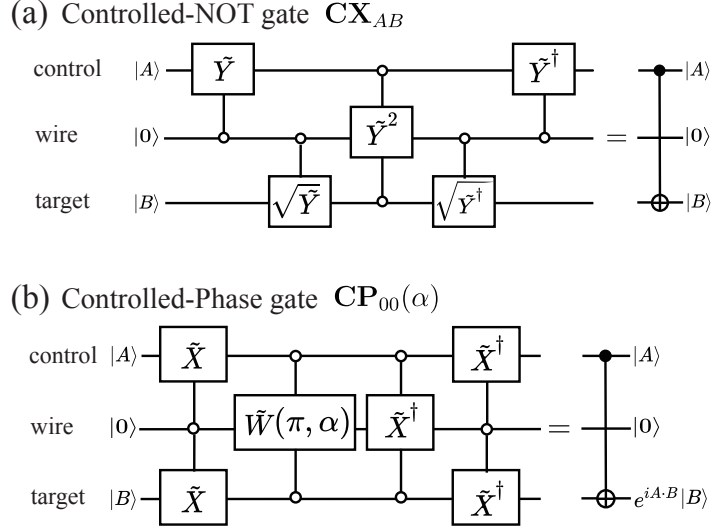
Figure 3.2: Quantum circuits of (a) controlled-NOT gate, $\mathbf{CX}_{AB}$, and (b) controlled-phase gate, $\mathbf{CP}_{00}(\alpha)$. The figure is reused from the reference [83], Frontiers Media S.A..

3.2.2 Standard Two-Qubit Gates

In this subsection, we focus on the standard two-qubit gates: the controlled-NOT gate $\mathbf{CNOT}$, the swap gate $\mathbf{SWAP}$, and the controlled-phase gate $\mathbf{CP}$.

The controlled-NOT gate, $\mathbf{CNOT}$, is a controlled X-gate, $\mathbf{CX}$, which flips the target qubit (the second qubit) only when the control qubit (the first qubit) is at $|1\rangle$ (i.e., $|AB\rangle \rightarrow |A, A \oplus B\rangle$). With atom addressing, $\mathbf{CX}_{AB}$ and $\mathbf{CX}_{BA}$ are given as follows, respectively:

$$\mathbf{CX}_{AB} = \langle 0|_W \tilde{Y}_A^\dagger \sqrt{\tilde{Y}_B^\dagger} \tilde{Y}_W^2 \sqrt{\tilde{Y}_B} \tilde{Y}_A |0\rangle_W \,, \tag{3.9a}$$

$$\mathbf{CX}_{BA} = \langle 0|_W \tilde{Y}_B^\dagger \sqrt{\tilde{Y}_A^\dagger} \tilde{Y}_W^2 \sqrt{\tilde{Y}_A} \tilde{Y}_B |0\rangle_W \,, \tag{3.9b}$$

The sequence of operation in $\mathbf{CX}_{AB}$ is as follows:

1. The central $\tilde{Y}_W^2$ acts as an inverted-$\mathbf{CZ}$-gate, flipping only the sign of the coefficients $|00\rangle_{AB} |0\rangle_W$.

2. Multiplying it by $\tilde{Y}_{AB}$ on one side and its Hermite conjugate on the other side, we obtain a controlled Z-gate (Eq. (3.10)), similar to that in Ref. [84].

3. Finally, by multiplying $\sqrt{Y_A}$ and its Hermite conjugate at both ends of Eq. (3.10), it yields $\mathbf{CX}_{AB}$.

$$\mathbf{CZ}_{AB} = \mathbf{CZ}_{BA} = \langle 0|_W \tilde{Y}_{AB}^\dagger \tilde{Y}_W^2 \tilde{Y}_{AB} |0\rangle_W \,, \tag{3.10}$$

The quantum circuit of $\mathbf{CX}_{AB}$ is shown in Fig. 3.2 (a). Similarly, the controlled Y-gates is obtained as follows:

$$\mathbf{CY}_{AB} = \langle 0|_W \tilde{Y}_A^\dagger \sqrt{\tilde{X}_B^\dagger} \tilde{Y}_W^2 \sqrt{\tilde{X}_B} \tilde{Y}_A |0\rangle_W \,, \tag{3.11a}$$

$$\mathbf{CY}_{BA} = \langle 0|_W \tilde{Y}_B^\dagger \sqrt{\tilde{X}_A^\dagger} \tilde{Y}_W^2 \sqrt{\tilde{X}_A} \tilde{Y}_B |0\rangle_W \,. \tag{3.11b}$$

$\mathbf{SWAP}$ gate is to perform state swapping of two qubits, i.e., $|AB\rangle \rightarrow |BA\rangle$, which is also to swap the coefficients of $|01\rangle$ and $|10\rangle$. In the atom-addressing scheme, the $\mathbf{X}$-gate version of the $\mathbf{SWAP}$ gate is given as follows:

$$\mathbf{SWAP} = \langle 0|_W \tilde{X}_A \tilde{X}_W \tilde{X}_{AB} \tilde{X}_W \tilde{X}_{AB}^\dagger \tilde{X}_W \tilde{X}_A^\dagger |0\rangle_W \,, \tag{3.12}$$

27

Eq. (3.12) is operated as follows:

1. The state interchange $|10\rangle_{AB}|0\rangle_W \leftrightarrow |00\rangle_{AB}|1\rangle_W$ occurs by the first three-pulse combination, $X_A^\dagger \tilde{X}_W \tilde{X}_A^\dagger$.

2. Then, the second combination $\tilde{X}_B \tilde{X}_W \tilde{X}_B^\dagger$ executes the state interchange $|00\rangle_{AB}|1\rangle_W \leftrightarrow |01\rangle_{AB}|0\rangle_W$.

3. Finally, the state interchange $|00\rangle_{AB}|1\rangle_W \leftrightarrow |10\rangle_{AB}|0\rangle_W$ by $\tilde{X}_A \tilde{X}_W \tilde{X}_A$ occurs.

Controlled-phase gate, $\mathbf{CP}(\alpha)$, sets the local phase of $|11\rangle$ of the AB data qubits. In our atom-addressing scheme, W-atom addressing $\tilde{W}(\pi, \alpha)$ turns $|00\rangle_{AB}|0\rangle_W$ into $-ie^{i\alpha}|00\rangle_{AB}|1\rangle_W$, and $\tilde{W}(\pi, \pi)\tilde{W}(\pi, \alpha)$ turns $|00\rangle_{AB}$ into $e^{i\alpha}|00\rangle_{AB}$, hence $\mathbf{CP}_{00}(\alpha)$ putting the local phase of $|00\rangle$ is to be given as follows:

$$\mathbf{CP}_{00}(\alpha) = \langle 0|_W \tilde{X}_W^\dagger \tilde{W}(\pi, \alpha)|0\rangle_W . \tag{3.13}$$

The quantum circuit for $\mathbf{CP}_{00}(\alpha)$ is shown in Fig. 3.2 (b). Based on Eq. (3.13), the standard $\mathbf{CP}(\alpha)$ (i.e., $\mathbf{CP}_{11}(\alpha)$) and , $\mathbf{CP}_{01}(\phi)$ and $\mathbf{CP}_{10}(\phi)$ are obtained as follows:

$$\mathbf{CP}(\phi) = \langle 0|_W \tilde{X}_{AB}^\dagger \tilde{X}_W^\dagger \tilde{W}(\pi, \phi) \tilde{X}_{AB}|0\rangle_W , \tag{3.14a}$$

$$\mathbf{CP}_{01}(\phi) = \langle 0|_W \tilde{X}_B^\dagger \tilde{X}_W^\dagger \tilde{W}(\pi, \phi) \tilde{X}_B |0\rangle_W , \tag{3.14b}$$

$$\mathbf{CP}_{10}(\phi) = \langle 0|_W \tilde{X}_A^\dagger \tilde{X}_W^\dagger \tilde{W}(\pi, \phi) \tilde{X}_A |0\rangle_W . \tag{3.14c}$$

The $\mathbf{CP}_{00}(\alpha)$ in the center of Eq. (3.14a) is multiplied by $\tilde{X}_{AB}$ on one side and the Hermite conjugate of $\tilde{X}_{AB}$ on the other, exchanging and re-exchanging the coefficients of $|00\rangle$ and $|11\rangle$, respectively, resulting in a mapping $|11\rangle \to e^{i\alpha}|11\rangle$. And for $\mathbf{CP}_{01}(\phi)$ and $\mathbf{CP}_{10}(\phi)$ in Eq. (3.14b) and Eq. (3.14c), instead of $|11\rangle$, they are substituted with $|01\rangle$ and $|10\rangle$, respectively.

3.2.3 Arbitrary Two-Qubit State Generation

General two-qubit state generation U is to find a single operation that transforms the initial state $|00\rangle_{AB}$ into an arbitrary two-qubit state, which can be defined as follows:

$$U|00\rangle = a_0|00\rangle + a_1|01\rangle + a_2|10\rangle + a_3|11\rangle . \tag{3.15}$$

$U \in \mathrm{U}(2^2)$ (a unitary group U(4)) (in Eq. (3.15)) can in principle be composed of single- and two-qubit gates, it is sufficient to define general rotations and at least one inversion operation on the two-qubit basis $\{|00\rangle, |01\rangle, |10\rangle, |11\rangle\}$ of the AB atom, which is possible by the Householder decomposition [85].

Inversion operations are the mirrors of two-qubit state vectors with respect to a given plane. For instance, $\mathbf{CZ}$ inverts the state vector for the plane orthogonal to $|11\rangle$, so $\tilde{M}_{11} = \mathbf{CZ}$, and similarly, $\tilde{M}_{00} = \mathbf{CP}_{00}(\pi)$, $\tilde{M}_{01} = \mathbf{CP}_{01}(\pi)$, and $\tilde{M}_{10} = \mathbf{CP}_{10}(\pi)$.

General rotation is the rotation for a given two-qubit base-pair $j, k \in \{|00\rangle, |01\rangle, |10\rangle, |11\rangle\}$. $\tilde{R}_{00,01}(\Theta, \phi)$, defined as follows:

$$\tilde{R}_{jk}(\Theta, \phi)|j\rangle = \cos\frac{\Theta}{2}|j\rangle - ie^{i\phi}\sin\frac{\Theta}{2}|k\rangle . \tag{3.16}$$

For example, $\tilde{R}_{00,01}(\Theta, \phi)$, $\tilde{R}_{00,11}(\Theta, \phi)$, $\tilde{R}_{01,10}(\Theta, \phi)$, $\tilde{R}_{01,11}(\Theta, \phi)$, and $\tilde{R}_{00,01}(\Theta, \phi)$ are the rotations of the quantum information stored in the base pairs $\{|00\rangle, |01\rangle\}$, $\{|00\rangle, |11\rangle\}$, $\{|01\rangle, |10\rangle\}$, $\{|01\rangle, |11\rangle\}$ and

$\{|10\rangle, |11\rangle\}$ respectively, which are as follows:

$$\tilde{R}_{00,01}(\Theta, \phi) = \langle 0|_W \, \tilde{X}_W \tilde{X}_B \tilde{W}(\Theta, -\phi) \tilde{X}_B^\dagger \tilde{X}_W^\dagger |0\rangle_W \,, \tag{3.17a}$$

$$\tilde{R}_{00,11}(\Theta, \phi) = \langle 0|_W \, \tilde{X}_W \tilde{X}_{AB} \tilde{W}(\Theta, -(\phi + \pi/2)) \tilde{X}_{AB}^\dagger \tilde{X}_W^\dagger |0\rangle_W \,, \tag{3.17b}$$

$$\tilde{R}_{01,10}(\Theta, \phi) = \langle 0|_W \, \tilde{X}_B \tilde{X}_W \tilde{X}_{AB} \tilde{W}(\Theta, -(\phi + \pi/2)) \tilde{X}_{AB}^\dagger \tilde{X}_W^\dagger \tilde{X}_B^\dagger |0\rangle_W \,,, \tag{3.17c}$$

$$\tilde{R}_{01,11}(\Theta, \phi) = \langle 0|_W \, \tilde{X}_B \tilde{X}_W \tilde{X}_A \tilde{W}(\Theta, -\phi) \tilde{X}_A^\dagger \tilde{X}_W^\dagger \tilde{X}_B^\dagger |0\rangle_W \,, \tag{3.17d}$$

$$\tilde{R}_{10,11}(\Theta, \phi) = \langle 0|_W \, \tilde{X}_A \tilde{X}_W \tilde{X}_B, \tilde{W}(\Theta, -\phi) \tilde{X}_B^\dagger \tilde{X}_W^\dagger \tilde{X}_A^\dagger |0\rangle_W \,. \tag{3.17e}$$

In Eq. (3.17a), the first two π-pulse operations, $\tilde{X}_B^\dagger$ and $\tilde{X}_W^\dagger$, execute $|00\rangle_{AB} |0\rangle_W \to |00\rangle_{AB} |1\rangle_W$ and $|01\rangle_{AB} |0\rangle_W \to |00\rangle_{AB} |0\rangle_W$, respectively, which implies that the quantum state of B atom is transferred to the W atom. Then the state vector of W atom is rotated by $\tilde{W}(\Theta, -\phi)$ and delivered back to B atom by the last two π-pulse operations.

3.2.4 Multi-Qubit Gates

Multi-qubit gates can be decomposed into a series of single-qubit and two-qubit elementary gates. However, standard three-qubit gates require many elementary gates (e.g., the Toffoli gate requires 15 or 17 elementary gates). In this subsection, we examine the possibility of reducing the number of gates significantly by using wire-atom arrangements in Toffoli gate and **CCZ** gate, which are prominent examples of standard three-qubit gates.

If a simple linear configuration of ABC data atoms and two wire atoms W_1 and W_2 is used, as in Fig. 3.3 (a), the pulse-sequence solutions are rather complicated, as in the Toffoli and **CCZ** gate examples in Eqs. (3.18):

$$\begin{aligned}
\mathbf{CCZ} &= \langle 00|_{W_{12}} \sqrt{\tilde{Y}_C} \tilde{Y}_{AB} \tilde{X}_{W_2}^\dagger \tilde{Y}_{W_1} \tilde{X}_{BC}^\dagger \sqrt{\tilde{X}_{W_2}} \tilde{X}_{BC}^2 \\
&\quad \times \sqrt{\tilde{X}_{W_2}^\dagger} \tilde{X}_{BC}^\dagger \tilde{X}_{W_{12}} \tilde{Y}_{AB}^\dagger \sqrt{\tilde{Y}_C^\dagger} |00\rangle_{W_{12}} \,,
\end{aligned} \tag{3.18a}$$

$$\begin{aligned}
\mathbf{TOFF} &= \langle 00|_{W_{12}} \sqrt{\tilde{Y}_B^\dagger \tilde{Y}_C} \tilde{Y}_{AB} \tilde{X}_{W_2}^\dagger \tilde{Y}_{W_1} \tilde{X}_{BC}^\dagger \sqrt{\tilde{X}_{W_2}} \tilde{X}_{BC}^2 \\
&\quad \times \sqrt{\tilde{X}_{W_2}^\dagger} \tilde{X}_{BC}^\dagger \tilde{X}_{W_{12}} \tilde{Y}_{AB}^\dagger \sqrt{\tilde{Y}_C^\dagger \tilde{Y}_B} |00\rangle_{W_{12}} \,.
\end{aligned} \tag{3.18b}$$

However, if the Y-shape configuration of Fig. 3.3 (b) is used instead, where one wire atom W couples all three data atoms, ABC, simultaneously, then their simple solutions are obtained as extensions of **CX** and **CZ** in Eq. (3.9) and Eq. (3.10). Utilizing the fact that $\langle 0|_W \tilde{Y}_W^2 |0\rangle_W$ is the inverted-**CCZ**, we obtain the following results:

$$\mathbf{CCZ} = \langle 0|_W \tilde{Y}_{ABC}^\dagger \tilde{Y}_W^2 \tilde{Y}_{ABC} |0\rangle_W \,, \tag{3.19a}$$

$$\mathbf{TOFF}_{ABC} = \langle 0|_W \sqrt{\tilde{Y}_C^\dagger} \tilde{Y}_{AB}^\dagger \tilde{Y}_W^2 \tilde{Y}_{AB} \sqrt{\tilde{Y}_C} |0\rangle_W \,. \tag{3.19b}$$

In Eqs. (3.19), $\tilde{Y}_{ABC} \equiv \tilde{Y}_A \tilde{Y}_B \tilde{Y}_C$ and $\tilde{Y}_{ABC}^\dagger$ are applied before and after changing the inverted-**CCZ** to **CCZ** as bit-wise flip and flip-back of the data atoms, respectively. The Toffoli gate **TOFF**$_{ABC}$ for AB controls and C target (Eq. (3.19b), whose quantum circuit is presented in Fig. 3.3 (c)), the $\sqrt{\tilde{Y}_C^\dagger}$ C and $\sqrt{\tilde{Y}_C}$ at both ends are the pseudo-Hadamard and its inverse acting on the target.

(a)

(b)

(c) Toffoli gate $\mathbf{TOFF}_{ABC}$
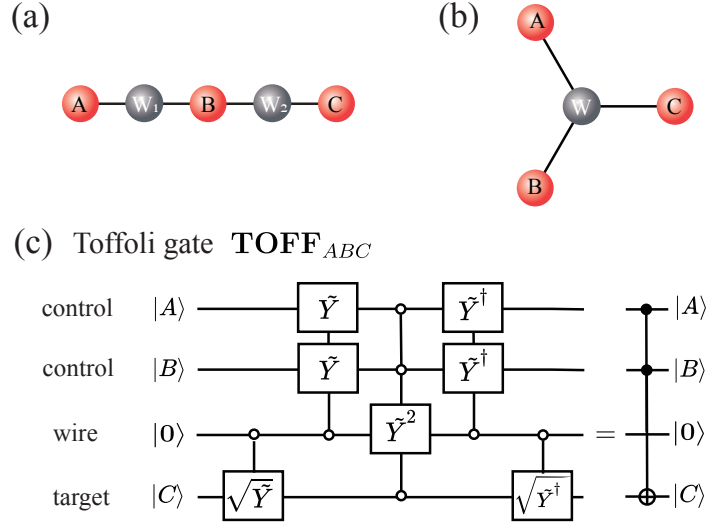
Figure 3.3: (a) A 5-atom chain and (b) an Y-shape atomic array to implement the multi-qubit wire gates. (c) Quantum circuit of the Toffoli gate $\mathbf{TOFF}_{ABC}$ for the control atoms A, B and the target atom C. The figure is reused from the reference [83], Frontiers Media S.A..

3.3 Summary

Rydberg wire gates utilizing auxiliary atoms to couple data atoms are proposed. The universal set of gates can be realized based on the strong local interaction of neutral Rydberg atoms by coding information into qubits comprising a ground state and a Rydberg state. These gates are implemented via fast laser excitation of the Rydberg state, which allows fast operation and rapid entanglement of well-separated data atoms. Fast entangling operations are basic building blocks of quantum circuits for large-scale quantum computation, and long-range entanglement enables greatly simplified operations between distant qubits in the array. The new idea of Rydberg wire gates can lead to new prospects for neutral-atom quantum science and technology.

Chapter 4. Rydberg-based Quantum Programming of Satisfiability Instances

Decision problems are categorized into deterministic polynomial (**P**) problems and nondeterministic polynomial (**NP**) problems based on their computational complexity (Table. 2.1 in Sec. 2.2). **P** problem is the problem that can be solved in polynomial time with a Deterministic Turing machine (DTM), which is the framework of a classical computer [45, 46], and there is an algorithm that can uniquely determine the next status given the current status. In other words, it is the problem that is efficiently solvable with classical computing. On the other hand, an **NP** problem is a problem that can be solved in polynomial time by a non-deterministic Turing machine (NTM), which, different from a DTM, follows a tree-like computation path consisting of multiple branches per step. In other words, it is the hard problem that is verifiable by a DTM in polynomial time [45], but there is no classical algorithm that can efficiently solve it unless P = NP [46, 86]. And, as mentioned in Sec. 2.2, **NP-complete** problem is the most difficult **NP** problem which is the problem that all **NP** problems can be reduced by many-one reduction in polynomial time, i.e., it belongs to **NP-hard** problems.

Currently, there are considerable efforts to build quantum computers [5, 87, 88], and an important challenge is to engineer quantum systems that can formulate quantum algorithms for efficiently solving classically hard computational problems, such as NP-complete problems [89, 90]. And according to the definition of NP-complete problems, an algorithm that can efficiently solve an NP-complete problem can be used as a subroutine of an efficient algorithm for solving all other NP problems [45, 46, 49]. In other words, if a quantum computer can solve these NP-complete problems efficiently, then there is a potential for all other NP instances to be solved efficiently via polynomial time reduction to NP-complete problems [91, 92]. Hence, in this chapter, we will introduce some examples of Karp's 21 NP-complete problems [93], which are representative NP-complete problems, and how they are transformed into instances of the maximum independent set (MIS) problem, which is one of the NP-complete problems, and then describe the Rydberg-based quantum programming of the Boolean satisfiability instances (SAT or B-SAT) and the 3-SAT instances, which are proto-typical NP-complete instances according to the Cook-Levin theorem [94].

This chapter is based on the published paper: S. Jeong, M. Kim, M. Hhan, J. Park, and J. Ahn, "Quantum programming of the satisfiability problem with Rydberg atom graphs," Phys. Rev. Res. **5**, 043037 (2023) [72].

4.1 Karp's 21 NP-complete Problems

A prominent examples of such NP-complete problems are Karp's 21 NP-complete Problems [93], and, in this section, we will briefly introduce some examples of Karp's 21 NP-complete Problems.

4.1.1 Satisfiability (SAT)

Satisfiability (**SAT** or **B-SAT**) is the problem to determine whether a given propositional logic expression (Boolean expression) $\Psi(x_1, x_2, \cdots)$ is *satisfiable* (i.e., whether there exists a Boolean variable value $(x_1, x_2, \cdots)$ such that $\Psi(x_1, x_2, \cdots)$ is true), and is the first problem which was proved to be NP-complete by the Cook-Levin theorem [94]. The Boolean expression $\Psi(x_1, x_2, \cdots)$ of the SAT problem can be written in conjunctive normal form (CNF) [95], i.e., as a conjunction of N_C clauses $C_j \equiv \bigvee_m l_{j,m}$ defined as a disjunction of literals $\ell_{j,m}$ which are Boolean variables or their negations, as follows:

$$\Psi(x_1, x_2, \cdots) = \bigwedge_{j=1}^{N_C} C_j. \tag{4.1}$$

And SAT problems where the maximum number of literals that make up each clause is k are called k-SAT problems, and examples include 2-SAT and 3-SAT. 2-SAT is in the P class, and 3-SAT is an NP-complete problem.

3-SAT

3-SAT problem is a class of SAT problem whose every clause comprising the CNF of a given Boolean expression consists of at most three literals, and all instances of the SAT problem are reducible to 3-SAT in polynomial-time [93]. By the definition of 3-SAT, a 3-SAT formula is as follows:

$$
\begin{aligned}
\Psi(x_1, x_2, \cdots, x_n) &= \bigwedge_{j=1}^{N_C} C_j & \text{(4.2a)} \\
C_j &= \ell_{j,1} \vee \ell_{j,2} \quad \text{or} \quad \ell_{j,1} \vee \ell_{j,2} \vee \ell_{j,3}, & \text{(4.2b)}
\end{aligned}
$$

where $\ell_{j,1}, \ell_{j,2}, \ell_{j,3} \in \{x_k, \bar{x}_k | k = 1, \cdots, n\}$ [49, 93].

4.1.2 Set Packing (Equivalent to the Independent Set)

Set Packing is an NP-complete problem in computational complexity theory and combinatorics, and is one of the 21 NP-complete problems proposed by Karp [93]. Given a finite set S and a list of subsets of S, the set packing problem asks whether some k subsets of the list are pairwise disjoint (i.e., the two sets do not share an element) [93]. More formally, given a finite universe $\mathcal{U}$ and a family $\mathcal{S}$ of subsets of $\mathcal{U}$, a set packing is a subfamily $\mathcal{C} \subseteq \mathcal{S}$ consisting of sets that belong to $\mathcal{S}$ and are pairwise disjoint from each other. The set packing decision problem is to find a set packing $\mathcal{C}$ such that $|\mathcal{C}| \geq k$ for a given pair $(\mathcal{U}, \mathcal{S})$ and integer k [93], and the **Maximum Set Packing** problem is an optimization problem to find the set packing $\mathcal{C}$ with the largest $|\mathcal{C}|$ for a given pair $(\mathcal{U}, \mathcal{S})$ [49].

For example, for a given universe $\mathcal{U} = \{W_1, W_2, W_3, W_4, e_1, e_2, e_3, e_4, e_5, e_6, e_7, e_8\}$ and a subset family $\mathcal{S} = \{S_1, S_2, \cdots S_8 (\subseteq \mathcal{U})\}$, let $S_1 = \{e_1, e_4, e_5\}$, $S_2 = \{e_1, e_2, e_6\}$, $S_3 = \{e_2, e_3, e_7\}$, $S_4 = \{e_3, e_4, e_8\}$, $S_5 = \{e_8, W_1, W_4\}$, $S_6 = \{e_5, W_1, W_2\}$, $S_7 = \{e_6, W_2, W_3\}$, $S_8 = \{e_7, W_3, W_4\}$, then the set packing $\mathcal{C}$ of maximum cardinality in the pair $(\mathcal{U}, \mathcal{S})$ is of two kinds, $\{S_1, S_3, S_5, S_7\}$ and $\{S_2, S_4, S_6, S_8\}$.

Also, the **Set packing** problem is equivalent to the **Independent set** problem, with the one-to-one polynomial-time reduction that follows:

Set packing → Independent set:

For the set packing problem of a given collection $\mathcal{S}$,

1. $\mathcal{S} \mapsto$ a graph $G(V, E)$,
2. $S \in \mathcal{S} \mapsto v_S \in V$,
3. $S \cap T \neq \varnothing \mapsto (v_S, v_T) \in E$,

then every independent set $I \subseteq V$ of $G(V, E)$ corresponds to a set packing of $\mathcal{S}$.

Similarly, by this reduction, the **Maximum Set Packing** problem corresponds to the **Maximum independent set** (**MIS**) problem described in Subsec. 2.2.1, where MIS corresponds to maximum set packing.

4.1.3 Graph Coloring

Figure 4.1: **Graph Coloring** of a non-planar graph $G(V, E)$ with ten nodes,

The **Graph Coloring** problem is the problem of determining whether the node set V can be colored with k colors (i.e., is k-colorable) such that adjacent points in a given graph $G(V, E)$ are distinguished, and is formally defined as [49]:

Graph Coloring: Check whether no two adjacent nodes (i.e., $u, v \in V$ with $(u, v) \in E$) share the same color using only k colors (i.e., k-colorable) for a given graph $G(V, E)$.

For example, the non-planar graph $G(V, E)$ in Fig. 4.1, which contains the complete non-planar subgraph K_5 composed by the node subset $W_0 = \{0, 1, 2, 3, 4\} \subset V$, requires at least five colors.

4.1.4 Exact Cover

The **Exact Cover** problem is a special case of the **Set Packing** problem, which is the decision problem of finding the existence of a set packing $\mathcal{C}' \subseteq \mathcal{S}$ such that, for a given total set $\mathcal{U}$ and a family $\mathcal{S}$ of subsets of $\mathcal{U}$, the union of subsets $S \in \mathcal{C}'$ is $\mathcal{U}$ [49, 93]. Formally, it is defined as follows:

Exact Cover: Check whether there is a set packing $\mathcal{C}' \subseteq \mathcal{S}$ such that $\bigcup_{S \in \mathcal{C}'} S = \mathcal{U}$, for a given total set $\mathcal{U}$ and a family $\mathcal{S}$ of subsets of $\mathcal{U}$.

Here are two examples of the exact cover problem:

Case 1 (Exact Cover exists)

For a given total set $\mathcal{U} = \{x_1, x_2, \cdots, x_{10}\}$ and a subset family $\mathcal{S}$ of $\mathcal{U}$, when the subsets S_1, S_2, S_3, S_4 belonging to $\mathcal{S}$ are equal to Eqs. (4.3),

$$
\begin{align}
S_1 &= \{x_1, x_2, x_3, x_6\} \tag{4.3a} \\
S_2 &= \{x_4, x_5, x_7, x_8, x_9, x_{10}\} \tag{4.3b} \\
S_3 &= \{x_1, x_5, x_{10}\} \tag{4.3c} \\
S_4 &= \{x_1, x_2, x_4, x_8\} \tag{4.3d}
\end{align}
$$

the relations of Eqs. (4.4) hold:

$$
\begin{align}
S_1 \cap S_2 &= \varnothing \tag{4.4a} \\
S_1 \cap S_3 &= \{x_1\} \tag{4.4b} \\
S_1 \cap S_4 &= \{x_1, x_2\} \tag{4.4c} \\
S_2 \cap S_3 &= \{x_5, x_{10}\} \tag{4.4d} \\
S_2 \cap S_4 &= \{x_4, x_8\} \tag{4.4e} \\
S_3 \cap S_4 &= \{x_1\} \tag{4.4f} \\
S_1 \cup S_2 &= U. \tag{4.4g}
\end{align}
$$

Due to Eq. (4.4g), the exact cover in this case is $\mathcal{C}' = \{S_1, S_2\}$.

Case 2 (No Exact Cover exists)

For a given total set $\mathcal{U} = \{x_1, x_2, \cdots, x_{10}\}$ and a subset family $\mathcal{S}$ of $\mathcal{U}$, when the subsets S_1, S_2, S_3, S_4, S_5 belonging to $\mathcal{S}$ are equal to Eqs. (4.5),

$$S_1 = \{x_1, x_2, x_3\} \tag{4.5a}$$
$$S_2 = \{x_3, x_4\} \tag{4.5b}$$
$$S_3 = \{x_5, x_6\} \tag{4.5c}$$
$$S_4 = \{x_6, x_7, x_8\} \tag{4.5d}$$
$$S_5 = \{x_9, x_{10}\} \tag{4.5e}$$

the relation Eqs. (4.6) holds for $j, k \in \{1, 2, \cdots, 5\}(j < k)$:

$$S_j \cap S_k = \begin{cases} \{3\} & \text{for } j = 1, k = 2 \\ \{6\} & \text{for } j = 3, k = 4 \\ \varnothing & \text{otherwise} \end{cases} \tag{4.6a}$$

$$S_1 \cup S_3 \cup S_5 = \{x_1, x_2, x_3, x_5, x_6, x_9, x_{10}\} \tag{4.6b}$$
$$S_1 \cup S_4 \cup S_5 = \{x_1, x_2, x_3, x_6, x_7, x_8, x_9, x_{10}\} \tag{4.6c}$$
$$S_2 \cup S_3 \cup S_5 = \{x_3, x_4, x_5, x_6, x_9, x_{10}\} \tag{4.6d}$$
$$S_2 \cup S_4 \cup S_5 = \{x_3, x_4, x_6, x_7, x_8, x_9, x_{10}\}. \tag{4.6e}$$

In this case, by Eqs. (4.6), the exact cover does not exist.

4.1.5 Max Cut

The **Max Cut** problem is the problem of partitioning a set of nodes V in a given graph $G(V, E)$ such that the number of edges between two subsets S and $V \backslash S$ is maximized [96]. The formal definition of this problem is as follows:

Max Cut: Maximize the number of edges $(u, v) \in E$ such that $u \in S$ and $v \in V \backslash S$, for a given graph $G(V, E)$.

In the instance of the Max Cut problem for the graph $G(V, E)$ in Fig. 4.2, when the node set V is partitioned into two subsets $A = \{1, 2, 4, 6, 10\}$ and $B = V \backslash A$, the maximum number of connected edges (i.e., cutedges) between the two partitions A and B is 6, which corresponds to a maximum cut.

4.1.6 Binary Integer Programming (BIP)

Binary Integer Programming (**BIP**) is a type of Integer Linear Programming (ILP), which is defined as the problem of determining an $\vec{x} \in \{0, 1\}^N$ that finds the maximum value of the objective function $\vec{c} \cdot \vec{x}$ under the constraint $S \cdot \vec{x} = \vec{b}$, given an $(m \times N)$- matrix S $(N > m)$ and constant vectors $\vec{b} \in \mathbb{R}^m$, $\vec{c} \in \mathbb{R}^N$ [97]. The formal definition is as follows:

Binary Integer Programming (**BIP**):
For $\vec{x} \in \{0, 1\}^N$, $S \in \mathbb{R}^{m \times N}$, $\vec{b} \in \mathbb{R}^m$, $\vec{c} \in \mathbb{R}^N$, maximize $\vec{c} \cdot \vec{x}$ under the constraint $S \cdot \vec{x} = \vec{b}$.

Example of a Max Cut Partition (Sample Cut)
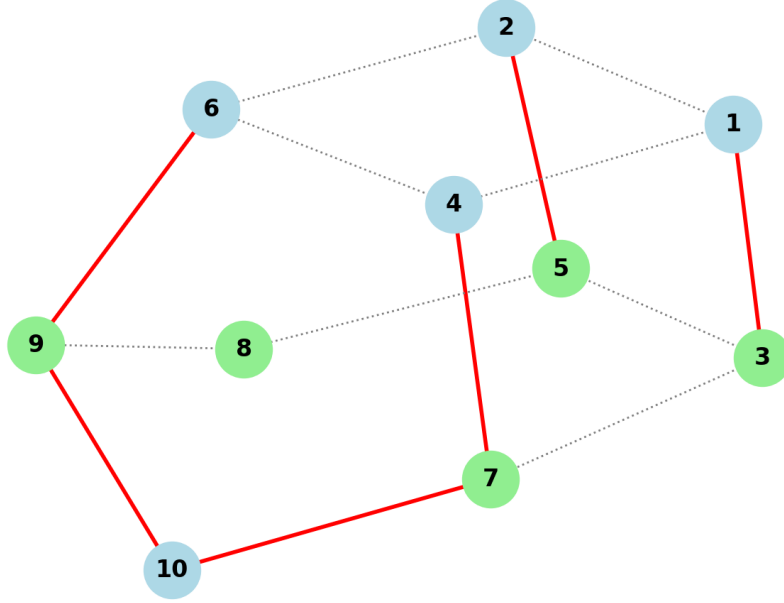
Figure 4.2: Maximum cut (Max Cut) of a connected graph $G(V, E)$ with 10 nodes, The red-edges are the cut edges, i.e., those that cross between the two partitions $A = \{1, 2, 4, 6, 10\}$ and $B = \{3, 5, 7, 8, 9\}$ of V. And the other edges (gray dotted) are not part of the cut.

There are two instances of BIP:

Case 1 (Feasible Constraint System)

Given a matrix S and vectors $\vec{b}$, $\vec{c}$ as in Eqs. (4.7),

$$S = \begin{bmatrix} 4 & 6 & 3 & 4 \\ 1 & 1 & 1 & 1 \\ 1 & 0 & 0 & 1 \end{bmatrix}, \tag{4.7a}$$

$$\vec{b} = \begin{bmatrix} 10 \\ 2 \\ 1 \end{bmatrix}, \tag{4.7b}$$

$$\vec{c} = \begin{bmatrix} 9 \\ 11 \\ 6 \\ 9 \end{bmatrix}. \tag{4.7c}$$

under the constraint $S \cdot \vec{x} = \vec{b}$, $\vec{x} \in \{0, 1\}^4$ that maximizes the objective function $\vec{c} \cdot \vec{x}$ is given by Eq. (4.8):

$$\vec{x} = \begin{bmatrix} 0 \\ 1 \\ 0 \\ 1 \end{bmatrix} \quad \text{or} \quad \begin{bmatrix} 1 \\ 1 \\ 0 \\ 0 \end{bmatrix}. \tag{4.8}$$

Case 2 (Infeasible Constraint System)

Suppose the matrix S and vectors $\vec{b}$, $\vec{c}$ are given as in Eqs. (4.9):

$$S = \begin{bmatrix} 1 & -1 & 0 & 0 \\ 0 & 0 & 1 & 1 \\ 1 & 0 & -1 & -1 \end{bmatrix}, \tag{4.9a}$$

$$\vec{b} = \begin{bmatrix} -1 \\ 1 \\ 3 \end{bmatrix}, \tag{4.9b}$$

$$\vec{c} = \begin{bmatrix} -1 \\ 2 \\ 1 \\ 1 \end{bmatrix}. \tag{4.9c}$$

Then, under the constraint $S \cdot \vec{x} = \vec{b}$, the relations as in Eqs. (4.10) are obtained:

$$x_1 - x_2 = -1, \tag{4.10a}$$

$$x_3 + x_4 = 1, \tag{4.10b}$$

$$x_1 - x_3 - x_4 = 3. \tag{4.10c}$$

For this instance, Eq. (4.10b) and Eq. (4.10c) contradict each other, making the constraint $S \cdot \vec{x} = \vec{b}$ infeasible, so there is no $\vec{x} \in \{0, 1\}^4$ that satisfies this constraint.

4.1.7 Number Partitioning / Undirected Hamiltonian Cycle / Clique / Clique Cover

Number Partitioning

Number Partitioning is the problem of finding a set $S = \{s_1, s_2, \cdots, s_N\}$ of natural numbers that can be divided into two disjoint subsets S_1 and S_2 such that the sums of the elements in S_1 and S_2 are the same for each other [49, 93]. This problem is formally defined as follows:

Number Partitioning: Determine whether a set $S = \{s_1, s_2, \cdots, s_N\}$ of natural numbers can be bipartitioned into two subsets S_1 and S_2 such that

$$\sum_{x \in S_1} x = \sum_{y \in S_2} y.$$

The following two examples are examples of instances that can and cannot be number partitioned:

Case 1 (Number partition exists)
For $S = \{3, 1, 1, 2, 2, 1\}$, S is number partitionable into $S_1 = \{3, 2\}$ and $S_2 = \{1, 1, 2, 1\}$.

Case 2 (Number partition does not exist)
For $S = \{4, 7, 2, 5, 3\}$, since the sum $4 + 7 + 2 + 5 + 3 = 21$ of all elements in S is an odd number, so this S is not possible to be number partitioned.

Undirected Hamiltonian Cycle

The **Undirected Hamiltonian Cycle** problem is to find a Hamiltonian cycle, a simple cycle that visits each node $v \in V$ exactly once and returns to the starting point, for a given undirected graph $G(V, E)$ [49, 93]. In Figs. 4.3, the two examples of the undirected Hamiltonian cycle problem for two graphs: the one in Fig. 4.3 (a) with a Hamiltonianian cycle $(0 \to 1 \to 2 \to 3 \to 4 \to 5 \to 6 \to 7 \to 8 \to 9 \to 0)$ and the other in Fig. 4.3 (b) with no Hamiltonian cycle due to the bottleneck node 9.

Clique

The **Clique** problem is the problem of finding a clique $C (\subseteq G)$, i.e., a m-complete subgraph $C = K_m$, whose size is a positive integer $m > 0$, for a given graph G. Formally, it is defined as follows:

Clique: Find an m-complete subgraph (i.e. a clique whose size is m) C of G for a positive integer m and a given graph G.

Furthermore, there is a duality that the node set of a clique of a graph G corresponds to the independent set of its complement graph $\overline{G}$. Thus, the **Maximum independent set (MIS)** problem of a graph G is dual to the **Maximum Clique** problem of its complement graph $\overline{G}$.

Clique Cover

The **Clique Cover** problem is the problem of determining, for a given graph $G(V, E)$ and a positive integer $m > 0$, whether a node set V can be partitioned into m different cliques. The formal definition is as follows:

Clique Cover: For a graph $G(V, E)$ and a positive integer $m > 0$, partition $G(V, E)$ into m different cliques with respect to the node set V.

For the 15-node graph in Fig. 4.4, a solution to the **Clique Cover** problem with $m = 5$ is $\{\{0, 2, 11, 14\}, \{1, 5, 7\}, \{3, 4, 6, 8\}, \{9\}, \{10, 12, 13\}\}$, as shown in Fig. 4.4.

Moreover, similar to the case of the **Clique** problem, the **Clique Cover** problem for a graph G is dual to the **Graph Coloring** problem for its complement graph $\overline{G}$ (i.e., determining whether $\overline{G}$ is m-colorable).

(a)

Graph With Hamiltonian Cycle (Minimum Degree ≥ 4)
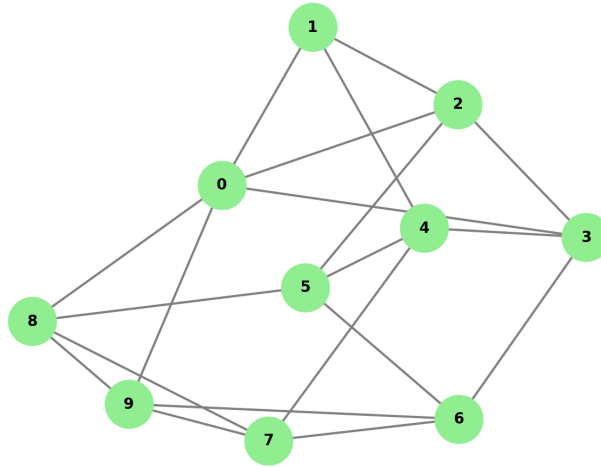
(b)

Non-Hamiltonian Graph With 14 Nodes
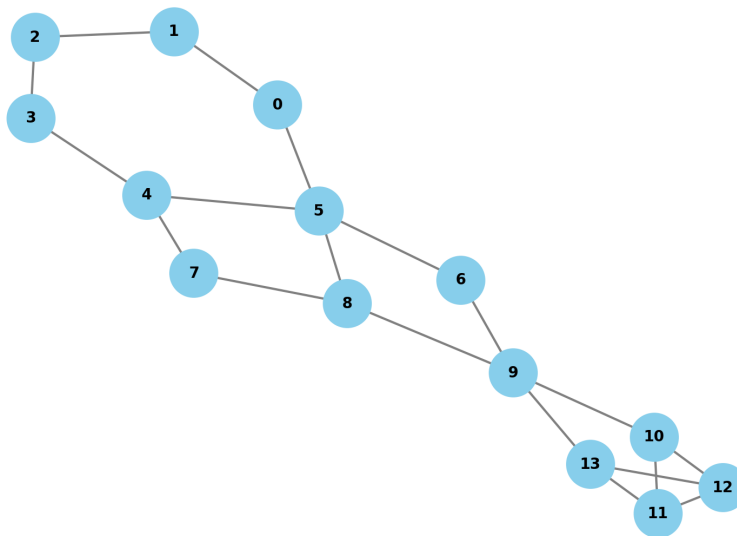
Figure 4.3: Two examples of the **Undirected Hamiltonian Cycle** problem.

4.2 Mathematical Reduction from NP-complete problem to MIS problem

Previously, in Sec. 4.1, we introduced several examples of Karp's 21 NP-complete problems, which are prominent NP-complete problems. In this section, we will discuss how these NP-complete problems can be reduced to the **Maximum independent set** (**MIS**) problem, which is the NP-complete problem equivalent to the set packing problem.
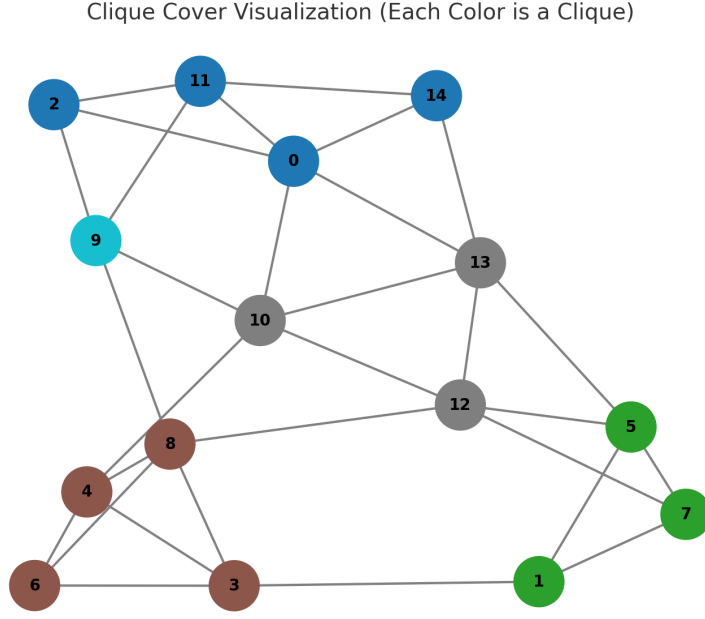
Figure 4.4: Example of the **Clique Cover** problem for a graph with 15 nodes. Each clique from the cover is distingushed via five different colors.

4.2.1 3-SAT to MIS

As mentioned in Subsec. 4.1.1, all instances of the SAT problem can be transformed into the 3-SAT domain by a polynomial-time reduction to 3-SAT problem. Then, the 3-SAT formula given by Eqs. (4.2) is transformed into the instance of MIS problem over the graph $G_M(V, E)$ by the reduction defined by Eqs. (4.11):

$$V = \{(j, k) | \ell_{j,k} \in C_j\}, \tag{4.11a}$$

$$E = E_1 \cup E_2, \tag{4.11b}$$

$$E_1 = \{[(j, k_1), (j, k_2)] | k_1 \neq k_2\}, \tag{4.11c}$$

$$E_2 = \{[(j_1, k_1), (j_2, k_2)] | k_1 \neq k_2, \ell_{j_1,k_1} = \bar{\ell}_{k_2,k_2}\}, \tag{4.11d}$$

where V is the set of nodes $v_{(j,k)}$ corresponding to literal $\ell_{j,k}$ in j-th clause C_j, and E is the set of all edges in G_M, which is the union of two edge sets E_1 and E_2; E_1 is the set of intra-clause edges connecting two nodes mapped from literals ℓ_{j,k_1} and ℓ_{j,k_2} in the same clause C_j, and E_2 is the set of inter-clause edges connecting two nodes mapped from literals that are negation to each other in different clauses [97, 98]. If the MIS size of the graph $G_M(V, E)$ is equal to the number of all clauses in the 3-SAT formula, then the 3-SAT formula is *satisfiable*.

4.2.2 Graph Coloring to MIS

As described in Subsec. 4.1.3, the **Graph Coloring** problem is the problem of determining whether a given graph $G(V, E)$ can be colored so that adjacent nodes are color distinguishable (i.e., m-colorable) using only m colors, and the constraints of the graph coloring problem are as follows:

GC1. Each node $v \in V$ must be colored by only one color $j \in \{1, 2, \cdots, m\}$.

GC2. Adjacent nodes u and v that are connected by an edge $(u, v) \in E$ should be colored with different colors to distinguish them.

Here, the constraint **GC1** can be regarded as the **MIS** problem of the m-complete graph K_m assigned to each node $v \in V$, and **GC2** as the **Independent Set** definition of the graph $G(V, E)$ replicated for each color $j \in \{1, 2, \cdots, k\}$.

Thus, the objective functions representing constraints **GC1** and **GC2** are represented by the cost Hamiltonians $\hat{H}_{\text{GC1}}$ and $\hat{H}_{\text{GC2}}$ as shown in Eqs. (4.12):

$$\hat{H}_{\text{GC1}} = \sum_{v \in V} \left[U \sum_{j=1}^{k} \sum_{l>j} \hat{n}_{v,j} \hat{n}_{v,l} - \Delta \sum_{j=1}^{k} \hat{n}_{v,j} \right], \tag{4.12a}$$

$$\hat{H}_{\text{GC2}} = U \sum_{j=1}^{k} \sum_{(u,v) \in E} \hat{n}_{u,j} \hat{n}_{v,j}, \tag{4.12b}$$

where $0 < \Delta < U$. Thus, since the cost Hamiltonians $\hat{H}_{\text{GC1}}$ and $\hat{H}_{\text{GC2}}$ do not share any terms with each other, the total cost Hamiltonian $\hat{H}_{\text{GC}}$ for the graph coloring problem can be given by Eqs. (4.13):

$$\hat{H}_{\text{GC}} = \hat{H}_{\text{GC1}} + \hat{H}_{\text{GC2}} \tag{4.13a}$$

$$= -\Delta \sum_{v \in V} \sum_{j=1}^{k} \hat{n}_{v,j} + U \left[\sum_{v \in V} \sum_{j=1}^{k} \sum_{l>j} \hat{n}_{v,j} \hat{n}_{v,l} + \sum_{j=1}^{k} \sum_{(u,v) \in E} \hat{n}_{u,j} \hat{n}_{v,j} \right]. \tag{4.13b}$$

4.2.3 Exact Cover to MIS

As mentioned in Subsec. 4.1.4, the **Exact Cover** problem is the problem to determine whether, given a total set $\mathcal{U}$ and its subset family $\mathcal{S}$, it is possible to partition it into disjoint subsets of $\mathcal{S}$. So, the constraints of the exact cover problem are as follows:

EC1. Subsets $S_j, S_k \in \mathcal{C}$ which belong to $\mathcal{C} \subseteq \mathcal{S}$ must be disjoint from each other (i.e., $S_j \cap S_k = \varnothing$), i.e., each element $x_p \in \mathcal{U}$ of the total set $\mathcal{U}$ must belong to only one kind of $S_j \in \mathcal{C}$.

EC2. The union of all $S \in \mathcal{C}$ must be the total set $\mathcal{U}$.

Similar to the graph coloring problem, **EC1** can be divided into two parts:

EC1-1: The **MIS** problem of the m_p-complete graph K_{m_p} ($m_p = |\mathcal{B}_p|$, where $\mathcal{B}_p = \{S_j | x_p \in S_j\}$) assigned to each element x_p, similar to GC1

EC1-2: The definition of an **Independent Set** based on the disjointness of each subset S_j and S_k chosen in **EC1-1**, similar to GC2.

And **EC2** is the decision problem of determining whether the size of the MIS in **EC1** is equal to the cardinality $|\mathcal{U}|$ of the total set.

Accordingly, the cost Hamiltonians $\hat{H}_{\text{EC1}-1}$ and $\hat{H}_{\text{EC1}-2}$ corresponding to **EC1-1** and **EC1-2** are given by Eqs. (4.14):

$$\hat{H}_{\text{EC1}-1} = \sum_{x_p \in \mathcal{U}} \left[U \sum_{S_j, S_k \in \mathcal{B}_p; k>j} \hat{n}_{p,j} \hat{n}_{p,k} - \Delta \sum_{S_j \in \mathcal{B}_p} \hat{n}_{p,j} \right], \tag{4.14a}$$

$$\hat{H}_{\text{EC1}-2} = U \sum_{S_j \cap S_k \neq \varnothing; k>j} \left[\sum_{x_p \in S_j} \sum_{x_q \in S_k} \hat{n}_{p,j} \hat{n}_{q,k} \right], \tag{4.14b}$$

41

where $0 < \Delta < U$. Similar to the graph coloring problem, the total cost Hamiltonian $\hat{H}_{\text{EC}}$ for the exact cover problem is the sum of $\hat{H}_{\text{EC1}-1}$ and $\hat{H}_{\text{EC1}-2}$, expressed as Eqs. (4.15):

$$
\begin{aligned}
\hat{H}_{\text{EC}} &= \hat{H}_{\text{EC1}-1} + \hat{H}_{\text{EC1}-2} && \text{(4.15a)} \\
&= -\Delta \sum_{x_p \in \mathcal{U}} \sum_{S_j \in \mathcal{B}_p} \hat{n}_{p,j} \\
&\quad + U \left[\sum_{x_p \in \mathcal{U}} \sum_{S_j, S_k \in \mathcal{B}_p; k>j} \hat{n}_{p,j}\hat{n}_{p,k} + \sum_{S_j \cap S_k \neq \varnothing; k>j} \left(\sum_{x_p \in S_j} \sum_{x_q \in S_k} \hat{n}_{p,j}\hat{n}_{q,k} \right) \right]. && \text{(4.15b)}
\end{aligned}
$$

Finally, according to **EC2**, an exact cover exists for a given pair $(\mathcal{U}, \mathcal{S})$ if, when comparing the MIS sizes of the graphs in the $\hat{H}_{EC}$, the MIS size in the graph from the $\hat{H}_{EC}$ is of size $|\mathcal{U}|$ of the set.

4.2.4 Max Cut to MIS

As explained in Subsec. 4.1.5, the **Max Cut** problem is the problem of bipartitioning a set V of nodes in a given graph $G(V, E)$ into S and $V \backslash S$ such that the number of edges between the two subsets of nodes is maximized. Thus, the cost Hamiltonian $\hat{H}_{\text{MaxCut}}$ of the **Max Cut** problem is given by Eqs. (4.16):

$$
\begin{aligned}
\hat{H}_{\text{MaxCut}} &= \sum_{(u,v) \in E} \left[\hat{n}_u (\hat{n}_v - 1) + (\hat{n}_u - 1)\hat{n}_v \right] && \text{(4.16a)} \\
&= \sum_{(u,v) \in E} \left[2\hat{n}_u \hat{n}_v - \hat{n}_u - \hat{n}_v \right] && \text{(4.16b)} \\
&= -\sum_{v \in V} w_v \cdot \hat{n}_v + 2 \sum_{(u,v) \in E} \hat{n}_u \hat{n}_v, && \text{(4.16c)}
\end{aligned}
$$

where $\hat{n}_v$ is the occupation number indicating whether node v is in S or not (i.e., if $\hat{n}_v = 1$, then $v \in S$), and w_v is the degree of v, which is the number of edges connected to node v. In other words, the cost Hamiltonian of the max cut problem is represented by the Quadratic unconstrained binary optimization (**QUBO**) problem in Eq. (4.16c) [99, 100], and accordingly, the max cut problem can be transformed into the QUBO domain and then into the MIS graph of the QUBO problem with data-, offset-qubit and even-, odd-atom quantum wires [101].

4.2.5 Binary Integer Programming (BIP) to MIS

As introduced in Subsec. 4.1.6, the **Binary Integer Programming** (**BIP**) problem is an Integer Linear Programming (ILP) problem that finds an N-bit vector $\vec{x} \in \{0,1\}^N$ that maximizes the value of an objective function determined by vector $\vec{c} \in \mathbb{R}^N$ under the constraints of a linear equation system of a given matrix $S \in \mathbb{R}^{N \times m}$ and vector $\vec{b} \in \mathbb{R}^m$:

BIP1. Binary vector $\vec{x} \in \{0,1\}^N$ must satisfy the linear equation system $S \cdot \vec{x} = \vec{b}$.

BIP2. $\vec{x}$ should maximize the objective function $\vec{c} \cdot \vec{x}$.

The cost Hamiltonians $\hat{H}_{\mathrm{BIP1}}$ and $\hat{H}_{\mathrm{BIP2}}$ accounting for these constraints **BIP1** and **BIP2** are given by Eqs. (4.17):

$$
\hat{H}_{\mathrm{BIP1}} = \sum_{j=1}^{m}\left[b_j - \sum_{i=1}^{N} S_{ji}\hat{n}_i\right]^2 \tag{4.17a}
$$

$$
= \|\vec{b}\|^2 - 2\sum_{i=1}^{N} w_i\hat{n}_i + 2\sum_{i=1}^{N}\sum_{j>i}\mu_{ij}\hat{n}_i\hat{n}_j \tag{4.17b}
$$

$$
\sim -2\sum_{i=1}^{N} w_i\hat{n}_i + 2\sum_{i=1}^{N}\sum_{j>i}\mu_{ij}\hat{n}_i\hat{n}_j \tag{4.17c}
$$

$$
\hat{H}_{\mathrm{BIP2}} = -\sum_{i=1}^{N} c_i\hat{n}_i, \tag{4.17d}
$$

where $w_i \equiv (S^T S)_{ii} - (S \cdot \vec{b})_i$, and $\mu \equiv S^T S - \mathrm{diag}(S^T S)$ (where S^T is the transpose of S and $\mathrm{diag}(S^T S)$ is the diagonal matrix with the same diagonal elements of $S^T S$). The total cost Hamiltonian $\hat{H}_{\mathrm{BIP}}$ of the **BIP** problem is the sum of $\hat{H}_{\mathrm{BIP1}}$ and $\hat{H}_{\mathrm{BIP2}}$, which is represented in **QUBO** form (Eqs.(4.18)), similar to the max cut problem:

$$
\hat{H}_{\mathrm{BIP}} = \hat{H}_{\mathrm{BIP1}} + \hat{H}_{\mathrm{BIP2}} \tag{4.18a}
$$

$$
= -\sum_{i=1}^{N}(c_i + 2w_i)\hat{n}_i + 2\sum_{i=1}^{N}\sum_{j>i}\mu_{ij}\hat{n}_i\hat{n}_j. \tag{4.18b}
$$

Similar to Subsec. 4.2.4, the BIP problem can be converted into an MIS problem corresponding to the QUBO formula Eq. (4.18b) [101].

4.2.6 Number Partitioning / Undirected Hamiltonian Cycle to MIS

In this subsection, among other NP-complete problems introduced in Subsec. 4.1.7, the MIS reduction for the **Number Partitioning** and the **Undirected Hamilton Cycle** problems which are not dual to the **MIS** or **Graph Coloring** problem will be discussed. As mentioned in Subsec. 4.1.7, the clique and clique cover prolems of a graph G is dual to the independent set and graph coloring of its complement graph $\overline{G}$, respectively.

Number Partitioning to MIS

The **Number Partitioning** problem is the determination problem to evaluate whether a set $S = \{s_1, s_2, \cdots, s_N\}$ of natural numbers is bipartitionable two subsets S_1 and S_2 whose total sums of elements are same. Thus, the cost Hamiltonian $\hat{H}_{\mathrm{Num-Part}}$ of the **Number Partitioning** problem is given as Eqs. (4.19):

$$
\hat{H}_{\mathrm{Num-Part}} = \left[\sum_{j=1}^{N} s_j\left(2\hat{n}_j - 1\right)\right]^2, \tag{4.19a}
$$

$$
= \sum_{j=1}^{N} s_j^2 + 2\sum_{j=1}^{N}\sum_{k>j} s_j s_k\left(4\hat{n}_j\hat{n}_k - 2\hat{n}_j - 2\hat{n}_k + 1\right), \tag{4.19b}
$$

$$
\sim -\sum_{j=1}^{N} s_j(M - s_j)\hat{n}_j + \sum_{j=1}^{N}\sum_{k>j}(2s_j s_k)\hat{n}_j\hat{n}_k, \tag{4.19c}
$$

where $M \equiv \sum_{j=1}^{N} s_j$ is the total sum of elements in S and $\hat{n}_j$ denotes whether s_j belongs to either S_1 or S_2 (i.e., if $\hat{n}_j = 1$, then $s_j \in S_1$). Similar to Subsecs. 4.2.4 and 4.2.5, the cost Hamiltonian $\hat{H}_{\mathrm{Num-Part}}$ is represented as a **QUBO** form, which leads to the conversion to **MIS** problem [101].

Undirected Hamiltonian Cycle to MIS

The **Undirected Hamiltonian Cycle** problem is the problem to find a Hamiltonian cycle which, for a given undirected graph $G(V, E)$, visits each node $v \in V$ exactly once and comes back to the start. So, the constraints of the **Undirected Hamiltonian Cycle** problem are given as followings:

UHC1. Each node $v_j \in V$ ($V = \{v_1, v_2, \cdots, v_N\}$) must be uniquely determined by its order $k \in \mathbb{Z}_N (= \{0, 1, \cdots, N - 1\})$ in the Hamiltonian cycle.

UHC2. Each ordering $k \in K (\equiv \{1, 2, \cdots, N\})$ must be uniquely determined for each node $v_j \in V$ ($V = \{v_1, v_2, \cdots, v_N\}$) in the Hamiltonian cycle.

UHC3. Two nodes whose order is k and $(k + 1)$ must be connected by an edge $e \in E$.

Here, the constraints **UHC1** and **UHC2** denote that for each ordering $k, l \in K$, different nodes $v, w \in V$ must be uniquely assigned, respectively, and **UHC3** enforces that no unedged nodes $u, v \in V$ (i.e., $(u, v) \notin E$) must be assigned to ordering $k, (k + 1) \in K$.

Thus, the cost Hamiltonians $\hat{H}_{\mathrm{UHC1}}$, $\hat{H}_{\mathrm{UHC2}}$ and $\hat{H}_{\mathrm{UHC3}}$ responsible for these constraints **UHC1**, **UHC2** and **UHC3** are given as Eqs. (4.20):

$$\hat{H}_{\mathrm{UHC1}} = \sum_{k \in \mathbb{Z}_N} \left[U \sum_{v \in V} \sum_{w \in V \setminus \{v\}} \hat{n}_{v,k} \hat{n}_{w,k} - \Delta \sum_{v \in V} \hat{n}_{v,k} \right] \tag{4.20a}$$

$$\hat{H}_{\mathrm{UHC2}} = \sum_{v \in V} \left[U \sum_{k \in \mathbb{Z}_N} \sum_{l > j} \hat{n}_{v,k} \hat{n}_{v,l} - \Delta \sum_{k \in \mathbb{Z}_N} \hat{n}_{v,k} \right] \tag{4.20b}$$

$$\hat{H}_{\mathrm{UHC3}} = U \sum_{k \in \mathbb{Z}_N} \sum_{(u,v) \notin E} \hat{n}_{u,k} \hat{n}_{v,k+1} \tag{4.20c}$$

where $\hat{n}_{v,k}$ denotes whether the pair (v, k) of the node $v \in V$ and the ordering $k \in \mathbb{Z}_N$ is selected (i.e., $\hat{n}_{v,k} = 1$, when (v, k) is chosen).

4.3 Quantum Programming of Satisfiability Instances

Of particular relevance in the context of the present chapter, the 3-SAT problem is reducible to the maximum independent set (MIS) problem, which is also the NP-complete problem [97, 98], and the MIS problem can be physically implemented with Rydberg atoms [19, 69]. So, we introduce a quantum algorithm to formulate the 3-SAT instance with a Rydberg atom system in this chapter, by formulating a quantum experiment to obtain the MIS solution of the Rydberg-atom graph programmed to algorithmically determine a given 3-SAT instance, i.e., to evaluate the satisfiability of the 3-SAT instance experimentally.

4.3.1 3-SAT Reduction to Maximum Independent Set Problems

Instances of 3-SAT problem are transformed into MIS instances via the mathematical reduction described in Subsec. 4.2.1. This reduction of 3-SAT instances to MIS instances maps the clauses consisting of two-literals and three-literals in Eq. (4.2b) to dimers and trimers, respectively, and literal-negation pairs to inter-clause edges. Ultimately, such an MIS graph G_M encodes the 3-SAT problem as a Rydberg atom array, an assembly of Rydberg dimers and trimers representing each clause, and Rydberg quantum wires with auxiliary atoms.

Two-Clause 3-SAT Instance
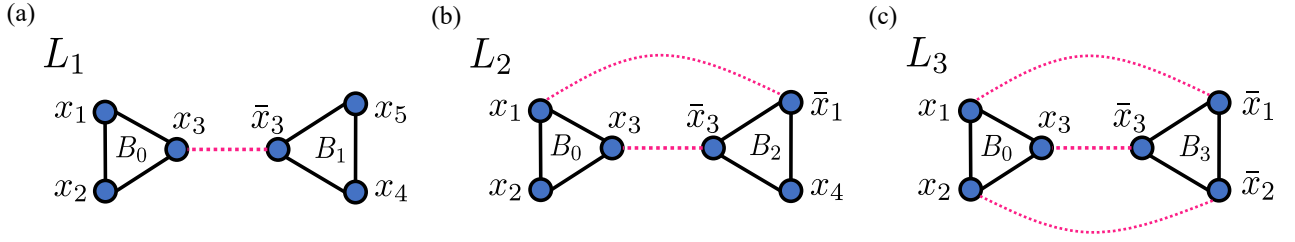
Figure 4.5: (a) MIS graph L_1 reduced from the 3-SAT instance Φ_1 in Eqs. (4.21), (b) L_2 from Φ_2, and (c) L_3 from Φ_3, where vertices represent literals ($x_1, \cdots, x_5$ and their negations), solid edges intra-clause logics, and dotted edges the inter-clause logics (between literals and their negations).

Figs. 4.5 show examples of MIS graphs for the two-clause 3-SAT instances, denoted by G_Ms, from the reduction algorithm in Subsec. 4.2.1. The first graph in Fig. 4.5 (a), L_1, is the graph for the 3-SAT instance, given as follows:

$$\Phi_1(x_1, x_2, x_3, x_4, x_5) = B_0 \wedge B_1 \tag{4.21a}$$

$$B_0 = x_1 \vee x_2 \vee x_3 \tag{4.21b}$$

$$B_1 = \bar{x}_3 \vee x_4 \vee x_5. \tag{4.21c}$$

where clauses with three literals are mapped to trimers (solid edges) and literal-negation pairs are mapped to inter-clause edges (dotted edges). In a similar way, for $B_2 = \bar{x}_1 \vee \bar{x}_3 \vee x_4$ and $B_3 = \bar{x}_1 \vee \bar{x}_2 \vee \bar{x}_3$, we define two more MIS graphs L_2 and L_3 for $\Phi_2 = B_0 \wedge B_2$ and $\Phi_3 = B_0 \wedge B_3$, respectively, as shown in Figs. 4.5 (b) and (c).

Three-Clause 3-SAT Instance

Figs. 4.6 show the MIS graphs of three-clause 3-SAT instances obtained by the reduction algorithm used in the two-clause cases. G_1 in Fig. 4.6 (a) is the graph for the three-clause 3-SAT instance given
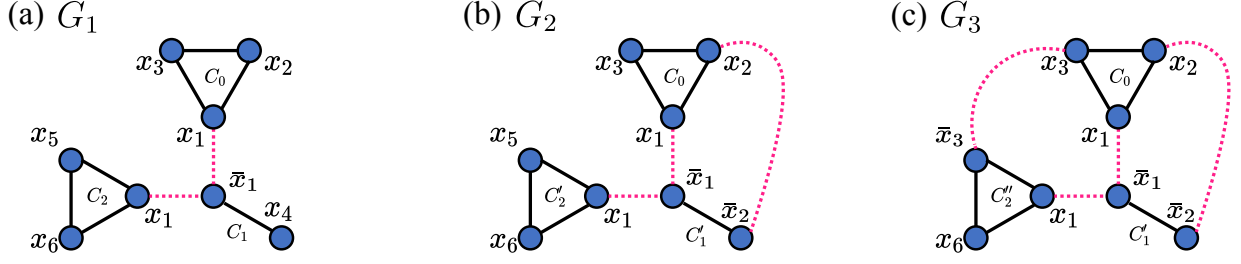
Figure 4.6: (a) MIS graph G_1 reduced from the 3-SAT instance Ψ_1 in Eqs. (4.22), (b) G_2 from Ψ_2, and (c) G_3 from Ψ_3, where vertices represent literals ($x_1, \cdots, x_6$ and their negations), solid edges intra-clause logics, and dashed edges the inter-clause logics (between literals and their negations). The figure is reused from the reference [72], APS.

by Eqs. (4.22):

$$\Psi_1(x_1, x_2, x_3, x_4, x_5, x_6) = C_0 \wedge C_1 \wedge C_2 \tag{4.22a}$$

$$C_0 = x_1 \vee x_2 \vee x_3 \tag{4.22b}$$

$$C_1 = \bar{x}_1 \vee x_4 \tag{4.22c}$$

$$C_2 = x_1 \vee x_5 \vee x_6 \tag{4.22d}$$

where, analogous to Eqs. (4.21), clauses with two or three literals are mapped to dimers or trimers (solid edges), respectively, and literal-negation pairs are mapped to inter-clause edges (dotted lines). Similarly, with $C_1' = \bar{x}_1 \vee \bar{x}_2$ and $C_2' = x_1 \vee \bar{x}_3 \vee x_6$, we can define two more MIS graphs G_2 and G_3 as shown in Figs. 4.6 (b) and (c) for $\Psi_2 = C_0 \wedge C_1' \wedge C_2$ and $\Psi_3 = C_0 \wedge C_1' \wedge C_2'$, respectively.

4.3.2 Experimental Procedure

Quantum computing of the 3-SAT instance starts from the single-atom array G_M prepared with the initial state $|\psi_{G_M}(t = 0)\rangle = |0\rangle^{\otimes |G_M|}$ ($|0\rangle \equiv |g\rangle$ is the ground state), resulting from the 3-SAT reduction to MIS (mentioned in Subsec. 4.3.1). And the Hamiltonian of the Rydberg atom array G_M is given (with $\hbar = 1$ unit) by Eq. (2.25) and Eq. (2.26) is as follows:

$$\hat{H}_{G_M}(t) = \sum_{(j,k) \in E(G_M)} U \hat{n}_j \hat{n}_k - \sum_{j \in V(G_M)} \left(\Delta(t) \hat{n}_j - \frac{\Omega(t)}{2} \hat{\sigma}_x^{(j)} \right), \tag{4.23}$$

where U is the interaction between edged atoms, Ω and Δ are the Rabi frequency and detuning, and $\hat{n}_j \equiv |1\rangle \langle 1|$, $\hat{\sigma}_x^{(j)}$ are the occupation number and Pauli x-operator defined for the ground ($|0\rangle \equiv |g\rangle$) and Rydberg ($|1\rangle \equiv |R\rangle$) states of the j-th atom (see the Eq. (2.9)). And according to the constraint term $U \hat{n}_j \hat{n}_k$ ($U > 0$) and the promoting term $-\Delta \hat{n}_j$ ($\Delta > 0$) from the MIS definition (mentioned in Subsec. 2.2.3), in the limit $\Omega \to 0$, many-body ground states of $\hat{H}_{G_M}$ ($\to H_{\text{MIS}}(G_M)$ in the Eq. (2.25)) are MIS solutions of G_M [68, 69].

Hence, as shown in Fig. 4.7, the control Hamiltonian $\hat{H}_{G_M}(t)$ in Eq. (4.23), we adiabatically change the control Hamiltonian $\hat{H}_{G_M}(t)$ to $\hat{H}_{G_M}(t = t_f) = \hat{H}_{G_M}(\Omega \to 0, \Delta = \Delta_f > 0)$. In this process, $\Omega(t)$ and $\Delta(t)$ are varied in the following way using the Rydberg excitation laser system (Subsec. 2.3.2):

1. First stage ($0 < t < t_1$): $\Omega(0 < t < t_1)$ is swept linearly as $\Omega_0(t/t_1)$ and $\Delta(0 < t < t_1)$ is fixed as Δ_i.
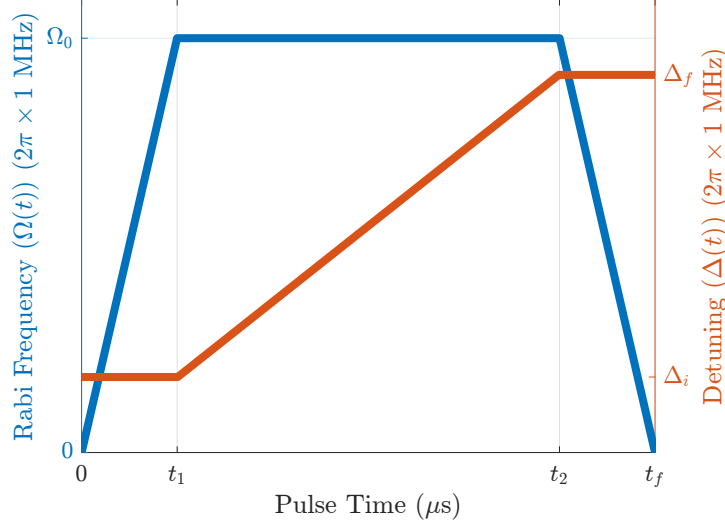
Figure 4.7: The Rabi frequency and detuning for the adiabatic process.

2. Second stage $(t_1 < t < t_2)$: $\Omega(t_1 < t < t_2) = \Omega_0$ is fixed and $\Delta(t_1 < t < t_2)$ is swept linearly from Δ_i to Δ_f.

3. Final stage $(t_2 < t < t_f)$: $\Omega(t_2 < t < t_f) = \Omega_0 \cdot [(t_f - t)/(t_f - t_2)]$ is swept linearly and $\Delta(t_2 < t < t_f) = \Delta_f$ is fixed.

The final state $|\psi_{G_M}(t = t_f)\rangle$ resulting from this adiabatic process is approximately the super-position of the many-body ground states of $H_{G_M}(\Omega \to 0, \Delta = \Delta_f > 0)$, and accordingly the final ground-state atom is detected by atomic qubit state measurement (Subsec. 2.3.3). To obtain the probability distribution $P_{G_M}(x) = |\langle x|\psi_{G_M}(t = t_f)\rangle|^2$ for all $2^{|G_M|}$ binary atom configurations $|x\rangle = |00 \cdots 0\rangle, |00 \cdots 1\rangle, \cdots, |11 \cdots 1\rangle$, M repeated measurements are performed.

Experimental Setup

The experimental setup for implementing this quantum programming is the Rydberg atom quantum machine described in Sec. 2.3 and reported elsewhere [19, 80, 81, 102]. The distance between all edged (i.e. nearest-neighbor) atoms is $d = 7.0$ μm, which is smaller than the Rydberg blockade distance $d_B = 9 - 10$ μm, and the van der Waals interaction between these edged atoms is $U = 2\pi \times 8.70$ MHz.

Experimental Condition (Two-Clause SAT)

First, we perform experimental test of Rydberg quantum programming of the 3-SAT instance for three two-clause 3-SAT instances Φ_1, Φ_2, and Φ_3: their corresponding graphs are L_1, L_2, and L_3 in Figs. 4.5 (a), (b), and (c), respectively, where each three-literal clause is an atomic trimer in a triangular configuration and the inter-clause logic (between a literal and its negation) is realized as an inter-clause edge (represented by a dashed line). For example, in Φ_1 in Fig. 4.5 (a), x_3 in B_0 and $\bar{x}_3$ in B_1 are edged in L_1.

The experimental graphs, L_1^{Exp}, L_2^{Exp}, and L_3^{Exp}, for the experimental implementation of L_1, L_2, and L_3 have been constructed as shown in Figs. 4.8 (a), (b) and (c), respectively. The nearest-neighbor

Figure 4.8: (a) Experimental graph L_1^{Exp}, (b) L_2^{Exp}, and (c) L_3^{Exp} of literal atoms $(x_1, \cdots, x_6)$ and quantum wire atoms $(a_1, \cdots, a_8)$.

Table 4.1: Atom positions in graphs L_1^{Exp}, L_2^{Exp}, and L_3^{Exp}

Graphs		Atom positions (x, y) (μm)		
	x_1:	(-9.56, -3.50)	x_2:	(-9.56, 3.50)
L_1^{Exp}	x_3:	(-3.50, 0.00)	$\bar{x}_3$:	(3.50, 0.00)
	x_4:	(9.56, 3.50)	x_5:	(9.56, -3.50)
	x_1:	(-9.56, -3.50)	x_2:	(-9.56, 3.50)
	x_3:	(-3.50, 0.00)	$\bar{x}_1$:	(9.56, -3.50)
L_2^{Exp}	x_4:	(9.56, 3.50)	$\bar{x}_3$:	(3.50, 0.00)
	a_1:	(-10.44, -10.44)	a_2:	(-3.50, -11.33)
	a_3:	(3.50, -11.33)	a_4:	(10.44, -10.44)
	x_1:	(-9.56, -3.50)	x_2:	(-9.56, 3.50)
	x_3:	(-3.50, 0.00)	$\bar{x}_1$:	(9.56, -3.50)
	$\bar{x}_2$:	(9.56, 3.50)	$\bar{x}_3$:	(3.50, 0.00)
L_3^{Exp}	a_1:	(-10.44, -10.44)	a_2:	(-3.50, -11.33)
	a_3:	(3.50, -11.33)	a_4:	(10.44, -10.44)
	a_5:	(-10.44, 10.44)	a_6:	(-3.50, 11.33)
	a_7:	(3.50, 11.33)	a_8:	(10.44, 10.44)

edges including "normal" edges (solid line edges) are implemented by the strong interaction of atoms at a distance d smaller than the Rydberg blockade distance $d_B = 9.00\mu$m, while physically distant inter-clause edges, such as x_1-$\bar{x}_1$ in L_2, x_1-$\bar{x}_1$ and x_2-$\bar{x}_2$ in L_3 use Rydberg quantum wires for implementation [19, 81]. In Fig. 4.8 (a), two atom trimers of B_0 (left) and B_1 (right) are closely placed for $L_1^{\text{Exp}} = L_1$, respectively, where atoms x_3 and $\bar{x}_3$ are at distance d. In Fig. 4.8 (b), the long edge between x_1 and $\bar{x}_1$ of L_2^{Exp} is implemented via the Rydberg quantum wire of the four auxiliary atoms denoted by $\{a_1, \cdots, a_4\}$. In Fig. 4.8 (c), the two long edges x_1-$\bar{x}_1$ and x_2-$\bar{x}_2$ in L_3^{Exp} are implemented by the two Rydberg quantum wires of the four auxiliary atoms in $\{a_1, \cdots, a_4\}$ and $\{a_5, \cdots, a_8\}$, respectively, which mediates a Rydberg blockade between two distant literal atoms [19, 103, 104]. The resulting atom positions are listed in Table 4.1. For the analysis of the experimental data, the Rydberg quantum wire compilation method [81] is used, which imposes the anti-ferromagnetic atom chain conditions $|a_1 a_2 a_3 a_4\rangle$ and $|a_5 a_6 a_7 a_8\rangle = |0101\rangle$ or $|1010\rangle$ on all the collected experimental data. The many-body ground states of the three graphs

Table 4.2: Many-body ground states of L_1^{Exp}, L_2^{Exp}, and L_3^{Exp} graphs

Graphs	State representation	Many-body ground states $\left\|L_{1,2,3}^{\mathrm{Exp}}\right\rangle$ of $\hat{H}_{L_{1,2,3}^{\mathrm{Exp}}}(\Omega \to 0)$ in their MIS phase
L_1^{Exp}	$\|x_1 x_2 x_3; \bar{x}_3 x_4 x_5\rangle$	$\frac{3}{10}\left(\|001;001\rangle + \|001;010\rangle + \|010;100\rangle + \|100;100\rangle\right)$ $+\frac{2}{5}\left(\|010;001\rangle + \|010;010\rangle + \|100;010\rangle + \|100;001\rangle\right)$
L_2^{Exp}	$\|a_1 a_2 a_3 a_4\rangle$ $\otimes \|x_1 x_2 x_3; \bar{x}_1 \bar{x}_3 x_4\rangle$	$\frac{1}{\sqrt{3}}\|0101\rangle \otimes \left[\frac{1}{\sqrt{6}}\left(\|010;010\rangle + \|100;001\rangle\right)\right.$ $\left.+\frac{1}{6}\left(\sqrt{15}\|010;001\rangle + \sqrt{7}\|001;001\rangle\right) + \frac{1}{\sqrt{18}}\|100;010\rangle\right]$ $+\frac{1}{\sqrt{3}}\|1010\rangle \otimes \left[\frac{1}{\sqrt{6}}\left(\|001;001\rangle + \|010;100\rangle\right)\right.$ $\left.+\frac{1}{6}\left(\sqrt{15}\|010;001\rangle + \sqrt{7}\|010;010\rangle\right) + \frac{1}{\sqrt{18}}\|001;100\rangle\right]$ $+\frac{1}{\sqrt{3}}\|1001\rangle \otimes \left[\frac{1}{\sqrt{2}}\|010;001\rangle + \frac{1}{2}\left(\|001;001\rangle + \|010;010\rangle\right)\right]$
L_3^{Exp}	$\|a_1 a_2 a_3 a_4\rangle \otimes \|a_5 a_6 a_7 a_8\rangle$ $\otimes \|x_1 x_2 x_3; \bar{x}_1 \bar{x}_2 \bar{x}_3\rangle$	$\sqrt{\frac{2}{14}}\|0101\rangle \otimes \|0101\rangle$ $\otimes \frac{1}{\sqrt{2}}\left(\|010;001\rangle + \|100;001\rangle\right)$ $+\sqrt{\frac{3}{14}}\|0101\rangle \otimes \|1010\rangle$ $\otimes \frac{1}{\sqrt{3}}\left(\|001;010\rangle + \|100;001\rangle + \|100;010\rangle\right)$ $+\sqrt{\frac{3}{14}}\|1010\rangle \otimes \|0101\rangle$ $\otimes \frac{1}{\sqrt{3}}\left(\|001;100\rangle + \|010;001\rangle + \|010;100\rangle\right)$ $+\sqrt{\frac{2}{14}}\|1010\rangle \otimes \|1010\rangle$ $\otimes \frac{1}{\sqrt{2}}\left(\|001;010\rangle + \|001;100\rangle\right)$ $+\frac{1}{\sqrt{14}}\|1001\rangle \otimes \|0101\rangle \otimes \|010;001\rangle$ $+\frac{1}{\sqrt{14}}\|1001\rangle \otimes \|1010\rangle \otimes \|001;010\rangle$ $+\frac{1}{\sqrt{14}}\|0101\rangle \otimes \|1001\rangle \otimes \|100;001\rangle$ $+\frac{1}{\sqrt{14}}\|1010\rangle \otimes \|1001\rangle \otimes \|001;100\rangle$

tested, L_1^{Exp}, L_2^{Exp}, and L_3^{Exp}, are presented in Table 4.2.

The parameter values used by the adiabatic process are as follows: Initial and final detunings $\Delta_i = 2\pi \times -3.5$ MHz and $\Delta_f = 2\pi \times 2.5$ MHz, total processing time $t_f = 1.73$ μs, sweep start and end time points $t_1 = t_f/6$ and $t_2 = 5t_f/6$, the two-photon Rabi frequency at peak $\Omega_0 = \Omega_{0i}\Omega_{i1}/2\Delta_m = 2\pi \times 1.92$ MHz (corresponding to the Rydberg blockade distance $r_B = 9.0$ μm), where $\Omega_{0i} = 2\pi \times 114$ MHz and $\Omega_{i1} = 2\pi \times 22.2$ MHz are the one-photon Rabi frequencies of the $\|0\rangle - \|i\rangle$ and $\|i\rangle - \|1\rangle$ transitions, respectively, and $\Delta_m = 2\pi \times 660$ MHz represents intermediate detuning. This adiabatic process was repeated for $M = 537$, 4026, and 3379 iterations for the one-, two- and three-wire graphs L_1^{Exp}, L_2^{Exp}, and L_3^{Exp}, respectively, and the results were measured.

Experimental Condition (Three-Clause SAT)

Additionally, we perform experimental tests of Rydberg quantum programming on three instances of 3-SAT, Ψ_1, Ψ_2, and Ψ_3, which are three instances of three-clause 3-SAT with a two-literal clause added: G_1, G_2, and G_3 in Figs. 4.6 (a), (b), and (c), respectively, with the addition of an atomic dimer for the two-literal clause.
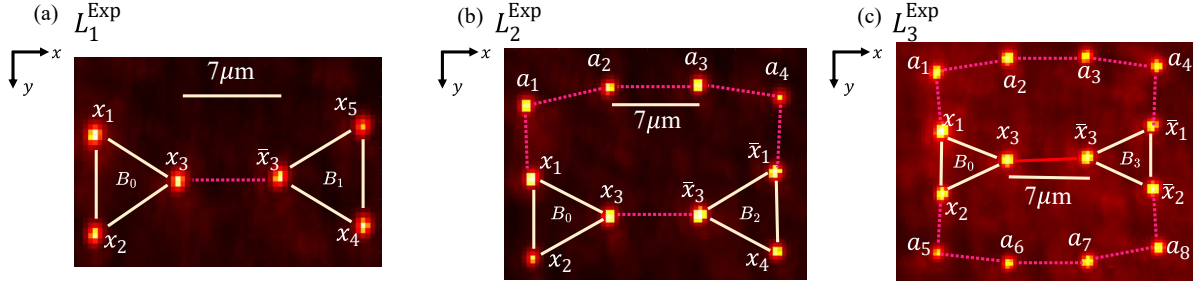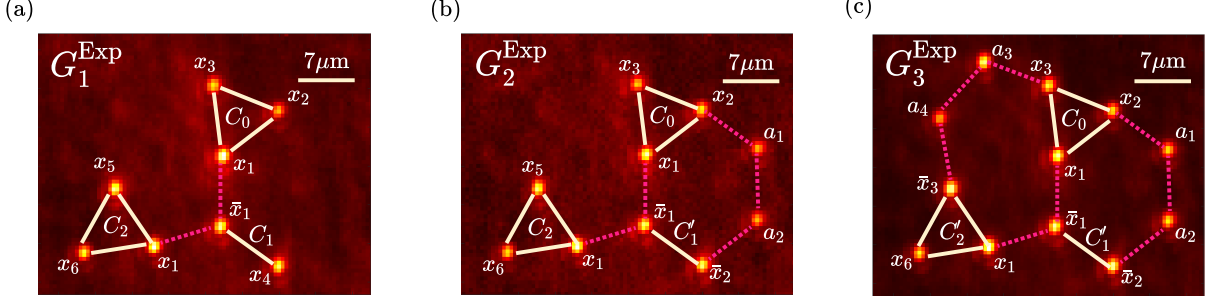

Figure 4.9: (a) Experimental graph G_1^{Exp}, (b) G_2^{Exp}, and (c) G_3^{Exp} of literal atoms $(x_1, \cdots, x_6)$ and quantum wire atoms $(a_1, \cdots, a_4)$. The figure is reused from the reference [72], APS.

Table 4.3: Atom positions of G_1^{Exp}, G_2^{Exp}, G_3^{Exp}, and G_1^{Alt}. The table is reused from the reference [72], APS.

Graphs		Atom positions (x, y, z) (μm)		
G_1^{Exp}	x_1:	(-1.51, -0.97, 0)	x_2:	(4.01, -5.28, 0)
	x_3:	(-2.49, -7.90, 0)	$\bar{x}_1$:	(-1.70, 6.03, 0)
	x_4:	(4.09, 9.97, 0)	x_1:	(-8.47, 7.80, 0)
	x_5:	(-12.35, 1.97, 0)	x_6:	(-15.46, 8.24, 0)
G_2^{Exp}	x_1:	(-1.51, -0.97, 0)	x_2:	(4.01, -5.28, 0)
	x_3:	(-2.49, -7.90, 0)	$\bar{x}_1$:	(-1.50, 6.03, 0)
	$\bar{x}_2$:	(4.09, 9.97, 0)	x_1:	(-8.47, 7.80, 0)
	x_5:	(-12.35, 1.97, 0)	x_6:	(-15.46, 8.24, 0)
	a_1:	(9.69, -1.20, 0)	a_2:	(9.71, 5.80, 0)
G_3^{Exp}	x_1:	(-1.51, -0.97, 0)	x_2:	(4.01, -5.28, 0)
	x_3:	(-2.49, -7.90, 0)	$\bar{x}_1$:	(-1.50, 6.03, 0)
	$\bar{x}_2$:	(4.09, 9.97, 0)	x_1:	(-8.47, 7.80, 0)
	$\bar{x}_3$:	(-12.35, 1.97, 0)	x_6:	(-15.46, 8.24, 0)
	a_1:	(9.69, -1.20, 0)	a_2:	(9.71, 5.80, 0)
	a_3:	(-9.05, -10.36, 0)	a_4:	(-13.50, -4.93, 0)
G_1^{Alt}	x_1:	(-7.20, 0.03, 0)	x_2:	(-13.44, 3.60, 0)
	x_3:	(-13.44, -3.60, 0)	$\bar{x}_1$:	(0, 0, 0)
	x_4:	(3.60, 0, 6.24)	x_1:	(3.60, 0, -6.24)
	x_5:	(3.60, 0, -13.44)	x_6:	(9.84, 0, -9.84)

In the same way as in the case of Figs. 4.5 and Figs. 4.8, the MIS graphs G_1, G_2, and G_3 in Fig. 4.6 are physically implemented as the experimental graphs G_1^{Exp}, G_2^{Exp}, and G_3^{Exp} in Figs. 4.9: In Fig. 4.9 (a), for Ψ_1, the atomic trimers C_0 (top)-C_1 (bottom right) and C_1 (bottom right)-C_2 (bottom left) are placed close together so that atoms x_1 of C_0 (each of which is also in C_2) and $\bar{x}_1$ of C_1 are located at distance d. Thus, x_1 of C_0 and C_2 are edged by $\bar{x}_1$ of C_1. In Fig. 4.9 (b), the long edge between x_2 and $\bar{x}_2$ of G_2^{Exp} is implemented as a Rydberg quantum wire consisting of two auxiliary atoms denoted by $\{a_1, a_2\}$. Also, in Fig. 4.9 (c), the two long edges x_2-$\bar{x}_2$ and x_3-$\bar{x}_3$ of G_3^{Exp} are implemented as two Rydberg quantum wires with auxiliary atoms $\{a_1, a_2\}$ and $\{a_3, a_4\}$, respectively. The positions of the atoms in the experimental graphs G_1^{Exp}, G_2^{Exp}, and G_3^{Exp} in these Figs. 4.9 (a-c) are listed in Table 4.3, along with G_1^{Alt}, which will be discussed in Sec. 4.5, and are constructed using the following conditions in the two-dimensional (x, y) plane, which is the focal plane of the optical tweezer:

- Unwanted (unedged) interatomic interactions should be minimized such that the edged pairs of all atoms, including auxiliary atoms, are at an interatomic distance $d = 7.0$ μm, which is smaller than the Rydberg blockade distance $d_B = 10.0$ μm.

For these conditions, the following is how to optimize the two-dimensional position of atoms in the experimental graph:

1. Numerically find the locations of all atoms (literal and quantum wire atoms) in G_3^{Exp} that minimize the overlap integral F of the unit disk of all atoms with no edges while preserving the condition of atoms with edges.

2. Then, G_1^{Exp}, G_2^{Exp} are obtained as graph minors of G_3^{Exp}.

In this case, the overlap integral is defined as the following Eq. (4.24):

$$F = \pi \sum_{(i,j) \in E} \pi \int_{\frac{|\vec{r}_{ij}|}{2}}^{\frac{d}{2}} \left(\frac{d^2}{4} - r^2 \right) dr + \frac{\pi}{\sqrt{8}} \sum_{(i,j) \notin E} \int_{\frac{|\vec{r}_{ij}|}{2}}^{\frac{d}{\sqrt{2}}} \left(\frac{d^2}{2} - r^2 \right) dr \cdot \Theta(\sqrt{2}d - |\vec{r}_{ij}|), \qquad (4.24)$$

where $\vec{r}_{ij}$ is the displacement vector from the i-th atom to the j-th atom, $\Theta(x)$ is the Heaviside step function (1 for $x > 0$, 0 for $x < 0$), and the minimum allowable distance between un-edged atoms is set to $\sqrt{2}d$. The first term is the overlap volume of two unit spheres of edged atoms, which is minimized so that all pairs of edged atoms are as close as possible. The second term is the overlap of two unit spheres of radius $\sqrt{2}d$ of unedged atoms, which is minimized such that $|\vec{r}_{ij}| > \sqrt{2}d$ for all pairs of unedged atoms. And, the many-body ground states of these G_1^{Exp}, G_2^{Exp}, and G_3^{Exp} graphs are listed in Table 4.4, being represented in symmetric base states defined by

$$|S_1\rangle = \frac{1}{\sqrt{2}} \left(|001; 01; 100\rangle + |010; 01; 100\rangle \right), \qquad (4.25a)$$

$$|S_2\rangle = \frac{1}{\sqrt{2}} \left(|001; 01; 001\rangle + |001; 01; 010\rangle \right), \qquad (4.25b)$$

$$|S_3\rangle = \frac{1}{\sqrt{2}} \left(|001; 10; 001\rangle + |001; 10; 010\rangle \right), \qquad (4.25c)$$

$$|S_4\rangle = \frac{1}{\sqrt{2}} \left(|010; 01; 001\rangle + |010; 01; 010\rangle \right), \qquad (4.25d)$$

$$|S_5\rangle = \frac{1}{\sqrt{2}} \left(|001; 10; 001\rangle + |001; 10; 010\rangle \right), \qquad (4.25e)$$

$$|S_6\rangle = \frac{1}{\sqrt{2}} \left(|100; 01; 001\rangle + |100; 01; 010\rangle \right). \qquad (4.25f)$$

Table 4.4: Many-body ground states of G_1^{Exp}, G_2^{Exp}, and G_3^{Exp} graphs. The table is reused from the reference [72], APS.

Graphs	State representation	Many-body ground states $\left\lvert G_{1,2,3}^{\text{Exp}} \right\rangle$ of $\hat{H}_{G_{1,2,3}^{\text{Exp}}}(\Omega \to 0)$ in theirs MIS phase
G_1^{Exp}	$\lvert x_1 x_2 x_3; \bar{x}_1 x_4; x_1 x_5 x_6 \rangle$	$\sqrt{\frac{49}{200}}\left(\lvert S_2\rangle + \lvert S_4\rangle\right) + \sqrt{\frac{9}{50}}\left(\lvert S_1\rangle + \lvert S_6\rangle\right)$ $+ \sqrt{\frac{3}{50}}\lvert 100;01;100\rangle + \sqrt{\frac{9}{200}}\left(\lvert S_3\rangle + \lvert S_5\rangle\right)$
G_2^{Exp}	$\lvert x_1 x_2 x_3; \bar{x}_1 \bar{x}_2; x_1 x_5 x_6 \rangle \otimes \lvert a_1 a_2 \rangle$	$\sqrt{\frac{1}{50}}\lvert S_3\rangle \otimes \left(\sqrt{\frac{18}{10}}\lvert 01\rangle + \sqrt{\frac{63}{10}}\lvert 10\rangle\right) + \sqrt{\frac{3}{500}}\lvert S_5\rangle$ $\otimes \lvert 01\rangle$ $+ \left(\sqrt{\frac{197}{500}}\lvert S_2\rangle + \sqrt{\frac{107}{500}}\lvert S_6\rangle\right)$ $\otimes \lvert 10\rangle$ $+ \left(\sqrt{\frac{131}{1000}}\lvert 001;01;100\rangle + \sqrt{\frac{93}{1000}}\lvert 100;01;100\rangle\right)$ $\otimes \lvert 10\rangle$
G_3^{Exp}	$\lvert x_1 x_2 x_3; \bar{x}_1 \bar{x}_2; x_1 \bar{x}_3 x_6 \rangle \otimes \lvert a_1 a_2 \rangle \otimes \lvert a_3 a_4 \rangle$	$\sqrt{\frac{1}{1000}}\lvert 001;10;001\rangle$ $\otimes \left(\sqrt{46}\lvert 01\rangle + \sqrt{53}\lvert 10\rangle\right) \otimes \lvert 01\rangle$ $+ \sqrt{\frac{46}{1000}}\lvert 010;10;001\rangle \otimes \lvert 01\rangle \otimes \left(\lvert 01\rangle + \lvert 10\rangle\right)$ $+ \sqrt{\frac{17}{1000}}\lvert 010;10;010\rangle \otimes \lvert 01\rangle \otimes \lvert 10\rangle$ $+ \left(\sqrt{\frac{121}{1000}}\lvert 001;01;001\rangle + \sqrt{\frac{65}{1000}}\lvert 001;01;100\rangle\right)$ $\otimes \lvert 10\rangle \otimes \lvert 01\rangle$ $+ \sqrt{\frac{46}{1000}}\lvert 100;01;010\rangle \otimes \lvert 10\rangle \otimes \lvert 10\rangle$ $+ \left(\sqrt{\frac{4}{25}}\lvert 100;01;001\rangle + \sqrt{\frac{3}{25}}\lvert 100;01;100\rangle\right)$ $\otimes \lvert 10\rangle \otimes \left(\lvert 01\rangle + \lvert 10\rangle\right)$

For the experimental preparation of the three instances of the three-clause 3-SAT thus prepared, the Δ/Ω_0 - U/Ω_0 phase diagrams of the experimental graphs G_1^{Exp}, G_2^{Exp}, and G_3^{Exp}, shown in Figs. 4.10 (a), (b), and (c), respectively, are divided into nine partitions according to the number of excited literal atoms:

- Partition I ($\Delta < 0$): This is the domain where all literal atoms are in the ground state.

- Partitions II and III: Smaller segments squeezed between I and IV, where only one and two literal atoms are excited, respectively.

- Partition IV: The domain where three literal atoms are excited, which is targeted for MIS solution. This domain is $0.01U < \Delta < 0.99U$ for G_1^{Exp}, $0.05U < \Delta < 0.98U$ for G_2^{Exp}, and $0.03U < \Delta < 0.95U$ for G_3^{Exp}.

- Partitions V-VIII: Regions where 4, 5, 6, and 7 atoms are excited, respectively.

- Partition IX: All literal atoms are excited.

Therefore, we set $(U/\Omega_0, \Delta/\Omega_0) = (8.70, 5)$, denoted by the diamond in the Partition IV, as the optimal experimental point. Then, the quantum adiabatic control path based on the $\Omega - \Delta$ phase diagram [105,
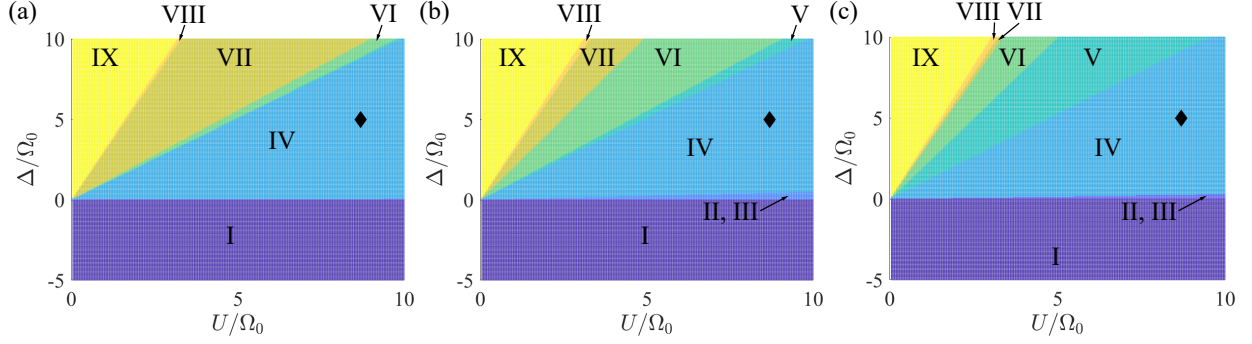
Figure 4.10: The Δ/Ω_0 - U/Ω_0 phase diagrams of 3-SAT instances with $N_C = 3$: (a) G_1, (b) G_2, (c) G_3.; Diamond point: Experimental condition $(U/\Omega_0, \Delta/\Omega_0) = (8.70, 5.0)$ for MIS solution, that is, each clause has only one MIS element and all clauses are excited.; There are nine partitions I-IX by the number of excited literal atoms. I: all literal atoms in ground state, II, III: only one or two literal atom excited respectively, IV: three literal atoms excited state which are targetted for MIS solution, V-VIII: four, five, six or seven atoms excited state respectively, IX: all literal atoms excited state
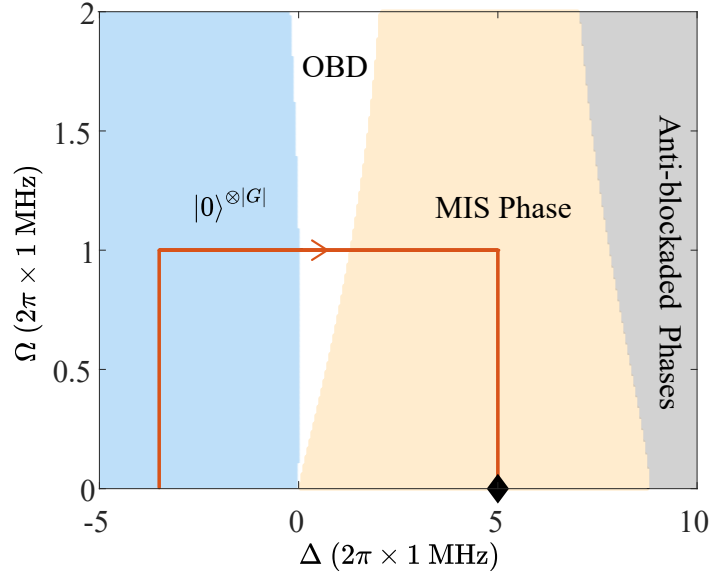
Figure 4.11: (a) Ω-Δ Phase diagram of $\hat{H}(G_1^{\mathrm{Exp}})$ with the control path is shown with an arrow from the paramagentic phas via order-by-disoder (OBD) to the MIS phase. The phase diagrams of $\hat{H}(G_{2,3}^{\mathrm{Exp}})$ are similar. The figure is reused from the reference [72], APS.

106] in Fig. 4.11 was constructed by following the arrow in Fig. 4.11 to solve Eq. (4.23) from $\hat{H}_{G_M}(\Delta = -0.7\Delta_0, \Omega = 0)$ to $\hat{H}_{G_M}(\Delta = \Delta_0, \Omega = 0)$, and the control parameters are as follows: Initial and final detuning $\Delta_i = -0.7\Delta_0$ and $\Delta_f = \Delta_0$, total processing time $t_f = 2.88\ \mu$s, sweep start and end time points $t_1 = t_f/10$ and $t_2 = 9t_f/10$, and two-photon Rabi frequency at peak $\Omega_0 = \Omega_{0i}\Omega_{i1}/2\Delta_m = 2\pi \times 1$ MHz (corresponding to $r_B = 10.0\ \mu$m), where $\Omega_{0i} = 2\pi \times 93$ MHz and $\Omega_{i1} = 2\pi \times 14$ MHz, and $\Delta_m = 2\pi \times 660$ MHz.

After this adiabatic control, measure the resulting atomic qubit states to record the experimental

MIS solution. Repeat this procedure $M = 5235$, 5000, and 8000 iterations for the graphs G_1^{Exp}, G_2^{Exp}, and G_3^{Exp}, respectively, to obtain the probability distribution of all binary spin configurations of all atoms.

4.4 Experimental Results

4.4.1 Two-Clause SAT Instance

We experimented with the MIS version of the 3-SAT instances $\{\Phi_1, \Phi_2, \Phi_3\}$ shown in Figs. 4.5 (a-c), respectively. The probability distributions of the theoretical ground states (see Table 4.2) of the 3-SAT instances Φ_1, Φ_2 and Φ_3 are shown in Figs. 4.12 (a), (b), and (c), respectively. As shown in Figs. 4.8 (b) and (c), for Φ_2 and Φ_3, wire atoms are used to mediate the Rydberg blockade between distant literal-negation pair atoms because the atoms connected by the inter-clause edge are farther than the Rydberg blockade distance [19, 103, 104, 107, 108]. Accordingly, simulation results filtered to reflect only the anti-ferromagnetic wire atomic state and the blockade literal atomic state are shown in Figs. 4.12 (d), (e), and (f), respectively. The results of the literal atom experiments with a state preparation and measurement (SPAM) error ($P(1|0) = 0.015$ and $P(0|1) = 0.1$), mitigated by the maximum-likelihood method [109], are shown in Figs. 4.12 (g), (h), and (i), respectively. In Figs. 4.12 (g-i), the orange bars are the probabilities of the literal atom solution state, the light navy bars are the probabilities of the other literal atom states, and the x- and y-axes represent the microstates of the literal atoms in each clause:

1. Φ_1 (L_1^{Exp} in Fig. 4.12 (g)):

   (a) Literal atomic solution state: $|x_1, x_2, x_3; \bar{x}_3, x_4, x_5\rangle = |010; 100\rangle, |010; 010\rangle, |010; 001\rangle, |100; 100\rangle, |100; 010\rangle, |100; 001\rangle, |001; 010\rangle$ and $|001; 001\rangle$.

   (b) The highest peak is $|x_1, x_2, x_3; \bar{x}_3, x_4, x_5\rangle = |010; 010\rangle$ and the second highest peak is $|001; 010\rangle$.

2. Φ_2 (L_2^{Exp} in Fig. 4.12 (h)):

   (a) Literal atomic solution state: $|x_1, x_2, x_3; \bar{x}_1, \bar{x}_3, x_4\rangle = |010; 010\rangle, |010; 001\rangle, |010; 100\rangle, |100; 010\rangle, |100; 001\rangle, |001; 001\rangle$ and $|001; 100\rangle$.

   (b) The highest peak is $|x_1, x_2, x_3; \bar{x}_1, \bar{x}_3, x_4\rangle = |010; 001\rangle$ and the second highest peak is $|001; 001\rangle$.

3. Φ_3 (L_3^{Exp} in Fig. 4.12 (i)):

   (a) Literal atomic solution state: $|x_1, x_2, x_3; \bar{x}_1, \bar{x}_2, \bar{x}_3\rangle = |010; 001\rangle, |010; 100\rangle, |100; 001\rangle, |100; 010\rangle, |001; 010\rangle$ and $|001; 100\rangle$.

   (b) The highest peak is $|x_1, x_2, x_3; \bar{x}_1, \bar{x}_2, \bar{x}_3\rangle = |001; 010\rangle$ and the second highest peak is $|010; 001\rangle$.

The **SAT** problem is the decision problem that evaluates satiability, i.e., the existence of a solution for which the logical expression is true, and the **MIS** reduction of the SAT instance evaluates the satiability of the SAT instance by observing whether there is a MIS element in each dimer or trimer. Therefore, to evaluate the solution probability summation that indicates the satiability of the 3-SAT instance in the 3-SAT experiment, in Figs. 4.12, we filter to account for only the anti-ferromagnetic wire atomic state and the blockade literal atomic state with the following conditions:
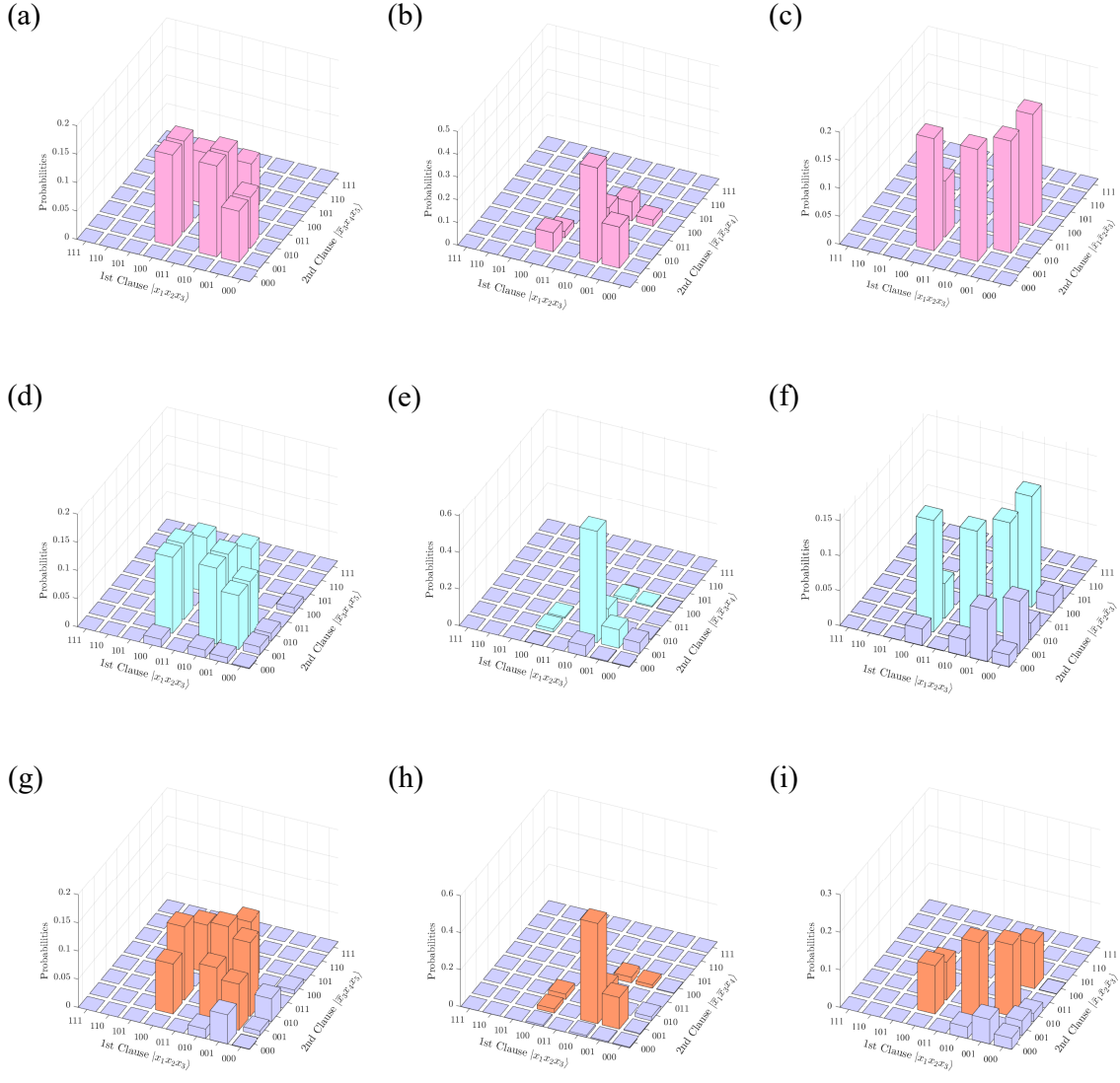
Figure 4.12: (a)-(c) Theoretical microstates probabilities from Table 4.2; (d)-(f) Simulation data of the microstates probabilities; (g)-(i) Experimental data of the microstates with anti-ferromagnetic states [81], except for anti-blockade literal atom basis (renormalized). (a),(d) and (g) are the results for the graph L_1, (b),(e) and (h) are for the graph L_2^{Exp}, (c), (f), and (i) are for the graph L_3^{Exp}. In (g)-(i), state preparation and measurement errors $P(1 \mid 0) = 0.015$ and $P(0 \mid 1)=0.1$ are considered by the maximum likelihood method [109].

1. First, we discard any anti-blockade state in which two or more literal atoms within a single clause are excited to the $|1\rangle$ state from the population.

2. Then, we also rule out inter-clause anti-blockade states (e.g., $|x_1, \bar{x}_1\rangle = |11\rangle$) from the population.

3. Finally, we only count the anti-ferromagnetic wire atomic states $|a_1, a_2, a_3, a_4\rangle$, $|a_5, a_6, a_7, a_8\rangle = |0101\rangle$, $|1010\rangle$ by the Rydberg quantum-wire compilation method [81].

The sum of the 3-SAT satisfaction probabilities evaluated by filtering with the above conditions are 87.1%, 95.0%, and 84.7% in graphs L_1^{Exp}, L_2^{Exp}, and L_3^{Exp}, respectively. It is estimated that the difference

between the simulation results and the experimental results is due to the laser beam pointing tilt problem, i.e., the direction of the laser beam pointing is slightly asymmetric with the literal atom arrangement, which causes the Rabi frequency of some atoms to be higher than the expected Rabi frequency value and the others to be lower. In the one-wire case (Fig. 4.8 (a)), the x_4 atom has a higher Rabi frequency than the x_5 atom; hence, the x_4 atom is more excited than the x_5 atom since the Rydberg blockade distance of each atom is unequal. In the three-wire case (Fig. 4.8 (c)), the x_1 and $\bar{x}_1$ atoms are subject to a lower Rabi frequency than the x_2 and $\bar{x}_2$ atoms. Therefore, the $|x_1, x_2, x_3; \bar{x}_1, \bar{x}_2, \bar{x}_3\rangle = |001; 010\rangle$ and $|010; 001\rangle$ states are measured more frequently than the $|001; 100\rangle$ and $|100; 001\rangle$ states (Fig. 4.12 (i)), in contrast to the ideal simulation results (Fig. 4.12 (f)).

4.4.2 Three-Clause SAT Instance

Figs. 4.13 (a), (b), and (c) are the experimental results for $G_M = G_1^{\mathrm{Exp}}, G_2^{\mathrm{Exp}}$, and G_3^{Exp}, respectively, where the x-axis shows the experimentally most-likely probabilities for all binary configurations of the literal atoms in the $|1\rangle$-state. Here, applying the filtering used in the case of the two-clause instances in Subsec. 4.4.1, all anti-blockade literal atom configurations (which are unlikely) are omitted for clarity and the maximum-likelihood probability calculation [109] assumes the experimentally measured SPAM error [82] $P(1|0) = 3.9\%$ and $P(0|1) = 7.9\%$. We also used the Rydberg quantum-wire compilation method [81], which imposes the anti-ferromagnetic wire atomic states $|a_1, a_2\rangle$ and $|a_3, a_4\rangle = |01\rangle$ or $|10\rangle$ among the acquired experimental data. In Figs. 4.13 (a-c), the orange bars are the 3-SAT solution states with one excited atom in each clause, and the gray bars are the non-solution states. For example, in Fig. 4.13 (a), for G_1^{Exp}, the maximum peak (i) of $|x_1, x_2, x_3; \bar{x}_1 x_4; x_1, x_5, x_6\rangle = |001; 01; 001\rangle$ is a 3-SAT solution, while the peak (ii) of $|001; 00; 001\rangle$ with two atoms excited in C_0 and C_2 but none in C_1 is a non-solution state. Similarly, in Figs. 4.13 (a-c), most of the dominant peaks are identified as 3-SAT solutions. For comparison, the insets in Figs. 4.13 (a-c) show the experimental error sources such as spontaneous decay of intermediate states (see Subsec. 2.1.3) and laser phase noise, which are taken into account by the Lindblad master equation (Eq. (2.23b)) and numerical simulations of the same physical process traced with the Lindblad master equation. The difference between simulation and experiment is mainly due to the distance error between the atom and the laser beam center, which results in a non-uniform Rabi frequency of the atom in Eq. (4.23). Numerical simulation is performed to compare the experimental results of the experimental graphs G_1^{Exp}, G_2^{Exp}, and G_3^{Exp}. To take into account the spontaneous decay from the intermediate state $|i\rangle$, the Lindblad master equation (Eq. (2.23b)), the intermediate detuning in the experiment and the individual dephasing rate at the Rabi frequency is estimated to be $\gamma = 2\pi \times 30$ kHz. The laser phase noise is then considered in the numerical calculation using the Monte-Carlo method, based on the fact that the spectral density of the measured noise is approximately 10^4 rad^2/Hz in the MHz range. We also take into account the inhomogeneity, where the Rabi frequency of an individual atom is 85 - 99.8% of the Rabi frequency at the laser beam center due to the finite diameter of 50 μm and the variation of the atom position ($\delta x = 0.1\mu$m, $\delta y = 0.1\mu$m, $\delta z = 0.6\mu$m) [19].

With the experimentally obtained probabilities shown in Figs. 4.13 (a-c), we can evaluate the satisfiability of the 3-SAT instances $\Psi_{1,2,3}$ based on whether they are solved correctly, i.e., whether the total probability of the MIS solution state is properly measured. In Fig. 4.13 (a), the sum of the probabilities in the orange bars for G_1^{Exp} is 81%, and consequently, the satisfiability of Ψ_1 is rated as probabilistically very high. Similarly, the satisfiability of Ψ_2 and Ψ_3 acquired from the experiments G_2^{Exp}, and G_3^{Exp} are
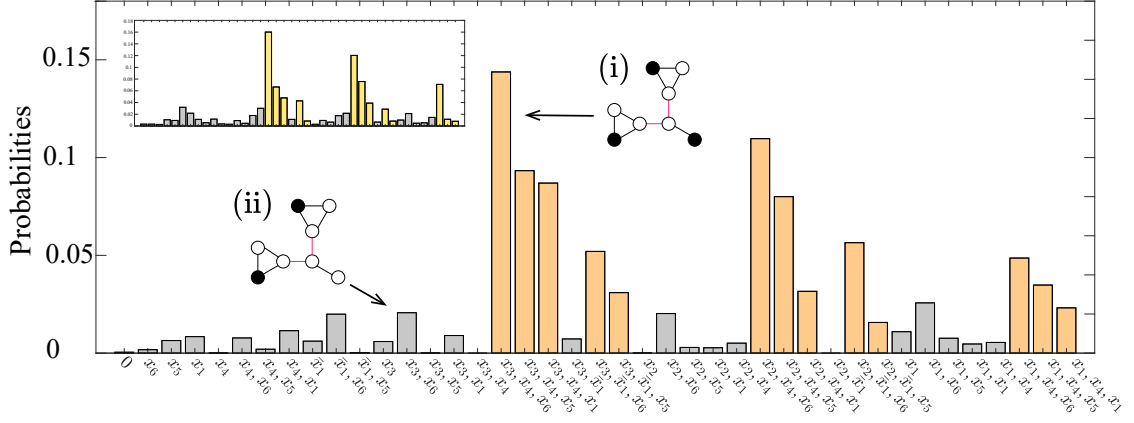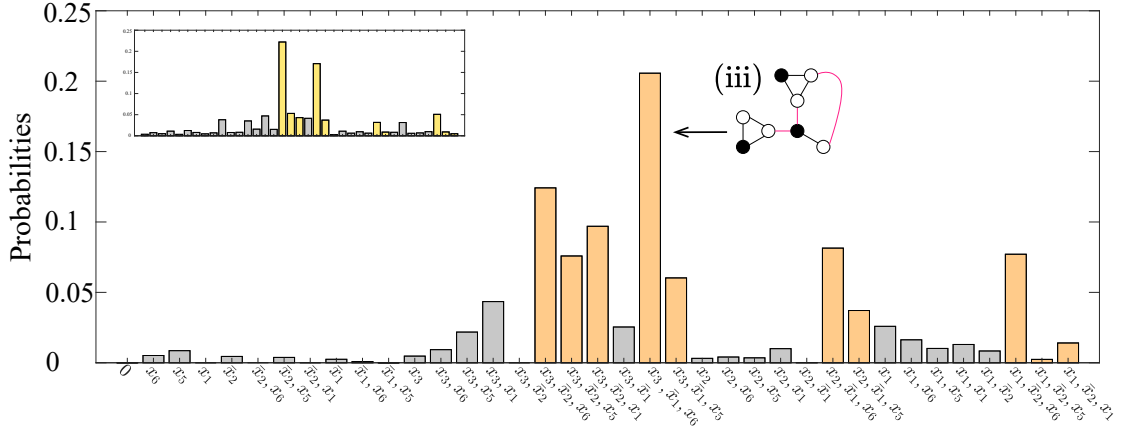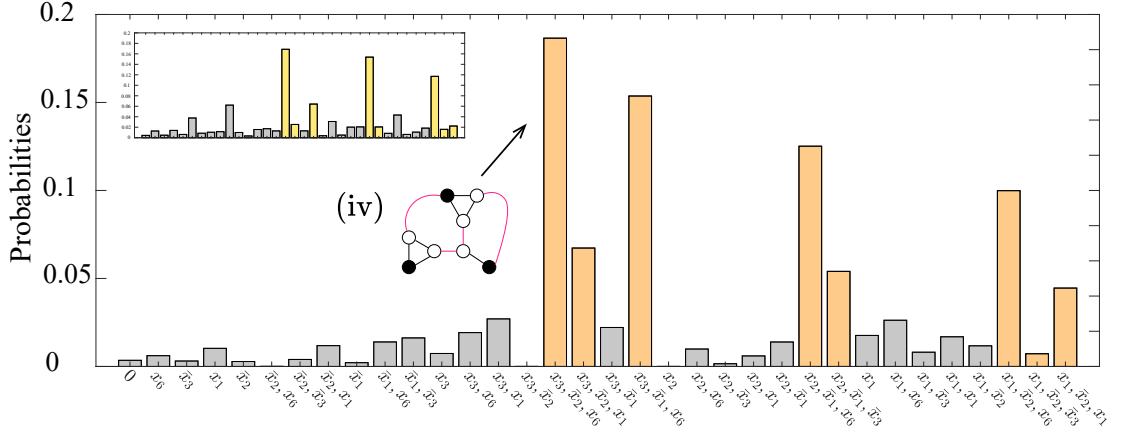
Figure 4.13: (a) Maximum likelihood probabilities of G_1^{Exp} experiments, where the x-axis denotes literal atoms in $|1\rangle$ in each binary configuration. (b) G_2^{Exp} experiments. (c) G_3^{Exp} experiments. For example, the peak (i) corresponds to $|x_1 x_2 x_3; x_4; x_5 x_6\rangle = |001; 1; 001\rangle$, (ii) $|001; 0; 001\rangle$, (iii) $|x_1 x_2 x_3; x_5 x_6\rangle = |001; 01\rangle$, and (iv) $|x_1 x_2 x_3; x_6\rangle = |001; 1\rangle$. Insets in (a-c) show numerical simulations with $\gamma = 30\ (2\pi)$ kHz of laser phase and dephasing noise taken into account. The figure is reused from the reference [72], APS.

evaluated as probability 78% and 74%, respectively.

4.5   Discussion

4.5.1   3D Atom allocation suggested for the Improvement of the Experimental Ground State
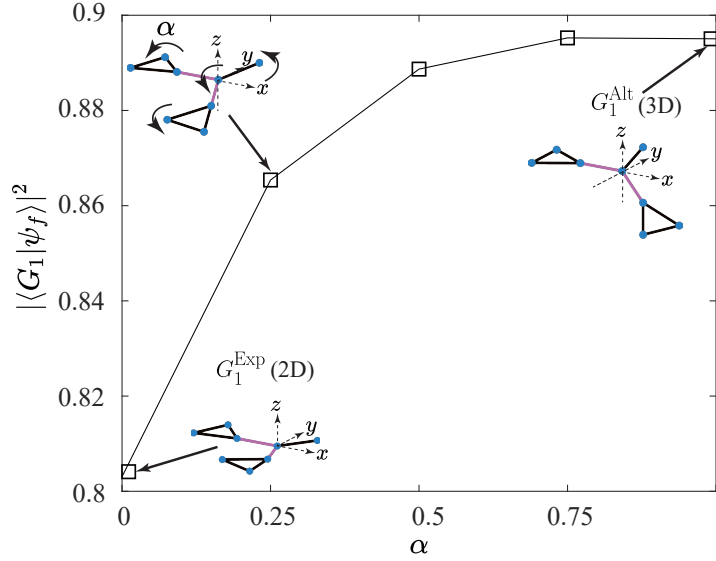
Figure 4.14: Ground state fidelity $|\langle G_1|\psi_f\rangle|^2$ according to the structural deformation from G_1^{Exp} to G_1^{Alt} with respect to a normalized rotation angle α. The figure is reused from the reference [72], APS.

The experiments in Subsection 4.4.2 can be improved by considering a three-dimensional Rydberg atom graph. The Hamiltonian $\hat{H}_{G_M}$ in Eq. (4.23) neglects long-range interactions as an approximation, so a three-dimensional MIS graph can be constructed for higher many-body ground state probabilities. In Fig. 4.14 computes the fidelity $|\langle G_1|\psi_f\rangle|^2$, where $|G_1\rangle$ is the analytic many-body ground state of $\hat{H}_{G_1^{\mathrm{Exp}}}(\Omega \to 0)$ (see Table 4.4 for details), and $|\psi_f\rangle$ is the final many-body state estimated numerically after quasi-adiabatic evolution under experimental conditions (without considering decoherence). For the experimental graph G_1^{Exp} in 2D, the fidelity is estimated to be 81% due to the contribution of long-range residual Rydberg interactions between atoms beyond the Rydberg blockade distance. The average strength of the residual interaction in the atomic arrangement for G_1^{Exp} is $\langle U_{\mathrm{res}}\rangle/2\pi = 0.64$ MHz, and its distribution is asymmetric. However, the structure of G_1^{Exp} can be transformed into an alternative graph G_1^{Alt} with a more symmetric geometry (see Table 4.3 for atom positions). As shown in Fig. 4.14, the structure transformation is performed by rotating the clauses C_0, C_1, and C_2 with respect to the edge at the literal atom $\bar{x}_1$ (the central atom), respectively, and these geometric changes are parameterized by the normalized rotation angle α ($\alpha = 0$ at G_1^{Exp}, and 1 at G_1^{Alt}). For the graph G_1^{Alt}, the average residual interaction strength is reduced to $\langle U_{\mathrm{res}}\rangle/2\pi = 0.40$ MHz, and the ground state fidelity $|\langle G_1|\psi_f\rangle|^2$ is improved to 90% after the same quasi-adiabatic evolution. Thus, the three-dimensional atom allocation has more degrees of freedom and thus is expected to improve the experimental performance, which is shown by the improvement in ground state fidelity $|\langle G_1|\psi_f\rangle|^2$ by the structural deformation with respect

to the normalized rotation angle α shown in Fig. 4.14.

4.5.2 Scalability: Total number of Atoms and Experimental time budget required for the Quantum programming of 3-SAT Instance

While all MIS graphs are in principle implementable in three-dimensional space via quantum wires [19], the scalability issue of the Rydberg atom approach to the 3-SAT instance is a worthwhile discussion. Hence, in this subsection, we address the following two scalability requirements for 3-SAT quantum programming: "Total number of atoms" and "Experimental time budget".

Total number of atoms required for 3-SAT instance
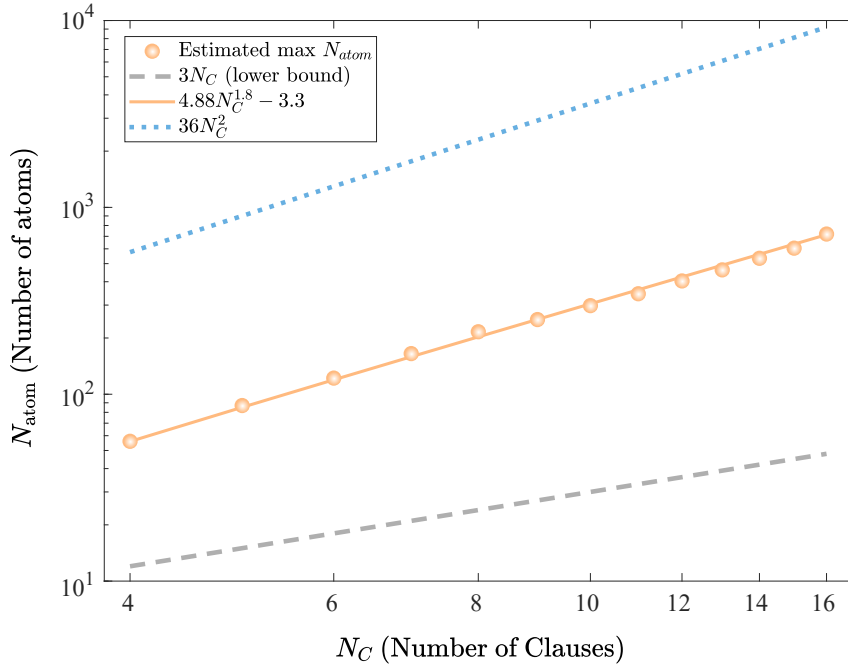
Figure 4.15: Estimation of the required number of atoms for MIS graphs mapped from 3-SAT instances. The lower bound is estimated from 3-SAT instances with no negation literal pairs and restricted to $3N_C$ (gray dashed line). The upper bound is calculated from 3-SAT instances with maximal negation literal pairs (orange dots) and scaled to $4.88N_C^{1.8}$ (solid line). It is also compared with the scaling result when the "crossing lattice" scheme is used (blue dotted line). The figure is adapted and reused from the reference [72], APS.

First, we estimate N_A, the total number of atoms required for general 3-SAT instances. For a Boolean function with N_C clauses, the lower bound on the total number of atoms required is $N_A \gtrsim 3N_C$, which is the case where there is no literal-negation pair (black dashed line in Fig. 4.15). The upper bound is the case of maximal literal-negation pairs, which is an MIS graph with maximal inter-clause interaction. To physically implement such a graph, auxiliary atoms are required to be used in either the "crossing lattice" scheme [110] or the "quantum wire" scheme [19], which have been recently proposed and experimentally

demonstrated, respectively. In the "crossing lattice" scheme, each node is transformed into a chain of atoms on a 2D surface, and the interactions between nodes are implemented by "crossing gadgets" consisting of up to 8 atoms. Thus, the upper bound on the number of atoms required is estimated to be $36N_C^2$ for a $3N_C$-node non-unit disk graph with arbitrary connectivity. For the "quantum wire" scheme, we numerically estimate the upper bound on the number of atoms for the implementation of MIS graphs under the assumption that all inter-clause interactions are implemented with quantum wires consisting of an average of four atoms. As a result, as shown in Fig. 4.15, the upper bound on the total number of atoms scales to $\sim 4.88N_C^{1.8}$, obtained from the fitting curve (solid line) of the calculated values, which is compared to the case of the "crossing lattice" scheme (blue dotted line). Thus, in the "quantum wire" scheme, the total number of atoms required is estimated as an upper bound by a scaling of $N_C^{1.8}$ for the largest literal-negation pairs and as a sublinear scaling of $O(N_C^{0.86\pm0.04})$ with respect to N_C for cases with a maximum degree of 6 in 3D [59, 60].

Next, we estimate the experimental time budget to tackle a large-scale 3-SAT problem. The probability of successfully obtaining the solutions of the 3-SAT problem after M experimental iterations is given as follows:

$$P_s(p, M) = \sum_{j=1}^{M} (1-p)^{j-1}p = 1 - (1-p)^M, \tag{4.26}$$

where p is the ground state probability of the corresponding MIS graph with N_A atoms. Based on the experimental scaling $p \sim 1.04^{-N_A}$ of a state-of-the-art experimental platform [68], the ground state probability of an MIS graph of the size $N_A = 400$ is estimated to be $p(N_A = 400) \sim 10^{-7}$. In this case, the number of iterations required to achieve, for example, $P_s > 20\%$ is given by $M > \log(1 - 0.2)/\log(1 - p)$, which is roughly $M \sim 10^6$ experimental iterations. Therefore, for the typical iteration rate of 2-3 Hz on current experimental platforms, an MIS graph experiment with $N_A = 400$, which can serve 3-SAT instances with approximately 12-140 clauses, would take 1 week.

4.6 Summary

We introduced Karp's NP-complete problems and examined theoretical methods for converting SAT, set packing, exact cover, max cut, and binary integer programming problems into maximum independent set (MIS) problem. Among these NP-complete problems, we propose the process of encoding and solving the 3-SAT instance, which is the task of determining the satisfiability of a Boolean expression, via Rydberg atom interaction, with theoretical and experimental results. The proposed Rydberg 3-SAT algorithm achieves this by formulating a general Boolean function using three types of building blocks (Rydberg atoms dimers, trimers, and quantum wires). Then, the satisfiability of the function is measured by experimental search for ground states within a structured Rydberg atom array. This implementation of the 3-SAT instance via Rydberg atom graphs has the potential to tackle a variety of decision-based computational instances involving NP-hard instances.

Chapter 5.   Rydberg Hybrid Quantum-Classical Programming

This chapter introduces hybrid quantum programming, called quantum-enhanced simulated annealing (QESA). While classical computers take an enormous amount of time to solve complex computational problems, quantum computing has the potential to solve them faster with its quantum properties [2, 111, 112]. However, current quantum systems are struggling to achieve both accuracy and qubit scalability. In order to achieve quantum supremacy, it is necessary to achieve scalability with low noise and reduce the iteration number of quantum adiabatic processes. To resolve this problem, we propose an approach that combines quantum experimental results with software programming to obtain high precision with short processing time. Among the various physical systems used in quantum computing [15, 113, 114, 115, 116], the Rydberg atom array has recently emerged as a promising platform due to its scalability, high qubit connectivity, and dynamic reconfigurability [69, 116, 117, 118, 119]. In particular, it offers outstanding features such as an intrinsic Hamiltonian that maps naturally to the maximum independent set (MIS) problem.

Here, we solve the MIS problem with the QESA method utilizing Rydberg atoms. We define the approximation ratio α as a metric and compare the processing time spent to reach α with the counterpart standalone simulated annealing (SA) method. The framework of adiabatic quantum computing (AQC) Rydberg atom array used as an experimental result is considered to be an efficient solving scheme in quantum computing, and many applications to MIS graphs have been documented [19, 60, 68, 70, 72, 73, 101, 120, 121, 122].

In addition, a hybrid quantum-classical algorithm that combines quantum experimental results with classical computing has recently been introduced [123]. In this chapter, in contrast to the previous papers, we identify the figure of merit that correlates to the performance of QESA and demonstrate the superiority of QESA over SA with a quantitative performance estimation.

And, we demonstrate the advantages of QESA using experimental results from adiabatic quantum computing (AQC) using Rydberg atom arrays (using previously reported datasets [120]) and quench evolution (QE) (using newly run experiments on a QuEra Aquila machine [125] accessed via the Amazon Bracket service), focusing on systems with a scale of about 100 atoms. We show the computational time advantage over conventional standalone simulated annealing (SA) and, in particular, present a new correlation between the computational time and Hamming distance for QESA. We show that QESA outperforms SA by utilizing a quantum experimentally optimized Hamming distance distribution, whereas SA starts with a non-optimized distribution. From these results, we examine the scalability of QESA in terms of the number of atoms and Hamming distance, and numerically estimate its potential to efficiently solve larger MIS problem within the constraint of available classical computational resources.

This chapter is based on a submitted paper: S. Jeong, J. Park, and J. Ahn, "Quantum-enhanced simulated annealing using Rydberg atoms," (2025) [124].

5.1 Approximation ratio

Before explaining the concept of QESA, we first introduce a metric for performance evaluation, called approximation ratio α (Eq. (5.1)). α is defined to compare the performance of standalone SA and QESA.

$$\alpha \equiv \frac{|\{i \in V | n_i = 1\}| - |\{(i,j) \in E | n_i n_j = 1\}|}{|\text{MIS}|}, \tag{5.1}$$

where $|\{i \in V | n_i = 1\}|$ counts the number of nodes in the independent set, $|\{(i,j) \in E | n_i n_j = 1\}|$ counts the number of edges connecting pairs of occupied nodes that violate the independence condition (see Subsec. 2.2.1), and $|\text{MIS}|$ denotes the size of the MIS of the graph. Thus, α considers two performance criteria:

(1) How close the total occupation number is to the MIS solution,

(2) How many edges violate the independence condition in the spin configuration.

This is a modification of the optimality gap [126, 127] used for comparison with ground energy.
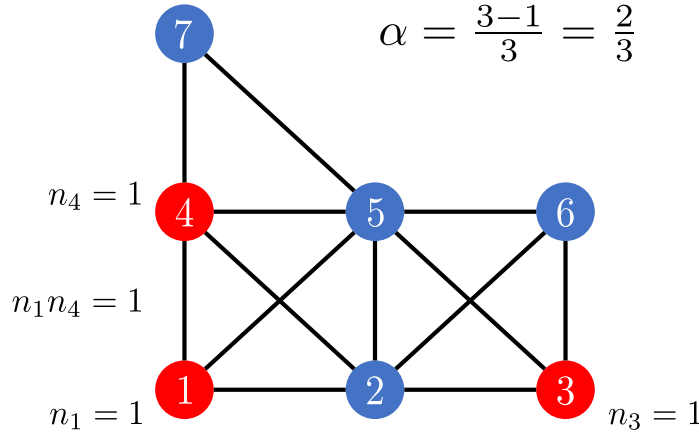
Figure 5.1: An easy illustration of calculating the approximation ratio α (Eq. (5.1)).

Fig. 5.1 is an easy example to illustrate α. It is a graph with an MIS solution size of 3, consisting of 7 vertices and 12 edges, with nodes $n_1, n_2, \cdots, n_7$. Suppose the nodes with the color "1" (red) in the obtained solution are n_1, n_3, and n_4 as shown in Fig. 5.1. In this case, the number of nodes is 3. However, the number of edges that violate the independence condition of the spin configuration due to simultaneously turning on to "1" at one edge (n_1, n_4) is 1. Therefore, the value of α in this case is 2/3. Even if the number of nodes lit to "1" is coincidentally the same as the MIS solution, such as in this case, the approximation ratio α has a lower value if there are edges that violate the independence condition. The approximation ratio α defined here is used as an evaluation metric for the Rydberg MIS result, SA, and QESA, which will be evaluated in the later sections.

5.2 Quantum-enhaced Simulated Annealing (QESA)

The routine of quantum-enhanced simulated annealing (QESA) is depicted in the QESA flow diagram of Fig. 5.2 and consists of four steps. First, in the Quantum Computing step, a Rydberg-atom experiment (AQC or QE) is performed to obtain quantum experimental result data for the MIS problem. The AQC and QE schemes are described later. In the Simulated Annealing (SA) Initialization step, the SA process is initialized using the quantum results. The quantum result data at this step contains errors. To mitigate these errors, the next step, Iterative Annealing, repeatedly runs the SA process using occupation flip and swap operations until a preset final temperature is reached. Finally, in the last step of QESA, we extract the resulting QESA solution after the SA process ends. Next, we explain the cost Hamiltonian H_{MIS} for the MIS problem:

$$H_{\mathrm{MIS}} = \sum_{j \in V} (-\Delta n_j) + \sum_{(j,k) \in E} U n_j n_k. \tag{5.2}$$

where the occupation number $n_j = 0, 1$ is a binary variable related to node $j \in V$. $n_j = 1$ indicates that node j belongs to the independent set, and $n_j = 0$ if it is excluded. The constants Δ and U are positive with $0 < \Delta < U$. The term Δn_j lowers the energy when $n_j = 1$, which promotes the inclusion of node j into the independent set. The term $U n_j n_k$ penalizes the inclusion of any two connected nodes j and k in the independent set by an edge, raising the energy to enforce the independence condition. Typically, the parameters are normalized by setting $\Delta = 1$. For specific graph structures, such as a king's graph (a graph representing the legal moves of a king on a chessboard), a value of $U = 11$ is chosen for a strong penalty of including adjacent nodes in the independent set [68]. $H_{\mathrm{MIS}}(s)$ in Eq. (5.2) is the energy for a spin configuration $s = (n_1, n_2, \cdots)$, which is minimized to $H_{\mathrm{MIS}}(s) = -|\mathrm{MIS}|$.

The quantum part of the QESA task utilizes adiabatic quantum computing (AQC) or quench evolution (QE). In AQC experiments, the quantum system is driven quasi-adiabatically, resulting in a gradual change in $\hat{H}_{\mathrm{Ryd}}$ in Eq. (2.26) over time. According to the quantum adiabatic theorem, if the evolution is slow enough, the system remains in the ground state of the time-varying Hamiltonian. By measuring the atomic state at the end of this evolution, a result corresponding to the low-energy state of the H_{MIS} can be obtained, which provides an approximate solution to the MIS problem. $\Omega(t)$ is typically chosen to be on the order of $2\pi \times 1$ MHz and $\Delta(t)$ is changed from $-2\pi \times 4.0$ MHz to $2\pi \times 2.0$ MHz over time. In this case, we use the Rydberg state $\left| n = 71, S_{1/2} \right\rangle$. For diagonally neighboring atoms, the interaction strength is $U(n = 71, r = 8.5\mu\mathrm{m}) = 2\pi \times 2.7$ MHz, and for laterally neighboring atoms, $U(n = 71, r = 6.0\mu\mathrm{m}) = 2\pi \times 21.7$ MHz.

Fig. 5.3 (a) shows an example of AQC experiment results for a 100-atom MIS graph with an 11×18 atom array. QESA incorporates Rydberg AQC into SA by leveraging experimental data from thousands of graphs with 60 to 115 atoms, as shown in Fig. 5.3 (a), where the black and red nodes represent the ground state and Rydberg state, respectively.

On the other hand, QE experiments are implemented on the QuEra Aquilla machine [125] by a single-atom Rabi frequency pulse with the following conditions: Rydberg state $\left| n = 70, S_{1/2} \right\rangle$ arranged so that the interaction strength is $U(n = 70, r = 7.5(1)\ \mu\mathrm{m}) = 2\pi \times 4.8(4)$ MHz for diagonally neighboring atoms and $U(n = 70, r = 5, 3(1)\ \mu\mathrm{m}) = 2\pi \times 39(4)$ MHz for laterally neighboring atoms, the resonant Rabi oscillation ($\Delta = 0$) with Rabi frequency rise/fall time $t_r = 50$ ns and $\Omega = 2\pi \times 1$ MHz, $t_Q = \pi/[\sqrt{\langle \deg(G) \rangle} \cdot \Omega]$, where $\langle \deg(G) \rangle$ is the average node degree in the graph G. This QE approach is inspired by the previously reported graph-degree dependence of the revival time for MIS state preparation in quasi-1D chain quantum quench [128]. Different from AQC, the QE method is expected to offer the
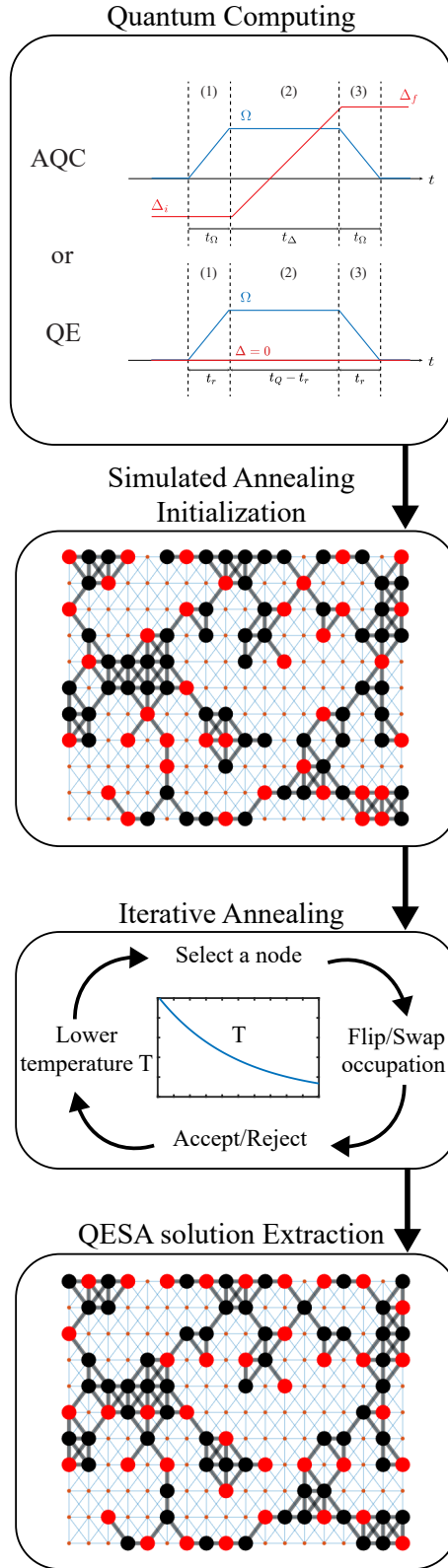
Figure 5.2: QESA flow diagram
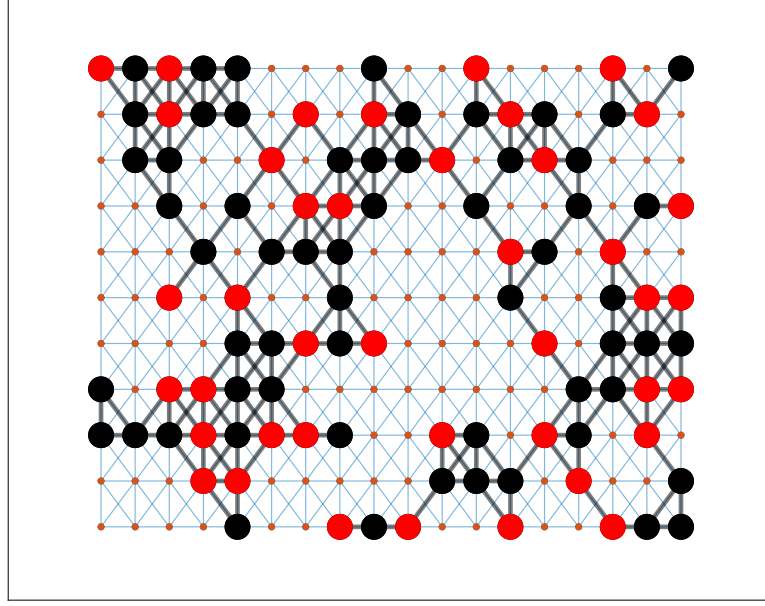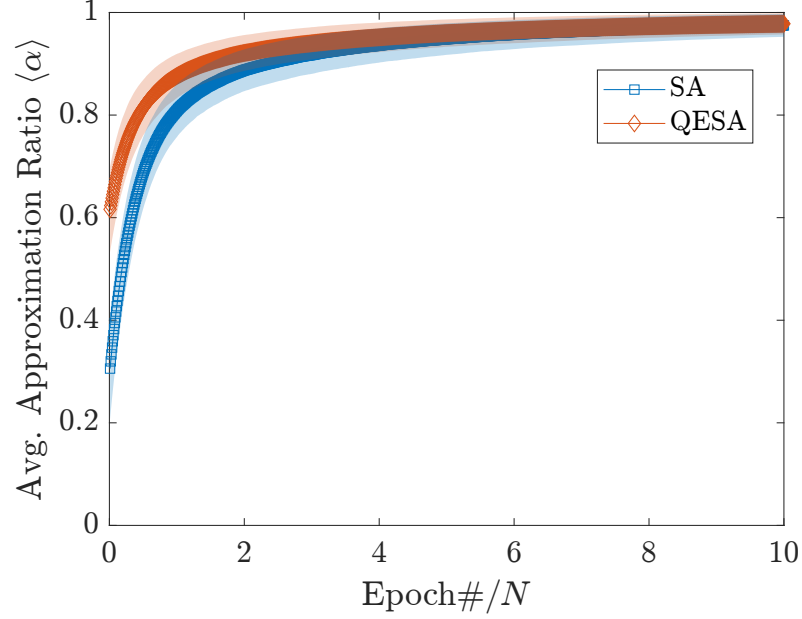
Figure 5.3: (a) AQC experimental data on an 11×18 atom array, (b) Approximation ratio change of SA (orange) and QESA (blue).

many-body correlations required for solving MIS problems even at large scalable problem sizes, since it does not contain system size-dependent errors arising from the energy landscape structure of the problem.

At the end of the experiment, the first step of the QESA procedure, the atomic states are measured. The measured experimental data is provided as a "warm start" input for the subsequent simulated annealing (SA) step [123]. The update rule for this SA step follows the previously reported "Rydberg Simulated Annealing" protocol [68]. This rule includes three main operations:

1. A free node can be added to the independent set. If node i is not occupied ($n_i = 0$) and none of its neighbors are occupied ($n_j = 0$ for all $(i, j) \in E$), then node i is proposed to be included in the set by setting $n_i = 1$.

2. Algorithm can swap the occupation between nodes. When node i is occupied ($n_i = 1$), its occupation can be swapped with one of its neighboring nodes. Specifically, for each neighboring node j, it can propose to swap the occupation of n_i and n_j with a probability of 1/8, resulting in the transition $n_i, n_j \to n_j, n_i$.

3. Finally, a node can be removed from the independent set. If neither of the above two options is applicable, node i is proposed for removal by setting $n_i = 0$.

When an update is proposed, the change in the cost Hamiltonian H_{MIS} associated with the MIS problem is calculated. The proposed state is then accepted or rejected according to the Metropolis-Hastings criterion [129, 130] at the current temperature T. If the proposed state has lower energy, the operation proceeds; otherwise, with a high probability, the system remains unchanged, resulting in the pass operation. After each update, the temperature T is gradually decreased according to a predefined schedule and the algorithm runs the next iteration. The Iterative Annealing step is terminated when the temperature reaches the final value of $T = 1/\beta = 0.03$ [68], and the resulting QESA solution is extracted.

Fig. 5.3 (b) shows the evolution of the approximation ratio α over time for a standalone SA (orange) and QESA (blue). We can see that the value of α increases over time. Each standalone SA starts with a random spin configuration where the total occupation number is the same as the AQC or QE result, and the approximation ratio increases as the epoch proceeds, where epoch refers to a step in the progression of SA runs. In contrast to SA, QESA starts from an AQC result. Through the QESA operation, this result converges more closely to the MIS solution. As shown in Fig. 5.3 (b), QESA outperforms SA in terms of approximation ratio, and the performance gap increases significantly, especially for graphs whose MIS solution is difficult to find. The mean approximation ratio and standard deviation (shaded area) are also shown in Fig. 5.3 (b).

5.3   Results

Figs. 5.4 show the average approximation ratio $\langle\alpha\rangle$ results of the QESA run and the standalone SA run according to the routine previously described in Sec. 5.2, based on the quantum experiment (AQC or QE) results. In both figures in Fig. 5.4, the y-axis shows the performance of QESA, and the x-axis shows the results of standalone SA starting from a randomized configuration $(n_1, n_2, \cdots)$ whose total occupation number is the same as the quantum experiment (i.e., the same total sum of occupation numbers, $\sum_i n_i$, as in the quantum experiment). Fig. 5.4 (a) shows the evolution of α over the progression (in Epoch#/N) of the AQC-based QESA method (using the archived AQC dataset [120]) applied to various experimental graphs chosen from the dataset, compared to the pure classical standalone SA (based on a random spin configuration with the same total occupation number as the AQC data) for the same graphs. Also, Fig. 5.4 (b) shows the evolution of α as the QE-based QESA method (using QE experiments implemented on the QuEra Aquila platform [125] accessed via the Amazon Bracket service) on the same graph set as in Fig. 5.4 (a), compared to the results of a pure classical standalone SA (with the same arbitrary spin configuration condition based on QE data instead of AQC) for the same graphs. In the results in Figs. 5.4 (a) and (b), a significant number of data points (97.5% for AQC and 91.9%

(a)

Approximation ratio α

(b)

Approximation ratio α
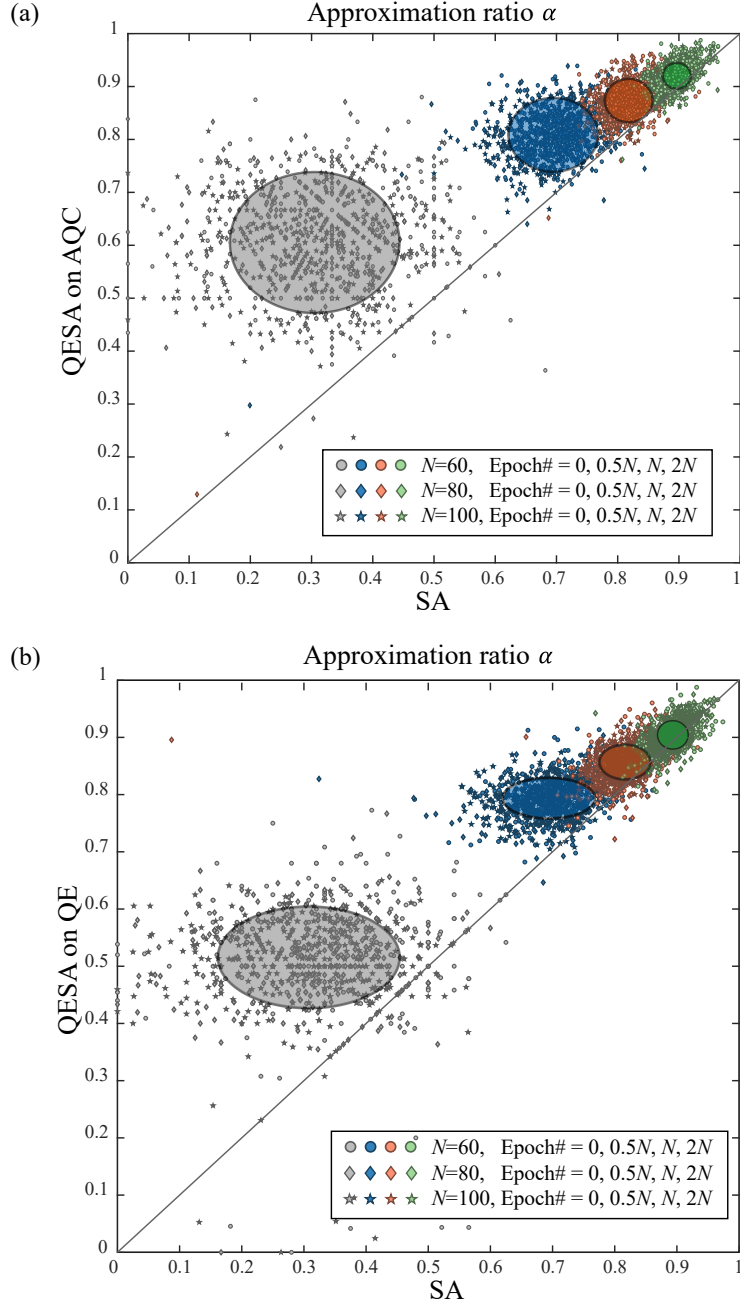
Figure 5.4: (a) Comparison of QESA vs. SA for AQC datasets. The approximation ratio (α) is plotted for AQC-based QESA (the y-axis) and compared with randomly initialized SA for the chosen graphs (the x-axis). A total of 924 graphs (atom arrangements) from the AQC datasets (#8,#9, #10, and #11) [120], with sizes $N = 60, 80$, and 100 (number of vertices $N \equiv |V|$), are analyzed and represented by circular, diamond, and pentagram scatter plots, respectively. Starting from the initial input (gray scatter plot), the SA algorithm progresses through epochs of $0.5N$ (blue scatter plot), N (orange scatter plot), and $2N$ (green scatter plot). As the number of epochs (Epoch#) increases, α improves, indicating better MIS approximations. (b) Comparison of QESA vs. SA for QE datasets. The same analysis is conducted for the above graphs using QE experiments. In (a) and (b), the size of the ellipses is the standard deviations $\sigma(\alpha)$, representing the spread of α.

for QE) lie above the $y = x$ line. Similarly, for Epoch#/$N = 0.5$, 1, and 2, a significant proportion of the data points are above the $y = x$ line: 98.1%, 95.5%, and 87.1% for the AQC results, and 97.0%, 88.7%, and 69.9% for the QE results. This demonstrates that QESA consistently outperforms pure classical SA for both types of QESA. These outcomes highlight the advantage of incorporating the Rydberg atom experiment results as a "warm start" that increases the chance that the SA algorithm can converge to higher-quality solutions for MIS problem compared to starting from a randomized configuration.
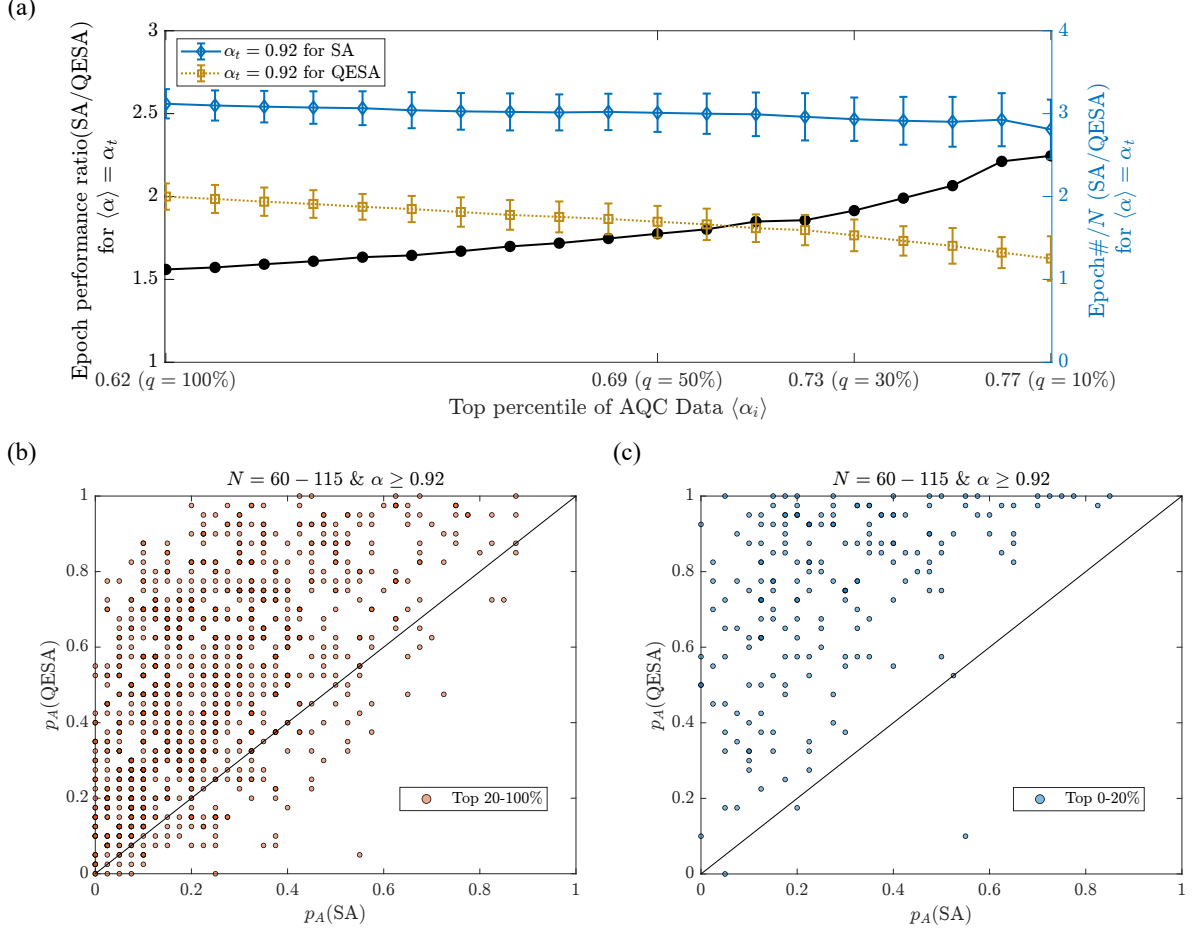
Figure 5.5: (a) The mean and standard deviation of Epoch#/N to reach the target approximation ratio α_t per number of vertices N. (b-c) The scatter plots of the probabilities $p_A(\text{QESA})$ and $p_A(\text{SA})$ where the average approximation ratios $\langle \alpha \rangle$ of QESA and SA reach the target $\alpha_t = 0.92$ at Epoch#/$N = 2$.

And, to analyze the performance gap between QESA and SA shown in Fig. 5.4, we plot the performance of QESA and SA as a function of initial approximation ratio α in Fig. 5.5 for a total 1200 kinds of graphs with $N = 60 - 115$ in Exp#10 of Ref. [120]. Fig. 5.5 (a) shows the mean and standard deviation of Epoch#/N required to reach the target approximation ratio α_t on the right y-axis. The x-axis represents the top percentile of the initial approximation ratio α_i of the AQC data or SA, and the left y-axis is the ratio of the average Epoch#/N of SA and QESA. As shown in Fig. 5.5 (a), it is observed that the larger α_i, the smaller the Epoch#/N required to reach the target α_t, where the ratios of the average Epoch#/N of SA and QESA are 1.56 for the top percentile $q = 100\%$ and 2.25 for $q = 10\%$. For each top percentile q, α_i for QESA is 0.62, 0.69, and 0.77 for $q = 100\%$, 50%, and 10%, respectively,

while α_i for SA is 0.31, 0.40, and 0.50 for $q = 100\%$, 50%, and 10%, respectively. Figs. 5.5 (b) and (c) show the probabilities $p_A(\text{QESA})$ and $p_A(\text{SA})$ that the QESA and SA results satisfy $\alpha \geq 0.92$ at Epoch#/$N = 2$. Fig. 5.5 (b) is for the top 20-100% cases and Fig. 5.5 (c) is for the top 20% cases, and the percentage of cases where $p_A(\text{QESA})$ is better than $p_A(\text{SA})$ is 97.9% for the top 20% cases (Fig. 5.5 (c)) compared to 88.2% for the top 20-100% cases (Fig. 5.5 (b)).

5.3.1   Degeneracy Density and Hardness Parameter of SA and QESA
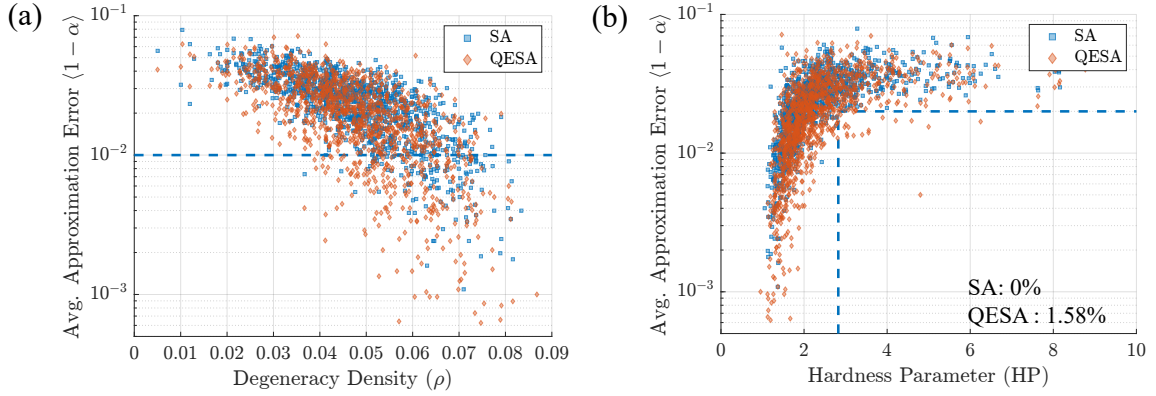
Figure 5.6: For Epoch#/$N = 10$, (a) Approximation error distribution per degeneracy density ($\rho \equiv \log(D_{|\text{MIS}|})/N$, $D_{|\text{MIS}|}$ is the number of MIS states) for SA (blue color) and QESA (orange color). The probabilities for $\alpha > 0.99$ are 10.58% (SA) and 19.17% (QESA) for each. As the degeneracy density increases, the approximation error decreases for both SA and QESA. (b) Approximation error $(1 - \alpha)$ distribution per hardness parameter (HP$\equiv D_{|\text{MIS}|-1}/(|\text{MIS}| \cdot D_{|\text{MIS}|})$, $|\text{MIS}|$ is the size of MIS and $D_{|\text{MIS}|-1}$ is the count of IS with the size $|\text{MIS}| - 1$) for (c) SA and (d) QESA. For the higher hardness parameter zone (HP $> \langle \text{HP} \rangle$, $\langle \text{HP} \rangle = 2.8243$ is the mean HP) , the number of MIS graphs where the approximation ratio > 0.98 is more at QESA case than the SA case.

There are two parameters in the graph that represent properties related to the difficulty of the MIS problem: the degeneracy density and the hardness parameter [68]. The degeneracy density is $\rho \equiv \log(D_{|\text{MIS}|})/N$, where $D_{|\text{MIS}|}$ is the number of MIS states and N is the number of nodes. The larger the number of MIS states in a graph, the larger ρ is, which in turn means that the larger ρ is, the easier it is to find a MIS solution for a given graph. The hardness parameter is HP $\equiv D_{|\text{MIS}|-1}/(|\text{MIS}| \cdot D_{|\text{MIS}|})$, where $|\text{MIS}|$ is the size of the MIS and $D_{|\text{MIS}|-1}$ is the number of independent sets of size $|\text{MIS}| - 1$. A larger HP indicates a harder MIS problem, since there are fewer transition paths to the MIS state.

Figs. 5.6 (a) and (b) show the distribution of approximation error $(1 - \alpha)$ as a function of the degeneracy density ρ and the hardness parameter HP for SA and QESA results for 1200 graphs which are used in Figs. 5.5. The probability for $\alpha > 0.99$ is 9.46% (SA) and 19.29% (QESA), respectively. For degeneracy densities $\rho \leq 0.035$, the SA results show no approximation ratios greater than 0.99, while the QESA results show a degeneracy density lower bound of ~ 0.02 for approximation ratio $\alpha > 0.99$. Also, for the higher hardness parameter regime (HP $> \langle \text{HP} \rangle (= 2.8243$, which is the mean HP)), the probability for $\alpha > 0.98$ is 0% (SA) and 1.58% (QESA).

5.3.2 Relationship between performance of QESA and Hamming distance

In this section, we focus on evaluating the computation time of QESA, denoted by Epoch#(QESA), required to achieve a target approximation ratio (e.g., $\alpha_t = 0.95$), and compare it to the computation time of pure classical standalone SA, denoted by Epoch#(SA). Hence, we use the ratio of Epoch# of SA and QESA as a performance measure of QESA over SA. Furthermore, based on multiple instances of using Hamming distance as a robust metric for performance evaluation and enhancement of various heuristic optimization algorithms (e.g., particle swarm optimization (PSO) [131, 132, 133], A* search algorithms [134] and hypergraph matching problems [135]), we identified the Hamming distance between the initial spin configuration s and the target spin configuration t, $\text{HD} \equiv |\{j \in 1, \cdots, N | s_j \neq t_j\}|$, as a figure of merit.

(a)

(b)
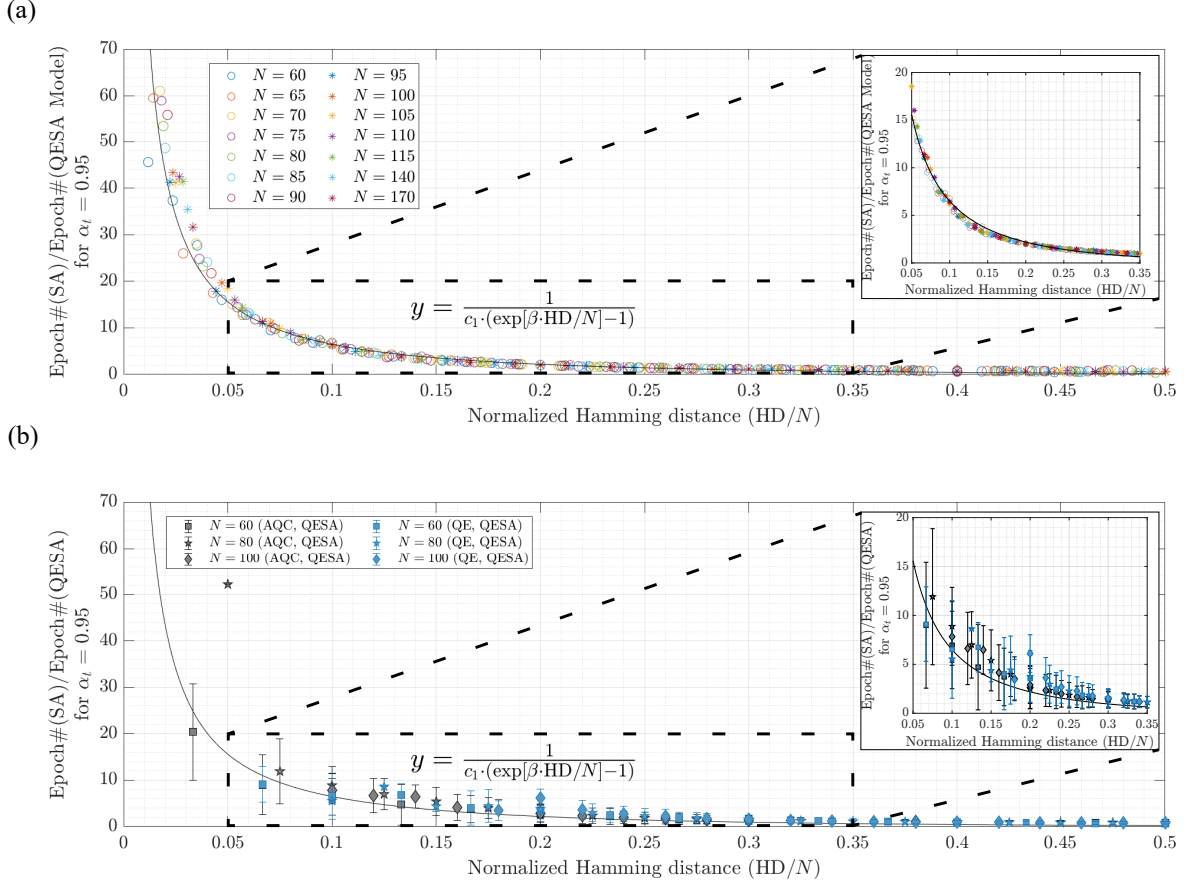
Figure 5.7: The relationship between Epoch# for $\alpha_t = 0.95$ and HD/N is depicted in two parts: (a) Epoch# ratio between SA and QESA models for 1200 graphs with $N = 60 - 115$, 93 graphs with $N = 140$, and 154 graphs with $N = 170$. The QESA model's monotonic behavior fits well to the black line $y = 1/[c_1 \cdot (\exp(\beta \cdot \text{HD}/N) - 1)]$, with $c_1 = 0.1602$, $\beta = 6.738$ and an adjusted $R^2_{\text{adj}} = 0.9838$, as detailed in the inset for HD/N = 0.05 − 0.35. (b) Epoch# ratio between SA and QESA for 924 graphs from Figs. 5.4 (a,b), with error bars representing AQC (black) and QE (blue).

In this respect, in Figs. 5.7 (a) and (b), we plot the ratios Epoch#(SA)/Epoch#(QESA Model) and Epoch#(SA)/Epoch#(QESA) for $\alpha_t = 0.95$ as a function of HD/N (Hamming distance normalized by the graph size N), respectively. The former ratio is based on a modeled QESA, which is detailed below. The required Epoch# of SA is modeled as Epoch#(SA) $= c_1 e^{\beta m^*}$ [136, 137]. In this case, m^* can be

approximated by HD/N, hence in Eq. (5.3), we model this ratio as a function $y(\text{HD}/N)$:

$$y(\text{HD}/N) = \frac{1}{c_1 \cdot (\exp[\beta \cdot \text{HD}/N] - 1)}, \tag{5.3}$$

where $c_1 = 0.1602$, $\beta = 6.738$ and an adjusted coefficient of determination $R^2_{\text{adj}} = 0.9838$, which explains over 98% of the variability in the data. The modeled QESA results in Fig. 5.7 (a) are obtained via the following procedure:

1. Sample the SA spin configurations that reached $\alpha_t = 0.95$ from the set of 1200 experimental graphs [120] of $N = 60 - 115$ in Exp#10, 93 graphs of $N = 140$, and 154 graphs of $N = 170$ and determine the epoch differences for the initial points $\alpha_i = 0.85$, 0.88, and 0.91 for $N = 60, 65, 70, \cdots, 115, 140, 170$.

2. Sort these epoch differences by HD for each N.

3. Compute the epoch performance ratio Epoch#(SA)/Epoch#(QESA Model), denoting the ratio of epochs for SA to those for QESA for each α_i, in accordance with these sorts of epoch differences.

In Fig. 5.7 (b), comparing the Epoch#(SA)/Epoch#(QESA) of AQC and QE (black and blue error bars, respectively) with the QESA model (Eq. (5.3)), it is observed that the epoch performance ratios of both AQC and QE closely follow the black fitting line of the QESA model. In addition, the zoomed-in plots for HD/$N = 0.05 - 0.35$ in the insets of Figs. 5.7 (a) and (b) show that Eq. (5.3) characterizes the average epoch performance ratio. This result indicates that QESA is advantageous due to the reduced computational time of QESA with a shorter quantum mechanically warm-started HD/N compared to randomly started SA.

5.3.3 Correlation between the Hamming distance and Initial Approximation ratio

Figure 5.8: (a-b) The relation between the normalized Hamming disance HD/N and the initial approximation ratio α_i, (a) Count Distribution of HD/N for each fixed $\alpha_i = 0.6$, 0.72, 0.81 and 0.9 from the QESA modeling results, (b) Epoch#(SA)/Epoch#(QESA Model) as a function of HD/N and α_i.

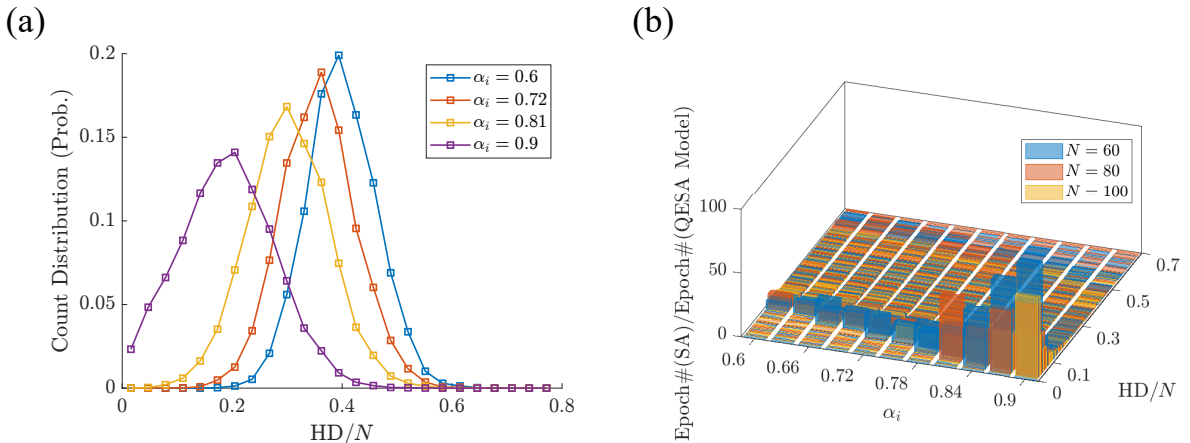In Figs. 5.5 and Figs. 5.7, we presented the behaviors of QESA's performance as a function of the initial approximation ratio α_i and the Hamming distance HD/N, respectively. As a result, the average epoch performance ratio of QESA tends to increase as α_i is larger and HD/N is smaller, in particular, it fits well with the monotonic behavior of modeling y(HD/N) (Eq. (5.3)) based on HD/N.

Hence, in this subsection, we examine the correlation between the Hamming distance HD/N and the initial approximation ratio α_i regarding how the change of α_i leads to the tendency of QESA's epoch performance shown in Fig. 5.5 (a). Figs. 5.8 (a) and (b) show the relationship between HD/N and α_i and the relationship between these two variables and QESA's epoch performance, respectively, for $\alpha_t = 0.95$. Fig. 5.8 (a) shows the distributions of HD/N for QESA modeling results of the same α_i. It shows that the mean HD/N decreases for distributions with larger α_i, which indicates the correlation that the higher α_i, the smaller the bit difference between the current independent set state and the target optimal state.

In Fig. 5.8 (b), the average QESA Epoch performance ratio behavior when both the two variables HD/N and α_i are taken into account is shown. In other words, Fig. 5.8 (b) simultaneously shows the relationship between the QESA Epoch performance ratio and HD/N and α_i as shown in Figs. 5.5 and Fig. 5.7, respectively, which shows that the correlation between HD/N and α_i as shown in Fig. 5.8 (a) leads to a decrease in the mean HD/N when α_i increases, which in turn leads to an increase in the Epoch performance of QESA when α_i increases as shown in Fig. 5.5 (a). Therefore, it shows that the tendency of QESA's performance with the initial approximation ratio α_i in Fig. 5.5 (a) is due to the negative correlation between α_i and HD/N and the relationship between Hamming distance HD/N and QESA's performance in Fig. 5.7.

5.4   Discussion

In this section, we discuss the issue of scaling with the number of atoms for using QESA. SA with inputs whose distribution of Hamming distances is widely spread is time-consuming since it examines all the many paths to incrementally increase α_i. In contrast, since QESA starts with a source with a partial error on a solution, it only pursues paths with shorter Hamming distances and thus reaches the solution faster. In other words, QESA can be regarded as a strict subset of SA with a warm start from a source with a shorter Hamming distance. Therefore, we can describe QESA via Hamming distance and SA analysis. Simulated annealing (SA) is a stochastic, iterative optimization algorithm that aims to find the optimal value of a cost function (in this case, H_{MIS} (Eq. (5.2))).

The probability of successfully finding the MIS is expressed as

$$P_{\mathrm{MIS,SA}} = 1 - \exp\big(-a\mathcal{HP}^{-1}/N \cdot \mathrm{Epoch\#(SA)}\big), \tag{5.4}$$

where $\mathcal{HP}$ is the hardness parameter of the given graph; for King's graphs, it is examined as $\ln \mathcal{HP} \sim \sqrt{N}$. [68] Consequently, the epoch-to-solution (ETS) [138] for the SA algorithm, denoted by $\mathrm{ETS}_{\mathrm{MIS,SA}}$, is given by

$$\mathrm{ETS}_{\mathrm{MIS,SA}} = aN \times \mathcal{HP} \sim aNe^{b\sqrt{N}}, \tag{5.5}$$

where a is a coefficient associated with the normalized Hamming distance HD/N (inversely proportional to the epoch performance ratio in Eq. (5.3)), and b is a parameter related to $\mathcal{HP}$ of the graph. This exponential scaling with $\sqrt{N}$ implies that as N increases, the number of iterations required for the algorithm to converge grows significantly.
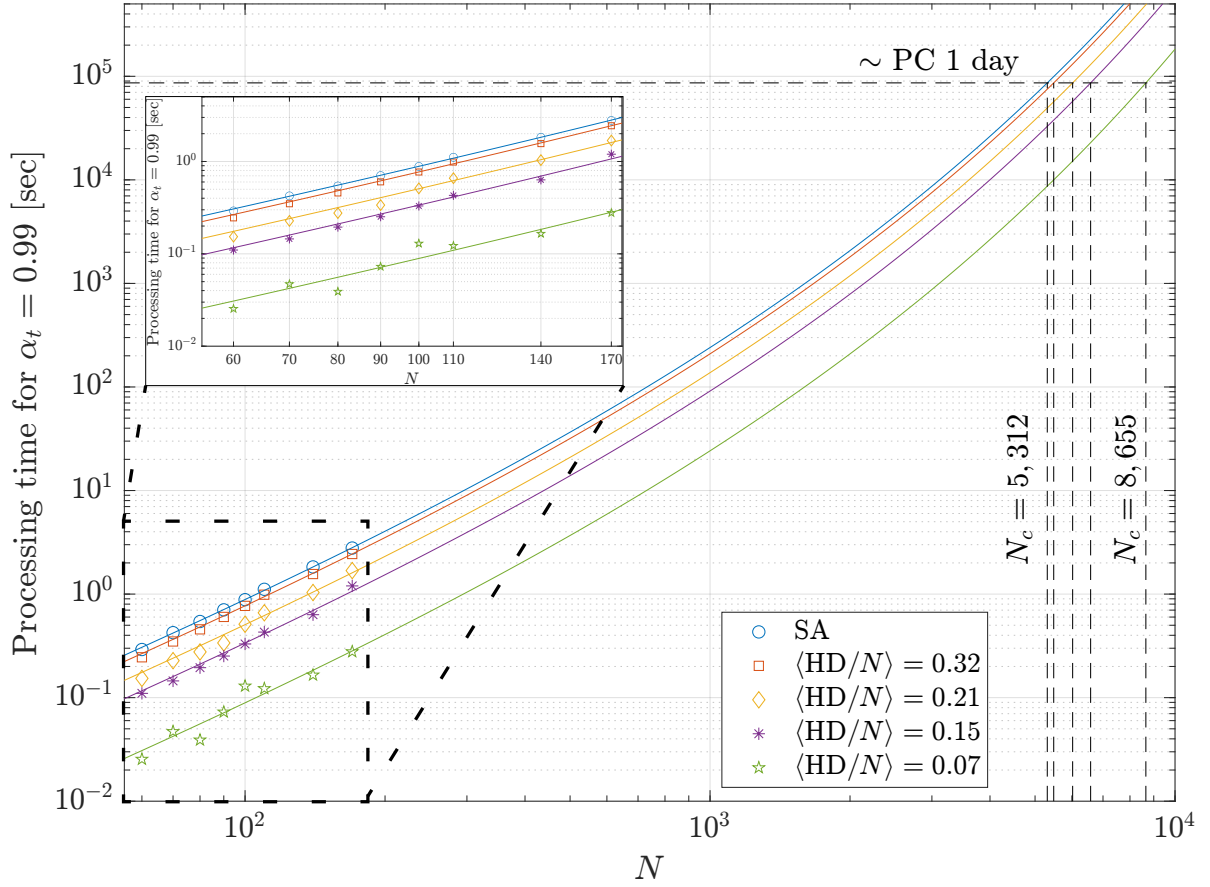
Figure 5.9: Scalability of graph size N for $\alpha_t = 0.99$ within a limited processing time of one day on PC. Each color means SA (blue) case (blue) and cases with different $\langle \mathrm{HD}/N \rangle$: 0.32 (orange), 0.21 (yellow) 0.15 (purple) and 0.07 (green). (Inset: Measured average processing time required to reach $\alpha_t = 0.99$ for $N = 60, 70, \cdots, 110, 140$ and 170.) The required processing time is estimated as $aN \times b^{\sqrt{N}} \times cN^d$ based on Equation 5.5 and the epoch performance ratio in Figure 5.7, where $a_0 = 5.0508, b = 1.0738$, $c = 25.44$ μs, $d = 0.76$ and $a_0/a = 1, 1.15, 1.74, 2.63$ and 9.94 for SA and $\langle \mathrm{HD}/N \rangle = 0.32, 0.21, 0.15$ and 0.07 cases, respectively. From these estimations, the upper bounds N_c of graph size within the one-day limit are predicted to be 5,312 for SA and as 5,484, 6,023, 6,584, and 8,655 for $\langle \mathrm{HD}/N \rangle = 0.32, 0.21$, 0.15 and 0.07 cases, respectively.

We assume that the average processing time per epoch, t_{step}, scales as a function of N:

$$t_{\mathrm{step}} = cN^d, \tag{5.6}$$

where the parameters c and d are determined by the specifications of the PC. Consequently, the total processing time for target α_t, denoted as $t_{\mathrm{processing}}$, is obtained as the product of Eqs. (5.5) and (5.6):

$$
\begin{aligned}
t_{\mathrm{processing}} &\equiv t_{\mathrm{step}} \times \mathrm{ETS}_{\mathrm{MIS,SA}} \\
&= aN \times b^{\sqrt{N}} \times cN^d. \tag{5.7}
\end{aligned}
$$

The scalability of $t_{\mathrm{processing}}$ is drawn in the inset in Figure 5.9, as HD/N varies and N increases for $\alpha_t = 0.99$. For $N = 60$ to 170, $t_{\mathrm{processing}}$ shows performance gaps of 1.15, 1.75, 2.63, and 9.94 times compared to the SA case, with $\langle \mathrm{HD}/N \rangle = 0.32, 0.21, 0.15$, and 0.07, respectively. In Figure 5.9, a,

related to HD/N, is fitted as $a = 5.05, 4.39, 2.89, 1.92, 0.51$ forthe SA case and $\langle \text{HD}/N \rangle = 0.32, 0.21,$ 0.15, and 0.07. b, related to $\mathcal{HP}$, is fitted as 1.0738, with R^2_{adj} values of 0.9981, 0.9929, 0.9758, 0.9625 and 0.8276 for SA case and $\langle \text{HD}/N \rangle = 0.32, 0.21, 0.15,$ and 0.07, respectively. c and d are related to the PC computing environment and fitted with values of 25.44 μs and 0.76, respectively, yielding R^2_{adj} values of 0.9826. The PC operational environment is MATLAB R2023a with an AMD Ryzen Threadripper 3960X 24-Core processor, NVIDIA GeForce RTX 3080 GPU, and 64.0 GB of RAM. It is assumed that the RAM does not significantly influence the extrapolation.

We now attempt to estimate the maximum graph size N_c that can be processed when $t_{\text{processing}}$ is constrained by a finite PC operation time, such as within 1 day. Extrapolating the numerically fitted scaling as Figure 5.9, $N_c = 5,312$ is expected for SA alone. However, for the QESA approach, N_c could increase to 5,484, 6,023, 6,584 and 8,655, for graphs having initial Hamming distances, HD/$N = 0.32,$ 0.21, 0.15 and 0.07, respectively. This suggests that QESA is capable of handling larger problem instances than the SA algorithm alone.
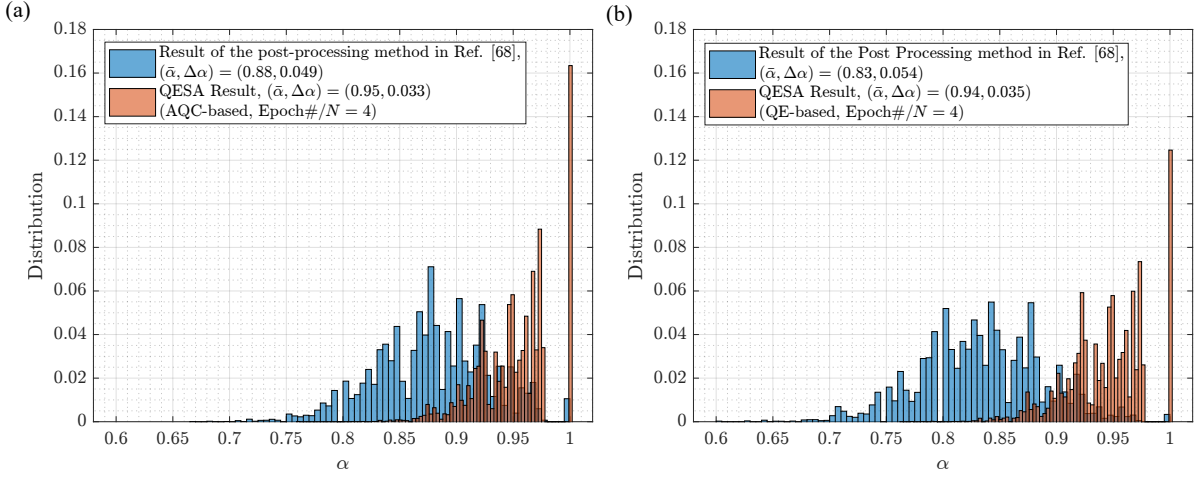
Figure 5.10: Distribution comparsions between the post-processing method (blue-colored) in Ref. [68] and QESA (orange-colored) for the approximation ratio α results, using the (a) AQC-based and (b) QE-based inputs utilized as the "warm start"s of QESA in Figs. 5.4 (a) and (b), respectively.

Furthermore, we compare the post-processing method [68] with the QESA method. Figs. 5.10 (a) and (b) show the approximation ratio α distributions of the AQC and QE experimental results with warm-start, respectively. The orange color is the QESA method, and the blue color is the post-processing method. The mean values of the QESA case are 0.95 (AQC) and 0.94 (QE), while the mean values of the post-processing method are 0.88 (AQC) and 0.83 (QE). In addition, the distribution of α is concentrated within a sharper interval in QESA, while the post-processing method has a wider distribution. This is due to the occupation swap process in QESA, which results in a spin exchange between the neighboring $|0\rangle$ and $|1\rangle$, i.e., the QESA iterative loop finds the optimal configuration via spin swapping, which increases α. In contrast, the post-processing does not include this occupation swap process, so there is no spin swapping between the neighboring $|0\rangle$ and $|1\rangle$, which limits the increase in α.

5.5 Summary

In this chapter, we highlight the computational time advantages of QESA using MIS experimental results from adiabatic quantum computing (AQC) (using a previously reported dataset [120]) and quench evolution (QE) (using newly run experiments [125] on the QuEra Aquila machine) on Rydberg atom arrays with approximately 100-atom scale. QESA shows a computational time advantage over classical standalone simulated annealing (SA). In particular, as a principle, we present a new correlation between the computation time of QESA and the Hamming distance. By analyzing the epoch time dependence of SA on Hamming distance, we found that QESA outperforms SA by leveraging the quantum-optimized Hamming distance distribution, as opposed to SA's non-optimized Hamming distance distribution. In other words, SA, which uses inputs from widely distributed Hamming distances, is time-consuming since it examines all of the many paths that incrementally increase α. However, since QESA starts from a warm start with partial errors on the solution, it only pursues paths with short Hamming distances and thus reaches the solution faster. This is possible since QESA experimental results are less likely to be on the path to a non-MIS solution than an SA start with the same initial approximation ratio α_i. Furthermore, QESA modeling estimates the scalability of N values such that α can reach 0.99 within a given time when using a "warm start" prepared with the expected HD$/N$.

The dataset is available on the *figshare* data repository [139]:

- Dataset collection in *figshare* (https://doi.org/10.6084/m9.figshare.c.7639259.v1).

And the dataset consists of following three categories used for this chapter:

1. Codes (https://doi.org/10.6084/m9.figshare.28260860.v1),

2. Data (https://doi.org/10.6084/m9.figshare.28254581.v1),

3. Figures (https://doi.org/10.6084/m9.figshare.28256084.v1).

Chapter 6.   Conclusion

In this thesis, by utilizing the properties and configurations of neutral Rydberg atoms, the implementation and effectiveness of Rydberg quantum programming using optical gates and satisfiability (SAT) problem, and a hybrid programming approach combining quantum experiments and software, are introduced and explored.

First, we design multiple sets of Rydberg universal optical gates by utilizing auxiliary atoms (wire atoms) to mediate coupling between qubit atoms (data atoms). We show that quantum gates can be designed based on the single-atom addressing coding of lasers and the strong local interaction of neutral Rydberg atoms. Then, we propose two kinds of Rydberg atom quantum programming schemes. The first one is programming that converts a mathematical problem into a qubit array structure to fit a maximum independent set (MIS) problem, which uses the Rydberg blockade property of the Rydberg atom upon transition to the ground state during adiabatic quantum computing (AQC). We present a quantum algorithm that programs 3-SAT instances which are proto-typical NP-complete instances requiring many steps to solve sequentially in classical computing and then into an array of qubits in the MIS domain. The arrays assembled by this 3-SAT reduction algorithm undergo quantum adiabatic experiments, and the results of these ground state demonstrate solving instances with the satisfiability evaluations of 84-95% (for three two-clause instances) and 74-81% (for three three-clause instances), significantly higher than the random guessing. According to the Cook-Levin theorem, all NP problems can be transformed into SAT, so this SAT quantum algorithm programmed with Rydberg atoms can be of great help.

It is difficult to improve both quality (noise) and scalability (the number of atoms) in a Rydberg quantum system, so to decrease the number of iterations of the quantum adiabatic process, we program Rydberg quantum-enhanced simulated annealing (QESA), which combines quench evolution (QE) and adiabatic quantum computing (AQC) experimental data with simulated annealing (SA) algorithms to improve accuracy and time. In this thesis, we demonstrate that QESA efficiently reaches the target approximation ratio α_t compared to SA. Using the experimental results of around 100 Rydberg atoms as a warm start, QESA outperforms SA. The gap in performance is strongly correlated with the Hamming distance between the target and the initial point. The scalability of the number of atoms N, which is difficult to handle in experiments, is estimated by modeling: when the normalized Hamming distance HD$/N \sim 0.05$ for $\alpha_t = 0.95$, the performance difference between SA and QESA is evaluated as Epoch#(SA)/Epoch#(QESA) ~ 15. We hope that this research helps to advance quantum computing by utilizing Rydberg atoms in the future.

Bibliography

[1] R. P. Feynman, Simulating physics with computers, Int. J. Theor. Phys. **21**, 467–488 (1982).

[2] M. A. Nielsen and I. Chuang, *Quantum computation and quantum information* (Cambridge Univ. Press, Cambridge, 2002).

[3] J. L. O'brien, Optical Quantum Computing, Science **318**, 1567 (2007).

[4] P. Kok, W. J. Munro, K. Nemoto, T. C. Ralph, J. P. Dowling, and G. J. Milburn, Linear optical quantum computing with photonic qubits, Rev. Mod. Phys. **79**, 135 (2007).

[5] F. Arute, K. Arya, R. Babbush, *et al.*, Quantum supremacy using a programmable superconducting processor, Nature **574**, 505–510 (2019).

[6] P. Krantz, M. Kjaergaard, F. Yan, T. P. Orlando, S. Gustavsson, and W. D. Oliver, A quantum engineer's guide to superconducting qubits, Appl. Phys. Rev. **6**, 021318 (2019).

[7] A. Blais, A. L. Grimsmo, S.M. Girvin, and A. Wallraff, Circuit quantum electrodynamics, Rev. Mod. Phys. **93**, 025005 (2021).

[8] D. Kielpinski, C. Monroe, and D. J. Wineland, Architecture for a large-scale ion-trap quantum computer, Nature **417**, 709-711 (2002).

[9] P. Schindler, D. Nigg, T. Monz, J. T. Barreiro, E. Martinez, S. X. Wang, S. Quint, M. F. Brandl, V. Nebendahl, C. F. Roos, M. Chwalla, M. Hennrich, and R. Blatt, A quantum information processor with trapped ions, New J. Phys. **15**, 123012 (2013).

[10] I. Pogorelov, T. Feldker, C. D. Marciniak, L. Postler, G. Jacob, O. Kriegelsteiner, V. Podlesnic, M. Meth, V. Negnevitsky, M. Stadler *et al.*, Compact Ion-Trap Quantum Computing Demonstrator, PRX Quantum **2**, 020343 (2021).

[11] T. van der Sar, Z. H. Wang, M. S. Blok, H. Bernien, T. H. Taminiau, D. M. Toyli, D. A. Lidar, D. D. Awschalom, R. Hanson, and V. V. Dobrovitski, Decoherence-protected quantum gates for a hybrid solid-state spin register, Nature **484**, 82–86 (2012).

[12] L. Childress and R. Hanson, Diamond NV centers for quantum computing and quantum networks, MRS Bulletin **38**, 134 (2013).

[13] D. Weiss and M. Saffman, Quantum computing with neutral atoms, Phys. Today **70**, 44 (2017).

[14] L. Henriet, L. Beguin, A. Signoles, T. Lahaye, A. Browaeys, G.-O. Reymond, and C. Jurczak, Quantum computing with neutral atoms, Quantum **4**, 327 (2020).

[15] M. Saffman, T. G. Walker, and K. Mølmer, Quantum information with Rydberg atoms, Rev. Mod. Phys. **82**, 2313 (2010).

[16] M. Saffman, Quantum computing with atomic qubits and Rydberg interactions: progress and challenges, J. Phys. B: At. Mol. Opt. Phys. **49**, 202001 (2016).

[17] M. Kim, Y. Song, J. Kim, and J. Ahn, Quantum Ising Hamiltonian Programming in Trio, Quartet, and Sextet Qubit Systems, PRX Quantum **1**, 020323 (2020).

[18] Y. Song, M. Kim, H. Hwang, W. Lee, and J. Ahn, Quantum simulation of Cayley-tree Ising Hamiltonians with three-dimensional Rydberg atoms, Phys. Rev. Res. **3**, 013286. (2021).

[19] M. Kim, K. Kim, J. Hwang, E.-G. Moon, and J. Ahn, "Rydberg quantum wires for maximum independent set problems," Nat. Phys. **18**, 755 (2022).

[20] H. Jo, Y. Song, M. Kim, and J. Ahn, Rydberg Atom Entanglements in the Weak Coupling Regime, Phys. Rev. Lett. **124**, 033603 (2020).

[21] A. Gaëtan, Y. Miroshnychenko, T. Wilk, A. Chotia, M. Viteau, D. Comparat, P. Pillet, A. Browaeys, and P. Grangier, Observation of collective excitation of two individual atoms in the Rydberg blockade regime, Nat. Phys. **5**, 115–118 (2009).

[22] E. Urban, T. A. Johnson, T. Henage, L. Isenhower, D. D. Yavuz, T. G. Walker, and M. Saffman, Observation of Rydberg blockade between two atoms, Nat. Phys. **5**, 110–114 (2009).

[23] D. Jaksch, J. I. Cirac, P. Zoller, S. L. Rolston, R. Côté, and M. D. Lukin, Fast Quantum Gates for Neutral Atoms, Phys. Rev. Lett. **85**, 2208 (2000).

[24] X.-F. Shi, Deutsch, Toffoli, and CNOT Gates via Rydberg Blockade of Neutral Atoms, Phys. Rev. Applied **9**, 051001 (2018).

[25] X.-F. Shi, Transition Slow-Down by Rydberg Interaction of Neutral Atoms and a Fast Controlled-not Quantum Gate, Phys. Rev. Applied **14**, 054058 (2020).

[26] M. Saffman, I. I. Beterov, A. Dalal, E. J. Páez, and B. C. Sanders, Symmetric Rydberg controlled-Z gates with adiabatic pulses, Phys. Rev. A **101**, 062309 (2020).

[27] L. Isenhower, E. Urban, X. L. Zhang, A. T. Gill, T. Henage, T. A. Johnson, T. G. Walker, and M. Saffman, Demonstration of a Neutral Atom Controlled-NOT Quantum Gate, Phys. Rev. Lett. **104**, 010503 (2010).

[28] H. Levine, A. Keesling, A. Omran, H. Bernien, S. Schwartz, A. S. Zibrov, M. Endres, M. Greiner, V. Vuletić, and M. D. Lukin, High-Fidelity Control and Entanglement of Rydberg-Atom Qubits, Phys. Rev. Lett. **121**, 123603 (2018).

[29] H. Levine, A. Keesling, G. Semeghini, A. Omran, T. T. Wang, S. Ebadi, H. Bernien, M. Greiner, V. Vuletić, H. Pichler, and M. D. Lukin, Parallel Implementation of High-Fidelity Multiqubit Gates with Neutral Atoms, Phys. Rev. Lett. **123**, 170503 (2019).

[30] T. M. Graham, M. Kwon, B. Grinkemeyer, Z. Marra, X. Jiang, M. T. Lichtman, Y. Sun, M. Ebert, and M. Saffman, Rydberg-Mediated Entanglement in a Two-Dimensional Neutral Atom Qubit Array, Phys. Rev. Lett. **123**, 230501 (2019).

[31] I. S. Madjarov, J. P. Covey, A. L. Shaw, J. Choi, A. Kale, A. Cooper, H. Pichler, V. Schkolnik, J. R. Williams, and M. Endres, High-fidelity entanglement and detection of alkaline-earth Rydberg atoms, Nat. Phys. **16**, 857–861 (2020).

[32] T. M. Graham, Y. Song, J. Scott, C. Poole, *et al.*, Demonstration of multi-qubit entanglement and algorithms on a programmable neutral atom quantum computer, arXiv:2112.14589.

[33] N. Schine, A. W. Young, W. J. Eckner, M. J. Martin, and A. M. Kaufman, Long-lived Bell states in an array of optical clock qubits, arXiv:2111.14653.

[34] P. Selinger, "Towards a quantum programming language," Mathematical Structures in Computer Science, **14**, pp. 527–586, (2004).

[35] N. D. Mermin, *Quantum Computer Science: An Introduction* (Cambridge Univ. Press, Cambridge, 2007).

[36] T. F. Gallagher, (2005). Rydberg Atoms. Cambridge University Press.

[37] Manuel Endres et al. , "Atom-by-atom assembly of defect-free one-dimensional cold atom arrays," Science **354**, 1024-1027 (2016).

[38] Levine, H. et al. (2019). Parallel Implementation of High-Fidelity Multiqubit Gates with Neutral Atoms. Phys. Rev. Lett., **123**, 170503 (2019).

[39] H. J. Metcalf and P. van der Straten, Laser Cooling and Trapping (Springer, New York, 1999).

[40] D. A. Steck, "Rubidium 87 D line data," (2001).

[41] W. Li, I. Mourachko, M. W. Noel, and T. F. Gallagher, "Millimeter-wave spectroscopy of cold Rb Rydberg atoms in a magneto-optical trap:Quantum defects of the ns, np, and nd series," Phys. Rev. A, **67**, 052502 (2003).

[42] E. Brion, L. H. Pedersen and K. Mølmer, "Adiabatic elimination in a lambda system," J. Phys. A: Math. Theor. **40**, 1033 (2007).

[43] V. Gorini, A. Kossakowski, and E. C. G. Sudarshan, "Completely positive dynamical semigroups of N-level systems," J. Math. Phys. **17**, 821 (1976).

[44] I. I. Beterov, I. I. Ryabtsev, D. B. Tretyakov, and V. M. Entin, "Quasiclassical calculations of blackbody-radiationinduced depopulation rates and effective lifetimes of Rydberg nS, nP, and nD alkali-metal atoms with $n \leq 80$," Phys. Rev. A **79**, 052504 (2009).

[45] M. Sipser, *Introduction to the Theory of Computation* (3rd edition, Cengage, 2012).

[46] S. Arora and B. Barak, *Computational Complexity: A Modern Approach* (Cambridge Univ. Press, 2009).

[47] J. Kleinberg, and É.Tardos, *Algorithm Design* (Pearson, 2006).

[48] O. Goldreich, *Foundations of Cryptography* (Cambridge Univ. Press, Cambridge, 2008).

[49] M. R. Garey and D. S. Johnson, *Computers and Intractability A Guide to the Theory of NP-Completeness* (W. H. Freeman, 1979).

[50] A. S. Fraenkel, and D. Lichtenstein, "Computing a perfect strategy for $n \times n$ chess requires time exponential in n," Journal of Combinatorial Theory, Series A, **31**, 199 (1981).

[51] C. Papadimitriou, *Computational Complexity* (Addison-Wesley, 1994).

[52] W. J. Savitch, "Relationships between nondeterministic and deterministic tape complexities," Journal of Computer and System Sciences, **4**, 177 (1970).

[53] H. R. Lewis and C. H. Papadimitriou, *Elements of the Theory of Computation*, (2nd edition, Prentice-Hall, 1981)

[54] M. Y. Vardi, "The complexity of relational query languages," Proceedings of the fourteenth annual ACM symposium on Theory of computing (STOC '82). Association for Computing Machinery, New York, NY, USA, pp. 137-146 (1982).

[55] D. Deutsch, "Quantum theory, the Church–Turing principle and the universal quantum computer," Proc. R. Soc. Lond. A, **400**, 97 (1985).

[56] R. Diestel, *Graph Theory* (5th edition, Springer, 2017).

[57] J. M. Robson, "Algorithms for maximum independent sets," Journal of Algorithms, **7**, 425 (1986).

[58] D. Zuckerman, "Linear Degree Extractors and the Inapproximability of Max Clique and Chromatic Number," Theory of Computing, **3**, 103 (2007).

[59] C. Dalyac and L. Henriet, "Embedding the MIS problem for non-local graphs with bounded degree using 3D arrays of atoms," arXiv:2209.05164.

[60] C. Dalyac, L.-P. Henry, M. Kim, J. Ahn, L. Henriet, "Exploring the impact of graph locality for the resolution of the maximum-independent-set problem with neutral atom devices," Phys. Rev. A **108**, 052323 (2023).

[61] A. Ephremides and T. V. Truong, "Scheduling broadcasts in multihop radio networks," IEEE Transactions on Communications, **38**, 456 (1990).

[62] O. Göbel, M. Hoefer, T. Kesselheim, T. Schleiden, and B. Vöcking, "Online Independent Set Beyond the Worst-Case: Secretaries, Prophets, and Periods," arXiv:1307.3192 (2013).

[63] Ramprasath S, Meghna Madhusudan, Arvind K. Sharma, Jitesh Poojary, Soner Yaldiz, Ramesh Harjani, Steven M. Burns, and Sachin S. Sapatnekar, "Analog/Mixed-Signal Layout Optimization using Optimal Well Taps," Proceedings of the 2022 International Symposium on Physical Design (ISPD '22), Association for Computing Machinery, New York, NY, USA, pp. 159–166 (2022). https://doi.org/10.1145/3505170.3506728

[64] D. Puthal, S. Nepal, C. Paris, R. Ranjan and J. Chen, "Efficient Algorithms for Social Network Coverage and Reach," 2015 IEEE International Congress on Big Data, New York, NY, USA, 2015, pp. 467-474 (2015).

[65] R. E. Tarjan and A. E. Trojanowski, "Finding a maximum independent set," SIAM Journal on Computing, **6**, 537 (1977).

[66] M. M. Halldórsson, "Approximations of independent sets in graphs," Approximation Algorithms for Combinatiorial Optimization (APPROX 1998). Lecture Notes in Computer Science, Vol. **1444**. Springer, Berlin, Heidelberg. (1998) https://doi.org/10.1007/BFb0053959

[67] D. V. Andrade, M. G. C. Resende, and R. F. Werneck, "Fast local search for the maximum independent set problem," J. Heuristics **18**, 525–547 (2012). https://doi.org/10.1007/s10732-012-9196-4

[68] S. Ebadi et al., "Quantum optimization of maximum independent set using Rydberg atom arrays," Science **376**, 1209 (2022).

[69] H. Pichler,, S.-T. Wang,, L. Zhou, S. Choi, and M. D. Lukin, "Quantum Optimization for Maximum Independent Set Using Rydberg Atom Arrays," arXiv:1808.10816 (2018)

[70] Y. Song, M. Kim, H. Hwang, W. Lee, J. Ahn, "Quantum simulation of Cayley-tree Ising Hamiltonians with three dimensional Rydberg atoms," Phys. Rev. Res. **3**, 013286 (2021).

[71] P. Scholl, A. L. Shaw, R. BS. Tsai, et al., "Erasure conversion in a high-fidelity Rydberg quantum simulator," Nature **622**, 273–278 (2023).

[72] S. Jeong, M. Kim, M. Hhan, J. Park, and J. Ahn, "Quantum programming of the satisfiability problem with Rydberg atom graphs," Phys. Rev. Res. **5**, 043037 (2023).

[73] A. Byun, M. Kim, J. Ahn, "Finding the maximum independent sets of Platonic graphs using Rydberg atoms," PRX Quantum, **3**, 030305 (2022).

[74] J. Dalibard and C. Cohen-Tannoudji, "Laser cooling below the Doppler limit by polarization gradients: simple theoretical models," J. Opt. Soc. Am. B **6**, 2023-2045 (1989).

[75] R. Grimm, M. Weidemüller, and Y. B. Ovchinnikov, "Optical Dipole Traps for Neutral Atoms," Adv. At. Mol. Opt. Phys. **42**, 95–170 (2000).

[76] H. Kim, M. Kim, W. Lee, and J. Ahn, "Gerchberg-Saxton algorithm for fast and efficient atom rearrangement in optical tweezer traps," Opt. Express **27**(3), 2184 (2019).

[77] W. Lee, H. Kim, and J. Ahn, "Defect-free atomic array formation using the Hungarian matching algorithm," Phys. Rev. A **95**, 053424 (2017).

[78] F. Nogrette, H. Labuhn, S. Ravets, D. Barredo, L. B´eguin, A. Vernier, T. Lahaye, and A. Browaeys, "Single-Atom Trapping in Holographic 2D Arrays of Microtraps with Arbitrary Geometries," Phys. Rev. X **4**, 021034 (2014).

[79] H. Kim, W. Lee, H.-g. Lee, H. Jo, Y. Song, and J. Ahn "In situ single-atom array synthesis using dynamic holographic optical tweezers," Nat. Commun. **7**, 13317 (2016)

[80] Y. Song, M. Kim, H. Hwang, W. Lee, and J. Ahn, "Quantum simulation of Cayley-tree Ising Hamiltonians with threedimensional Rydberg atoms," Phys. Rev. Res. **3**, 013286 (2021).

[81] A. Byun, M. Kim, and J. Ahn, "Finding the maximum independent sets of Platonic graphs using Rydberg atoms," PRX Quantum **3**, 030305 (2022).

[82] S. de Léséleuc, D. Barredo, V. Lienhard, A. Browaeys, and T. Lahaye, "Analysis of imperfections in the coherent optical excitation of single atoms to Rydberg states," Phys. Rev. A **97**, 053803 (2018).

[83] S. Jeong, X-F. Shi, M. Kim and J. Ahn "Rydberg Wire Gates for Universal Quantum Computation," Front. Phys. **10**, 875673 (2022).

[84] K. M. Maller, M. T. Lichtman, T. Xia, Y. Sun, M. J. Piotrowicz, A. W. Carr, L. Isenhower, and M. Saffman, "Rydberg-blockade controlled-not gate and entanglement in a two-dimensional array of neutral-atom qubits," Phys. Rev. A **92**, 022336 (2015).

[85] R. Cabrera, T. Strohecker, H. Rabitz, "The canonical coset decomposition of unitary matrices through Householder transformations," J. Math. Phys., **51**, 082101 (2010).

[86] F. Barahona, "On the computational complexity of Ising spin glass models," J. Phys. A **15**, 3241–3253 (1982).

[87] C. Monroe, W. C. Campbell, L.-M. Duan, et al., "Programmable quantum simulations of spin systems with trapped Ions," Rev. Mod. Phys. **93**, 025001 (2021).

[88] S. Ebadi, T. T. Wang, H. Levine, H. et al., "Quantum phases of matter on a 256-atom programmable quantum simulator," Nature **595**, 227 (2021).

[89] P. Shor, "Algorithms for quantum computation: discrete logarithms and factoring" Proceedings 35th Annual Symposium on Foundations of Computer Science. IEEE Comput. Soc. Press: 124 (1994). doi: 10.1109/SFCS.1994.365700.

[90] L. K. Grover, "Quantum mechanics helps in searching for a needle in a haystack," Phys. Rev. Lett. **79**, 325 (1997).

[91] E. Farhi, J. Goldstone, S. Gutmann, J Lapan, A. Lundgren, and D. Preda, "A quantum adiabatic evolution algorithm applied to random instances of an NP-complete problem," Science **292**, 472 (2001).

[92] N. G. Dickson and M. H. S. Amin, "Does adiabatic quantum optimization fail for NP-complete problems?," Phys. Rev. Lett. **106**, 050502 (2011).

[93] R. M. Karp, "Reducibility among combinatorial problems," In: R. E. Miller, J. W. Thatcher, and Bohlinger JD, *Complexity of Computer Computations* (Plenum Press, New York,1972).

[94] S. A. Cook "The complexity of theorem proving procedures," Proceedings of the Third Annual ACM Symposium on Theory of Computing, 151 (1971).

[95] H. K. Büning and T. Lettmann, *Propositional Logic: Deduction and Algorithms* (Cambridge University Press, 1999).

[96] V. V. Vazirani, *Approximation Algorithms* (Springer, Berlin, Heidelberg, 2003).

[97] A. Lucas, "Ising formulations of many NP problems," Frontiers in Physics **2**, 1 (2014).

[98] V. Choi, "Adiabatic quantum algorithms for the NP-complete maximum-weight independent set, exact cover and 3SAT problems," arXiv:1004.2226 (2010).

[99] E. Boros and P.L. Hammer. "The max-cut problem and quadratic 0-1 optimization; polyhedral aspects, relaxations and bounds," Ann. of Oper. Res. **33**, 151 (1991).

[100] F. Glover, G. Kochenberger, R. Hennig, et al. "Quantum bridge analytics I: a tutorial on formulating and using QUBO models," Ann. Oper. Res. **314**, 141 (2022).

[101] A. Byun, J. Jung, K. Kim, M. Kim, S. Jeong, H. Jeong, J. Ahn, "Rydberg-atom graphs for quadratic unconstrained binary optimization problems," Adv. Quantum. Technol., **2024**, 2300398 (2024).

[102] W. Lee, M. Kim, H. Jo, Y. Song, and Jaewook Ahn, "Coherent and dissipative dynamics of entangled few-body systems of Rydberg atoms," Phys. Rev. A **99**, 043404 (2019).

[103] S. Weber et al. "Hardware considerations for high-connectivity quantum annealers," APS March Meeting Abstracts **2018**, A33-008 (2018).

[104] X. Qiu, P. Zoller, and X. Li, "Programmable quantum annealing architectures with Ising quantum wires", PRX Quantum **1**, 020311 (2020).

[105] S. Fey, S. C. Kapfer, and K. P. Schmidt, "Quantum criticality of two-dimensional quantum magnets with long-range interactions," Phys. Rev. Lett. **122**, 017203 (2019).

[106] P. Scholl, M. Schuler, H. J. Williams, et al, "Quantum simulation of 2D antiferromagnets with hundreds of Rydberg atoms," Nature **595**, 233–238 (2021).

[107] A. Kerman, "Design and simulation of complex superconducting circuits for advanced quantum annealing hardware," In APS March Meeting Abstracts **2018**, C26001 (2018).

[108] A. Kerman, "Paramagnetic tree coupling of spin qubits," US patent 10,719,775 (2020).

[109] Y. S. Teo, H. Zhu, B. G. Englert, J. Rehacek, and Z. Hradil, "Quantum-state reconstruction by maximizing likelihood and entropy," Phys. Rev. Lett. **107**, 020404 (2011).

[110] M.-T. Nguyen, J.-G. Liu, J. Wurtz, M. D. Lukin, S.-T. Wang, and H. Pichler, "Quantum optimization with arbitrary connectivity using Rydberg atom arrays," PRX Quantum **4**,010316 (2023).

[111] R. P. Feynman, "Simulating physics with computers," Int. J. Theor. Phys. **21**, 467 (1982).

[112] J. Dowling, G. Milburn, "Quantum technology: the second quantum revolution," Phil. Trans. **361**, 1655 (2003).

[113] C. Monroe, W. C. Campbell, L.-M. Duan, Z.-X. Gong, A. V. Gorshkov, P. W. Hess, R. Islam, K. Kim, N. M. Linke, G. Pagano, P. Richerme, C. Senko, N. Y. Yao, "Programmable quantum simulations of spin systems with trapped ions," Rev. Mod. Phys. **93**, 025001 (2021).

[114] G. Wendin, "Quantum information processing with superconducting circuits: a review" Rep. Prog. Phys. **80**, 106001 (2017).

[115] F. Arute, et. al., "Quantum supremacy using a programmable superconducting processor," Nature (London), **574**, 505 (2019).

[116] C. S. Adams, J. D. Pritchard, J. P. Shaffer, "Rydberg atom quantum technologies," J. Phys. B: At. Mol. Opt. Phys. **53**, 012002 (2020).

[117] M Saffman, "Quantum computing with atomic qubits and Rydberg interactions: progress and challenges," J. Phys. B: At. Mol. Opt. Phys., **49**, 202001 (2016).

[118] S. K. Barik, A. Thakur, Y. Jindal, B. S. Silpa, S. Roy, "Quantum technologies with Rydberg atoms," Front. Quantum Sci. Technol., **3**, 1426216 (2024).

[119] M. Morgado, S. Whitlock, "Quantum simulation and computing with Rydberg-interacting qubits," AVS Quantum Sci., **3**, 023501 (2021).

[120] K. Kim, M. Kim, J. Park, A. Byun, J. Ahn, "Quantum Computing Dataset of Maximum Independent Set Problem on King's Lattice of over Hundred Rydberg Atoms," Scientific Data, **11**, 111 (2024).

[121] J. Park, S. Jeong, M. Kim, K. Kim, A. Byun, L. Vignoli, L-P. Henry, L. Henriet, J. Ahn, "Rydberg-atom experiment for the integer factorization problem," Phys. Rev. Res. **6**, 023241 (2024).

[122] A. G. de Oliveira, E. Diamond-Hitchcock, D. M. Walker, M. T. Wells-Pestell, G. Pelegrí, C. J. Picken, G. P. A. Malcolm, A. J. Daley, J. Bass, J. D. Pritchard, "Demonstration of Weighted-Graph Optimization on a Rydberg-Atom Array Using Local Light Shifts," PRX Quantum, **6**, 010301 (2025).

[123] J. Wurtz, S. H. Sack, S.-T. Wang, "Solving Nonnative Combinatorial Optimization Problems Using Hybrid Quantum–Classical Algorithms," IEEE Transactions on Quantum Engineering, **5**, 1 (2024).

[124] S. Jeong, J. Park, and J. Ahn, "Quantum-enhanced simulated annealing using Rydberg atoms," submitted (2025).

[125] J. Wurtz, A. Bylinskii, B. Braverman, J. Amato-Grill, S. H. Cantu, F. Huber, A. Lukin, F. Liu, P. Weinberg, J. Long, S.-T. Wang, N. Gemelke, A. Keesling, "Aquila: QuEra's 256-qubit neutral-atom quantum computer," arXiv:2306.11727, v1, (2023).

[126] H. M. Bauza and D. A. Lidar, "Scaling Advantage in Approximate Optimization with Quantum Annealing," arXiv:2401.07184v1 (2024).

[127] Gurobi Optimization: MIPGap.

[128] B. F. Schiffer, D. S. Wild, N. Maskara, M. Cain, M. D. Lukin, R. Samajdar, "Circumventing superexponential runtimes for hard instancesof quantum adiabatic optimization," Phys. Rev. Res. **6**, 013271 (2024).

[129] N. Metropolis, A. W. Rosenbluth, M. N. Rosenbluth, A. H. Teller, E. Teller, "Equation of State Calculations by Fast Computing Machines," J. Chem. Phys.,**21**, 1087 (1953).

[130] W. K. Hastings, "Monte Carlo sampling methods using Markov chains and their applications," Biometrika **57**, 97 (1970).

[131] Y. Han, Y. Wang, Y. Cao, Z. Geng, Q. Zhu, "A Novel Wrapped Feature Selection Framework for Developing Power System Intrusion Detection Based on Machine Learning Methods," IEEE Transactions on Systems, Man, and Cybernetics: Systems, **53**, 7066 (2023).

[132] Z. Li, Y. Chen, Y. Song, K. Lu, J. Shen, "Effective Covering Array Generation Using an Improved Particle Swarm Optimization," IEEE Transactions on Reliability, **71**, 284 (2022).

[133] Y. Shen, G. Ge, "Multi-Objective Particle Swarm Optimization Based on Fuzzy Optimality," IEEE Access, **7**, 101513 (2019).

[134] A.-E. Iordan, "A Comparative Study of Three Heuristic Functions Used to Solve the 8-Puzzle," Journal of Advances in Mathematics and Computer Science, **16** (1), 1 (2016).

[135] A. Kammerdiner, P. A. Krokhmal, P. M. Pardalos, "On the Hamming distance in combinatorial optimization problems on hypergraph matchings," Opt. Lett. **4**, 609 (2010).

[136] B. Hajek, "Cooling Schedules for Optimal Annealing," Math. Oper. Res., **13**, 311 (1988).

[137] C. Bouttier, I. Gavra, "Convergence Rate of a Simulated Annealing Algorithm with Noisy Observations," J. Mach. Learn. Res., **20**, 1 (2019).

[138] T. Albash, D. A. Lidar, "Demonstration of a Scaling Advantage for a Quantum Annealer over Simulated Annealing," Phys. Rev. X, **8**, 031016 (2018).

[139] S. Jeong, J. Park, J. Ahn. "Codes, Data and Figures for "Quantum-enhanced simulated annealing using Rydberg atoms"", *figshare* https://doi.org/10.6084/m9.figshare.c.7639259.v1, (2025).

Acknowledgments in Korean

이번 박사 학위논문을 작성하면서, 대학원 과정동안 제게 학문적으로 여러 면에서 도움을 주신 많은 분들이 떠올랐습니다. 먼저 여러모로 부족한 점이 많은 제가 학문적으로 성장하고 학위과정을 끝까지 잘 마칠 수 있도록 지도해주신 안재욱 교수님께 감사의 말씀 올립니다. 교수님께 연구 지도를 받으면서 논문 작성과 연구 주제들을 바라보는 관점 그리고 학술 활동과 학계 트렌드에 대한 감각과 고찰 등 많은 것을 배울 수 있었습니다.

또한 바쁘신 와중에 학위논문을 심사해주신 최재윤 교수님, 강명수 교수님, 김동규 교수님, 배준우 교수님께도 깊은 감사의 마음을 전하고 싶습니다. 여러 교수님들께서 주신 다각도의 연구 조언과 통찰력 있는 피드백은 제 연구의 부족한 점을 보완하여 연구자로서 다방면에서 깊이 성장할 수 있는 큰 도움이 되었습니다. 교수님들께서 주신 충고와 가르침은 앞으로의 학술 연구에 필요하고 소중한 밑거름으로 삼을 것입니다.

학위 과정에서 제게 든든한 지지와 응원으로 버팀목과 원동력이 되어준 부모님과 동생 유진이에게도 진심으로 감사드립니다. 이 자리를 빌어 항상 저를 아낌없이 지원해주고 곁에 있어준 가족들에게 깊은 사랑과 존경, 감사를 표하며, 어려운 순간과 고비마다 가족들이 함께 하였기에 끝까지 제 목표를 향해 나아갈 수 있었습니다.

그리고 학위 과정에서 함께 고뇌하고 다양한 시각을 제시하며 같이 공부할 수 있었던 연구실 동료들과 친구, 선후배들께 감사의 말씀 드립니다. 연구실 선배로서 연구자로서 다양한 관점과 연구 방향을 제시해 주신 송윤흥, 김민혁, 변우정, 선하은, 황한섭 선배님들, 동기 강흔, 학문적인 주제와 소재에 대해 깊이있게 대화하고 함께 고민하던 연구실 후배 주영, 선화, 강진, 승택이 형, Maynardo에게 감사드립니다. 또한 연구실 밖에서 같이 힘이 되어 주었던 저의 친구들 그리고 학부 동기들과 선후배들한테도 고맙다는 말을 전하고 싶습니다.

이 논문이 완성되는데까지 도움을 주신 모든 분들께 깊은 감사드리며, 학위과정을 통해 받은 가르침과 지혜로 과학기술 발전에 이바지할 수 있도록 노력하겠습니다.

Curriculum Vitae

Name	:	Seok-Ho Jeong (정석호)
Date of Birth	:	September 30, 1997
ORCID	:	0000-0002-7219-8955

Educations

2020. 3. – 2025. 8.	**Integrated Master - Ph.D Program in Physics**, Korea Advanced Institute of Science and Technology (KAIST), Daejeon, Korea
2016. 2. – 2020. 2.	**B.S. in Physics (Double major in Mathematics)**, Chung-ang University, Seoul, Korea

Teaching

2021. 3. – 2021. 6.	Teaching Assistant, Classical Electromagnetism I (PH231)
2020. 9. – 2020. 12.	Teaching Assistant, General Physics II (PH142)
2020. 3. – 2020. 6.	Teaching Assistant, General Physics I (PH141)

Academic Activities

1. **Seokho Jeong** and Jaewook Ahn, *Quantum-enhanced simulated annealing using Rydberg atoms*, 2024 KPS Fall meeting, 2024.10.23-2024.10.25

2. **Seokho Jeong**, Minhyuk Kim, Minki Hhan, and Jaewook Ahn, *Quantum Computing of 3-SAT problems using Rydberg atom arrays*, APS March Meeting 2023, 2023.03.05-2023.03.10

3. **Seokho Jeong**, Minhyuk Kim, and Jaewook Ahn, *Quantum Computing of 3-SAT problems using Rydberg atom graphs*, The 15th Asia Pacific Physics Conference (APPC15), 2022.08.21-2022.08.26

4. **Seokho Jeong**, Xiao-Feng Shi, Minhyuk Kim, and Jaewook Ahn, *Rydberg wire gates for universal quantum computation*, 2022 KPS Spring meeting, 2022.04.20-2022.04.22

5. **Seokho Jeong**, Andrey Moskalenko, and Jaewook Ahn, *Quantum Gate Design using GRAPE Algorithm in Rydberg Systems*, KPS Atomic and Molecular Physics Division Workshop (AMP2021), 2021.06.21-2021.06.23

Publications

1. **Seokho Jeong**, JuYoung Park, and Jaewook Ahn, "Quantum-enhanced simulated annealing using Rydberg atoms," submitted (2025).

2. Sunhwa Hwang, Hansub Hwang, Kangjin Kim, Andrew Byun, Kangheun Kim, **Seokho Jeong**, Maynardo Pratama Soegianto, and Jaewook Ahn, "Fast and reliable atom transport by optical tweezers," *Optica Quantum* **3**, 64 (2025).

3. Andrew Byun, **Seokho Jeong**, and Jaewook Ahn, "Programming higher-order interactions of Rydberg atoms," *Physical Review A* **110**, 042612 (2024).

4. Andrew Byun, Junwoo Jung, Kangheun Kim, Minhyuk Kim, **Seokho Jeong**, Heejeong Jeong, and Jaewook Ahn, "Rydberg-atom graphs for quadratic unconstrained binary optimization problems," *Advanced Quantum Technologies* 2024, **7**, 2300398 (2024).

5. Juyoung Park, **Seokho Jeong**, Minhyuk Kim, Kangheun Kim, Andrew Byun, Louis Vignoli, Louis-Paul Henry, Loic Henriet, and Jaewook Ahn, "Rydberg-atom experiment for the integer factorization problem," *Physical Review Research* **6**, 023241 (2024).

6. **Seokho Jeong**, Minhyuk Kim, Minki Hhan, JuYoung Park, and Jaewook Ahn, "Quantum programming of Satisfiability problem with Rydberg Atom Graphs," *Physical Review Research* **5**, 043037 (2023).

7. **Seokho Jeong**, Xiao-Feng Shi, Minhyuk Kim, and Jaewook Ahn, "Rydberg wire gates for universal quantum computation," *Frontiers in Physics* **10**, 875673 (2022).